POLITECNICO DI MILANO

Doctoral Program in Hydraulic Engineering

LABORATORY-SCALE CHARACTERIZATIONS OF THE MIXING ZONE FOR REACTIVE TRANSPORT IN A CARBONATE SYSTEM.

Mohamed Fathy KASSAB

A Dissertation
Submitted to the School of Doctoral Programs of the Politecnico di Milano
in Partial Fulfillment of the Requirements for the Degree of
Doctor of Philosophy
in
Hydraulic Engineering

Supervisor:	Prof. Alberto GUADAGNINI	Politecnico di Milano (DIIAR)
Co-advisors:	Prof. Monica RIVA	Politecnico di Milano (DIIAR)
Co-advisors:	Dr. Philippe GOUZE	CNRS- Montpellier- France
Coordinator of Doctoral program:		Prof. Alberto GUADAGNINI

Milan, 2012 (XXIII)

Dedication

This modest work is dedicated to…

The pure souls of the martyrs of Egypt,

My lovely mother, *the source of safety and love,*

My dear father, *thanks for your patience and infinite support,*

My dear brothers Nasser *&* ***Hany*** *&* ***Yasser*** *&* ***Hassan*** *as well as their families,*

My dear sisters, Hanaa *&* ***Tahany*** *as well as their families,*

My lovely wife Sara *the source of my happiness.*

To Mr. Sameer Bazeed *& his family*

To my dear friends, Ali; Ahmed *&* ***Zaher***

Really you are the main source of my success, I love you all

Acknowledgements

I would like to begin by expressing my sincere appreciation to my supervisor *prof. Alberto Guadagnini* as well as *prof. Monica Riva* for their patience, unreserved guidance, and invaluable support.

My deep appreciation is expressed also to my advisor *Dr. Philippe Gouze* and his research team of Geosciences Montpellier dept. especially *Charlotte Garing* and *Linda Louqut* for their infinite support and scientific collaboration; really this work would not have been possible without their support.

Sincere thanks are extended to all those who help me and contributed to complete this work, especially, *Eng. Richard Leprovost* for the technical assistance of experimental setup.

I am also grateful to DIIAR department staff, with special mention to the director *prof. Enrico Larcan,* for facilitating all challenges during my study.

Thanks for all the staff of the administrative office *Mr. Matteo Sdravato* (*DIIAR- Politecnico di Milano) and Ms. Bernadette Marie-Hurson (Geosciences Montpellier).*

The financial support provided by the doctoral school of the Politecnico di Milano University and the University of Montpellier 2 is gratefully acknowledged.

I would like to express sincere thanks to *Prof. Soliman M. Soliman , prof. Yehia Galal and Prof. Mohamed Abd Elmoiem* as well as all the staff of Soil and Water Research Dep., Atomic Energy Authority, Cairo, Egypt, that have nominated me to study the Doctorate program at the Politecnico di Milano in Italy.

I am also grateful to IAMB staff, with special mention to *prof. Nicola Lamaddalena* and *prof. Antonio Coppola* from University of Basilicata for their collaboration in publishing our research in the advanced in water research journal.

To the soul of my advisor in Egypt *prof. Abd El.naby Gadalla,* you are always in our mind and we pray that God bless you.

I would like to express my infinite gratitude to all my friends especially *Liudmila Patrikeeva and Samer Majdalani* for their solidarity and endless capacity to surpass all the difficulties.

Mohamed Kassab
25th, January 2012

Laboratory-scale characterizations of the mixing zone for reactive transport in a carbonate system.

ABSTRACT

We have performed laboratory-scale percolation experiments combining hydrodynamic and geochemical reaction processes in a unique setup to study the evolution of permeability induced by dissolution reactions in a natural Carbonate system. First, the key parameters controlling Calcite dissolution due to mixing of two end member solutions representing fresh and sea waters are assessed through typical geochemical modeling. Both solutions are at equilibrium with Calcite and are associated with different values of partial pressure of CO_2 and salinity. Mixing of the two selected end members provides a subsaturated solution with low and moderate ionic strength, high pCO_2, and high salinity. Modeling results reveal that the maximum subsaturation is expected to occur for mixing ratios of about 15%. The expected dissolved Calcite until equilibrium attains its maximum at a mixing ratio of about 45%. Experimental results indicate that the calcite dissolution rate at a 15% mixing ratio is higher than that observed at 45% mixing ratio. The outlet solution from the sample reactor is always undersaturated with respect to Calcite. Permeability of the tested sample displays a rapid decrease during the beginning of injection. It then shows a stable behavior until the end of percolation when the porosity of the sample increases due to dissolution. To understand permeability and porosity evolution obtained from the mixing experiments we perform dissolution experiments under different dissolution regimes by injection of deionized water (DW) and/or DW enriched with CO_2. It is observed that permeability decreases when DW is injected whereas it increases following injection of DW enriched with CO_2. The observed global dissolution rate of Calcite is larger for the experiments with DW enriched with CO_2 than for those performed with DW. The observed permeability reduction is due to the clogging of connected pore caused by migration of micro particles detaching from the host porous matrix and migrating towards the outlet. Evidences of particles migration and pore clogging are verified through SEM and XRMT analysis. A key conclusion of the study is that a dissolution reaction can lead to permeability reduction if the dissolution rate is not large enough to dissolve detached microparticles. The observed permeability reduction is interpreted through a simple zero-dimensional model relating permeability to grain size distribution and relying the measured global reaction rate to the rate of partitioning of the particles that constitute the porous medium matrix.

Keywords: saltwater intrusion, mixing zone, dissolution, permeability, porosity, Carbonate.

Caratterizzazioni su scala di laboratorio della zona di mescolamento per il trasporto reattivo in un sistema carbonatico naturale.

RIASSUNTO

Si sono effettuati esperimenti di percolazione su scala di laboratorio per l'analisi congiunta di processi idrodinamici e geochimici al fine di analizzare l'evoluzione dinamica della permeabilità a seguito di reazioni di dissoluzione in un sistema carbonatico naturale. In una prima fase si è adottato un modello geochimico per la valutazione dell'effetto dei parametri principali che controllano la dissoluzione del carbonato di calcio a seguito della miscelazione di due soluzioni che rappresentano acqua dolce e salata. Le due soluzioni considerate sono in equilibrio con il $CaCO_3$ e sono associate a differenti valori di pressione parziale di CO_2 e di salinità. La miscelazione delle due soluzioni risulta in una soluzione che si trova in condizioni di sotto-saturazione, con forza ionica bassa / moderata, elevate pCO_2 e salinità. I risultati della modellazione rivelano che la sotto-saturazione massima si verifica per rapporti di miscelazione intorno al 15%. La dissoluzione attesa di $CaCO_3$ raggiunge il suo massimo per rapporto di miscelazione pari a circa il 45%. Risultati sperimentali indicano che il tasso di dissoluzione ad un rapporto di miscelazione del 15% è superiore a quanto osservato per un rapporto di miscelazione pari al 45%. La soluzione in uscita dal reattore contenente il campione utilizzato è sempre sotto-saturata rispetto al $CaCO_3$. La permeabilità del campione testato mostra una rapida diminuzione durante la prima fase dell'iniezione. Successivamente, si rileva un comportamento stabile chepermane fino all'esaurimento della percolazione, quando si osserva un incremento della porosità del campione a causa di processi di dissoluzione. Per comprendere la dinamica di permeabilità e porosità osservata negli esperimenti di miscelazione, si sono effettuati esperimenti di percolazione per diversi regimi di dissoluzione, iniettando acqua deionizzata (DW) e/o DW arricchita con CO_2. Si osserva che la permeabilità del campione di roccia testato diminuisce a seguito dell'iniezione di DW, mentre aumenta a valle dell'iniezione di DW arricchita con CO_2. Il tasso globale di dissoluzione di calcite osservato è maggiore per gli esperimenti con DW arricchita con CO_2 rispetto a qaunto misurato negli esperimenti effettuati con DW. Si ritiene che la riduzione della permeabilità sia dovuta ad un intasamento di pori interconnessi causato dalla migrazione di micro particelle che si staccano dal matrice porosa e migrano nel sistema. Risultati di analisi SEM e XRMT supportano questo schema concettuale. La conclusione principale dello studio consiste nella osservazione sperimentale che una reazione di dissoluzione può risultare in una riduzione della permeabilità se il tasso di dissoluzione non è sufficiente elevato da dissovlere le microparticelle solide che si distaccano dalla matrice del mezzo poroso. La riduzione di permeabilità osservata è quindi interpretata attraverso un modello semplice (zero-dimensionale) basato sul modello concettuale descritto.

Parole chiave: intrusione di acqua salata, zona di mescolamento, dissoluzione, permeabilità, porosità, sistemi carbonatici.

Caractérisations à l'échelle de laboratoire de la zone de mélange pour transport réactifs dans un système de carbonate.

RÉSUMÉ

Des expériences d'infiltration à l'échelle de laboratoire ont été faites où les conditions hydrodynamiques et géochimiques ont été combinées pour étudier l'évolution de la perméabilité due aux réactions de dissolution dans un système carbonaté naturel. Au début, le model géochimique PHREEQC a été utilisé pour étudier les paramètres qui contrôlent la dissolution de la Calcite avec deux solutions représentant un mélange d'eau fraîche et d'eau salée, toutes les deux en équilibre avec la Calcite et avec différents niveaux de pression partielle du CO_2 et de salinité. Les solutions résultantes ont montré une sous-saturation pour une faible force ionique, une forte pCO_2 et une forte salinité. Les résultats ont montré que le maximum de sous saturation a lieu pour des proportions de mélange de 15%, alors que la Calcite dissoute atteint son maximum à 45% de proportion de mélange jusqu'à l'équilibre. Les résultats expérimentaux indiquent que le taux de dissolution de la Calcite à 15% est plus important qu'à 45% et la solution sortante de l'échantillon est toujours sous saturée en Calcite. La perméabilité de l'échantillon a diminué rapidement au début de l'injection et puis son comportement était stable jusqu'à la fin de l'infiltration, alors que la porosité de l'échantillon a augmenté à cause de la dissolution. Pour comprendre l'évolution de la porosité et de la perméabilité lors des expériences d'infiltration, nous avons mené des expériences de dissolution sous différents régimes de dissolution en injectant de l'eau désionisée et/ou de l'eau désionisée enrichie avec du CO_2. La perméabilité a diminué (respectivement augmenté) quand l'eau désionisée (respectivement de l'eau désionisée enrichie avec du CO_2) a été utilisée. Le taux de dissolution de la Calcite était plus important avec l'eau désionisée enrichie avec du CO_2. La diminution de la perméabilité était due au colmatage des pores connectés à cause de la migration de microparticules détachées pendant la dissolution. Les preuves de migration ou de réarrangement de particules et du colmatage de pores ont été vérifiées à l'aide des analyses SEM et XRMT. On peut ainsi déduire que la réaction de dissolution peut conduire à une diminution de la perméabilité si le taux de dissolution n'est pas suffisamment important pour dissoudre les microparticules détachées et vice versa. La diminution de la perméabilité a été simulée à l'aide d'un modèle à zéro dimension où la perméabilité a été reliée à la taille des grains, tout en prenant comme paramètres de calage le taux de dissolution expérimental et le taux de désagrégation des particules par dissolution.

Mots-clés: intrusion d'eau salée, zone de mélange, dissolution, perméabilité, porosité, carbonate.

Table of Contents

List of Figures

List of Tables

Chapter 1

Introduction

1. Introduction

1.1. Background and problematic

Approximately 78% of the total freshwater on Earth is located and stored in the subsurface. Nevertheless, despite the abundance of groundwater resources, uncontrolled and unregulated extraction of the resource can contribute to changes in the aquifer systems. In coastal areas for instance, overexploitation has disturbed the naturally established equilibrium between seawater and freshwater resulting in uncontrolled saltwater encroachment into coastal aquifers. As a large portion of the world's population (e.g. about 70%) dwells in coastal zones, it is therefore important to develop optimal exploitation of groundwater and to control saltwater intrusion (Bear et al., 1999).

Saltwater intrusion is a major concern commonly found in coastal aquifers around the world. It is the induced flow of seawater into freshwater aquifers primarily caused by groundwater development near the coast. Where groundwater is being pumped from aquifers that are in hydraulic connection with the sea, induced gradients may cause the migration of salt water from the sea toward a well, making the freshwater well unusable. Because fresh water is less dense than salt water it floats on top. The boundary between salt water and fresh water is not distinct, and the zone of dispersion is brackish with salt water and fresh water mixing.

Reactive transport models have demonstrated that important porosity development may occur at the salt water-fresh water mixing zone of coastal aquifers on a geological time scale (Sanford and Konikow, 1989 a,b; Rezaei et al., 2005, Romanov and Dreybrodt, 2006). Mixing of two fluids with different salinity has also been used as a hypothesis to explain deep dissolution of carbonates and the formation of hydrothermal mineral deposits (Corbella et al., 2004). Sediment diagenesis, the formation of mineral deposits, and the evolution of permeability in hydrothermal systems are processes of considerable geologic interest. The rates at which these processes occur are linked to complex, non-linear, mineral-fluid interactions, often leading to dissolution of rock fabric or precipitation of mineral species.

Recent years have seen the growing development and application of reactive transport models to describe, at different spatial and temporal scales, natural and industrial processes involving water-rock interactions in particular porosity, permeability, formation reduction and oil

migration in sedimentary basins, transport and geological sequestration of CO_2, and geothermal power generation. The successful application of these models requires a comprehensive and robust kinetic data base of mineral-water interactions. Significant efforts have been made over the past two decades to i) measure in the laboratory mineral dissolution/crystallization rates and ii) develop robust rate laws which could be incorporated in reactive transport algorithms (Pokrovsky et al. 2005 ; Pokrovsky et al. 2009 ; Schott et al., 2009).

Consequently, there is a great need to improve our understanding of the geochemical processes that take place into coastal carbonate aquifers. This particularly includes the understanding of geochemical reactive transport processes in the mixing zone between salt and fresh water due to rock-water interaction and the factors that control these processes.

The dissolution of Carbonate mineral occurs when flow of undersaturated solution took place through it. These chemical reactions affect the physical and hydraulic properties of the rock such as porosity and permeability. Studying these effects is difficult to realize in the field scale due to the measurement challenges.

Dissolution and precipitation are two of the most important processes affecting groundwater chemistry, and they can significantly modify the physical and chemical properties of porous media. For a given process, it may be possible to construct the associated evolution of permeability- porosity relationship and thus predict the transport properties of rock at depth which may help to characterize its underlying process.

Few percolation experiments were realized at the laboratory scale (Singurindy and Berkowitz (2003); Singurindy et al. (2004); Sanz et al. (2011). These experiments introduced adequate information about the reaction rate of chemical processes i.e. dissolution and precipitation reactions induced by mixing waters. The evolution of hydraulic conductivity in carbonate rock, due to competition among flow, precipitation and dissolution processes, can display a wide variety of possible behaviors, however the tested samples were disturbed (crushed and sieved) or packed samples. Consequently, it is essential to study these processes in natural representative elementary volume (REV) which is closer to reality to understand the effect of chemical reaction on the hydraulic and physical properties more over illustrating the structure and chemical evolution of the tested sample using advanced imaging techniques such as Scan Electron Microscopy (SEM) and X-Ray Micro tomography (XRMT).

1.2. Objectives and dissertation outlines

In this work we present a short and long term laboratory-scale percolation experiments where hydrodynamic and geochemical reactions were combined in one setup to:

1. Investigate the relation between Calcite saturation state and potential dissolution under different mixing ratios and different levels of partial pressure of CO_2 of two end-member solutions equilibrated with Calcite.
2. Characterize the evolution of permeability and porosity under different dissolution regimes using Scan Electron Microscopy (SEM) and X-Ray Micro tomography (XRMT).

The dissertation is structured according to the objectives outlined above. In particular in Chapter 2, we present a brief explanation of the reactive transport processes followed review of literature of the previous experimental and modeling studies. Chapter 3 covers a pure geochemical modeling of different factors and conditions that control the dissolution of Calcite using PHREEQC (version2).

In Chapter 4 we present a description of tested samples, the experimental protocol where hydrodynamic and chemistry are coupled into an experimental setup, the material and methods used in the experimental investigations and the imaging techniques of X-ray and SEM used to characterize the sample structure before and after the percolation experiments.

In Chapter 4 we present the obtained results and discussions in Chapter 6 a simple approach to model permeability reduction is present. Finally in Chapter 7 represents a conclusion of the current study.

Chapter 2

Literature Review

2. Flow and Transport in porous media

2.1. Background

In this chapter we review the flow and transport processes in porous media and the governing equations of these processes. By definition the porous media is a material consists of solid matrix and voids called pores. The percentage of the voids inside the rock called the total porosity. These voids cab be occupied by water, air or other fluids. In our study we carried out our experimental and modeling work with the saturated porous media, which mean that all the voids are saturated with a single phase fluid. The porosity notion is very important when one deals with the flow and transport in porous media because the interconnections of these pores control the circulation of the fluid, hence the permeability of the porous media.
Hereafter, we review some elementary definitions necessary to understand the flow and transport in porous media. In particular the Darcy law and the principle mechanisms of the solute transport in porous media will be reviewed.

2.2. Characteristic parameters of the porous media

A porous media is most often a consolidated or unconsolidated media having an interior fraction of volume accessible to a fluid (Guyon et al., 2001). It is characterized by its porosity, though the void space within the rocks is a complicated connected structure, it is often convenient to think of it as consisting of discrete pores. A pore is defined as a portion of void space bounded by solid surfaces; it connects to another pore or a channel by a narrow opening, referred to as the throat. Interior the pores, three cases of the fluid cab be presented, the first one is the particle movement and deposition, which is important when dealing with percolation and filtration processes that may change the hydrodynamic properties of the porous media. The second case when more than one fluid non miscible existed in the media such as water and air or water and oil, in this case one must take into consideration the capillarity effect to characterize the flow of each phase. The third case is where the porous media are completely saturated of one or more than one miscible fluids.

2.2.1. Porosity (ϕ)

In general, it is a parameter representing the volume fraction occupied by voids or pore spaces in the bulk of the matter concerned. It can be classified in the following ways:

i. Absolute porosity: It is the fraction of the bulk volume occupied by all void spaces irrespective of interconnectivity.
ii. Effective porosity: It is the fraction of the bulk volume occupied only by the interconnected pores spanning the sample.

However porosity may be studied at different stages of rock formation. Primary porosity is an inherent characteristic and is determined at the time the rock is formed. Secondary porosity results from later changes that may alter the primary porosity (Auriault and Boutin, 1992; Lucia, 1999; Berryman and Wang, 2000; Kazatchenko et al., 2006).

2.2.2. Specific surface (A)

The surface area of the pore-solid interface per unit volume of the porous bulk material. It is important when dealing with rate of kinetic reactions (dissolution, precipitation, and sorption) and the relation of the porous media geometry and the flow through it.

2.2.3. Tortuosity (τ)

It describes the sinuosity and interconnectedness of the pore space. Tortuosity can be of the following types - geometrical, electrical, diffusional and hydraulic. Each of these is in general distinct and there is no single definition that encompasses all the types (Ben Clennell 1997; Phillips 1991).

Adler (1992) defined the geometrical tortuosity as the ratio between the longest flow pass way (L_{eg}) to the length of the straight line of the rock sample (L) as illustrated in (figure 2.1. a and b). Carman (1937) defined the geometric tortuosity as the ratio between the effective flow pass way of a certain fluid (L_{eh}) to the length of the straight line of the rock sample (L).

Figure (2.1.a, b, c and d) below explains geometrical and hydraulic tortuosity respectively. A greater path length has to be traversed in (b) in comparison to (a) to reach side 2 from 1. The effective path length $L_{eg} = L$ in (a) whereas $L_{eg} > L$ in (b), whereas, at (d) the hydraulic length is much greater than the geometric one in (c).

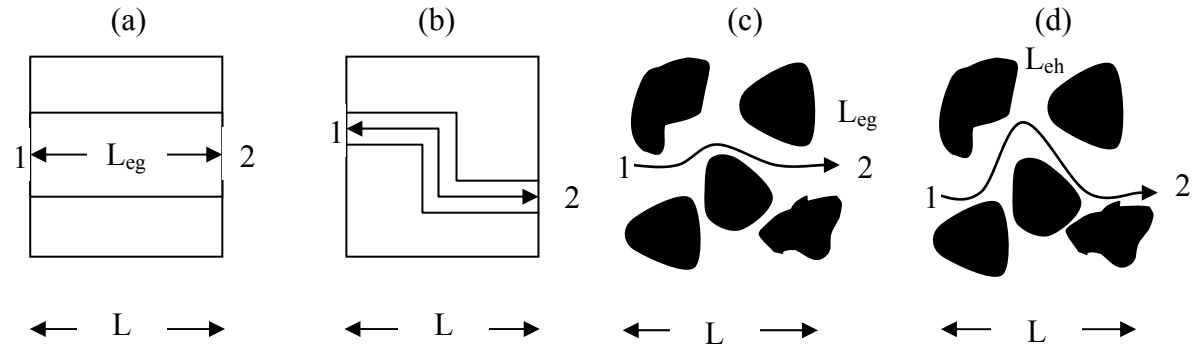

Figure 2.1: Illustration of geometrical and hydraulic tortuosity.

2.2.4. Permeability (*k*):

The permeability is one of the most important parameters in many domains of research such as soil mechanics, hydrogeology, geochemistry and petroleum engineering. In some reference it is called relative permeability or intrinsic permeability and in some other it is called hydraulic conductivity or the coefficient of permeability. Consequently, each definition is corresponding to different measurements units. The permeability usually refers to the ability of a porous media to allow fluids to pass through it. In particular the relative permeability in multi phase flow refers to dimensionless measure of the effective permeability of that phase and it is the ratio of the effective permeability of that phase to the absolute or intrinsic permeability. The intrinsic or the absolute permeability states ability of the porous media to allow fluid passing through the connected pores and it is function of the structure regardless of the fluid. The permeability can be calculated using Darcy's Law, where the ratio of volumetric flow rate Q ($m^3 \cdot s^{-1}$) over the pressure difference ΔP is directly related to the permeability of the sample k (m^2) by:

$$k = -\frac{\mu L}{S}\frac{Q}{\Delta P} \tag{2.1}$$

where, L is the length of the sample in the flow direction (m), S is the section of the sample (m^2) and μ is the dynamic viscosity of the fluid (Pa·s). Permeability values are reported in mD, (1mD ≈ 0.987 10^{-15} m^2). (De Marsily 1986).

2.3. Sea water intrusion in coastal aquifer

In coastal aquifers, groundwater has two origins, inland meteoric recharge and seawater. Hence, subsurface flow dynamics are driven by unstable density variations and by hydraulic head gradients, which are subject to time-varying forcing at both the terrestrial (e.g. seasonally varying recharge) and marine (e.g. tides and waves) boundaries of these aquifers. These processes drive a circulation of seawater in the subsurface of potentially great ecological significance: it increases subsurface mixing between fresh groundwater and seawater and provides a mechanism to continuously flush submarine sediments, enhancing chemical exchange between the aquifer and the overlying water column; Additionally, it may play a role in the breakdown of marine-derived organic matter, and hence contribute fundamentally to the nutrient cycle of coastal ecosystems. However, seawater circulation in coastal aquifers is still poorly understood: its characteristic spatial and temporal scales and the relative importance of various processes are unclear (Barlow 2003).

The capacity of a geologic material to transit water is characterized by the material's hydraulic conductivity, which is commonly referred to as the permeability of the material. Confining units (or confining layers) are geologic units that are less permeable than aquifers. Because of their lower permeability, confining units restrict the movement of ground water into or out of adjoining aquifers. Aquifers and confining units are mapped on the basis of the degree of contrast in hydraulic conductivity among geologic units (Sun and Johnston, 1994). Generally, there is a close correlation between the type of geologic formation and its water-yielding properties. For example, unconsolidated sands and gravels, sandstones, and limestones commonly are major sources of ground-water supplies (aquifers), whereas beds of silt and clay function primarily as confining units (Heath, 1984).

Fresh ground water comes in contact with saline ground water at the seaward margins of coastal aquifers. The seaward limit of freshwater in a particular aquifer is controlled by the amount of freshwater flowing through the aquifer, the thickness and hydraulic properties of the aquifer and adjacent confining units, and the relative densities of saltwater and freshwater, among other variables. Because of its lower density, freshwater tends to remain above the saline (saltwater) zones of the aquifer.

The sharp interface boundary between saltwater and freshwater does not occur under ordinary field conditions. Instead, a brackish transition zone of finite thickness separates the two fluids (Todd and Mays, 2005). The different factors that contribute to the increase in thickness of the transition zone are freshwater dispersion by flow, tides effect, groundwater recharge and wells pumping.

Groundwater abstraction from a coastal aquifer induces groundwater head decreases in both freshwater and saltwater bodies, which result not only in drawdown head depressions and submarine groundwater discharge reductions into coastal zones, but also in increased saltwater inflow and modified isocone contour surfaces which progressively increase the mixing zone thickness (Custodio, 2002).

The salinity distribution established over time depends on coastal aquifer characteristics and location of groundwater extraction.

The freshwater and saltwater zones within coastal aquifers are separated by a transition zone (sometimes referred to as the zone of dispersion) within which there is mixing between freshwater and saltwater (Figure 2.2). The transition zone is characterized most commonly by measurements of either the total dissolved-solids concentration or of the chloride concentration of ground water sampled at observation wells. Although there are no standard practices for defining the transition zone, concentrations of total dissolved solids ranging from about 1000 to 35000 ($mg.l^{-1}$) and of chloride ranging from about 250 to 19000 ($mg.l^{-1}$) are common indicators of the zone.

Within the transition zone, freshwater flowing to the sea mixes with saltwater by the processes of dispersion and molecular diffusion. Mixing by dispersion is caused by spatial variations (heterogeneities) in the geologic structure and the hydraulic properties of an aquifer and by dynamic forces that operate over a range of time scales, including daily fluctuations in tide stages, seasonal and annual variations in ground-water recharge rates, and long-term changes in sea-level position.

These dynamic forces cause the freshwater and saltwater zones to move seaward at times and landward at times. Because of the mixing of freshwater and saltwater within the transition zone, a circulation of saltwater is established in which some of the saltwater is entrained within the overlying freshwater and returned to the sea, which in turn causes additional saltwater to move landward toward the transition zone.

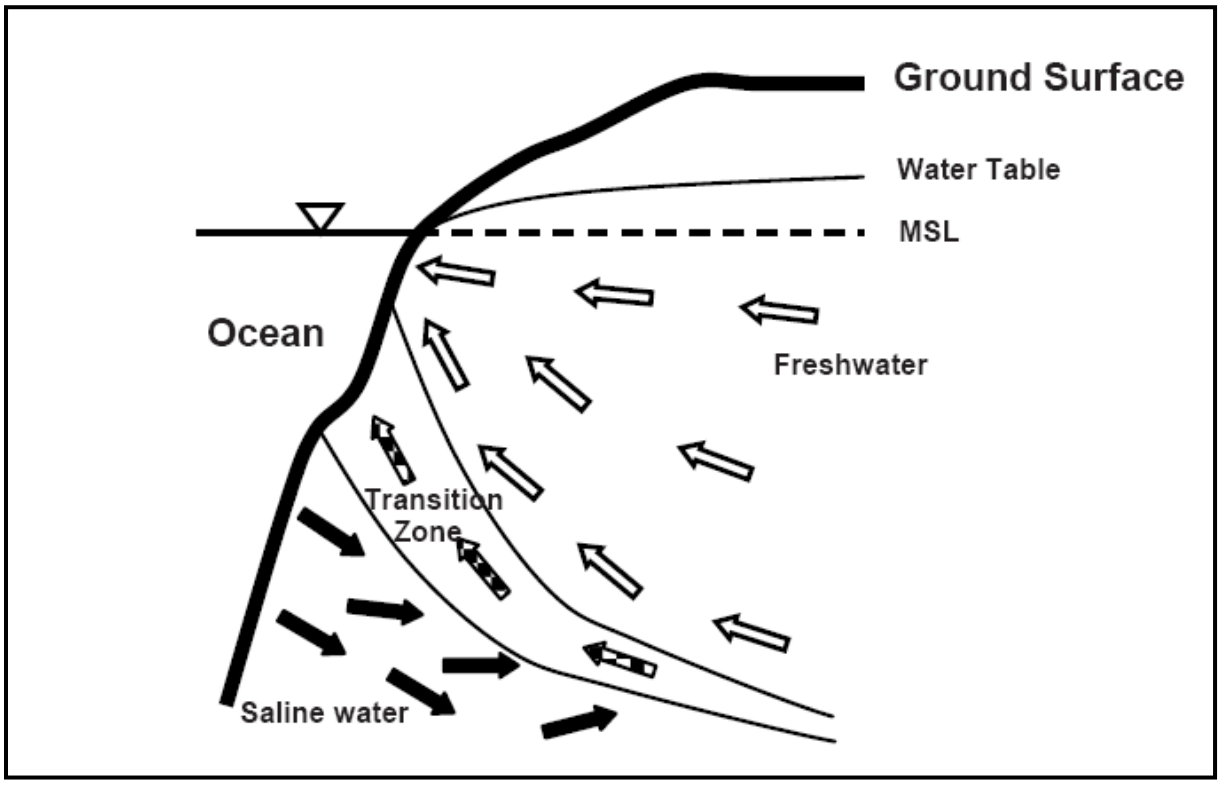

Figure 2.2: Ground-water flow patterns and the freshwater-saltwater transition zone in an idealized coastal aquifer. A circulation of saltwater from the sea to the transition zone and then back to the sea is induced by mixing of freshwater and saltwater in the transition zone (after Custodio, 2002).

The depth to saltwater and the thickness of freshwater in a water-table (unconfined) aquifer can be estimated by applying Ghyben-Herzberg relation which is a relatively simple equation that has been used successfully in many coastal areas. The equation relates the elevation of the water table to the elevation of the boundary of the interface between the freshwater and underlying saltwater zones of an aquifer (Figure 2.3), and is based on the balance of the height of two columns of fluids of differing density (Reilly and Goodman, 1985).

Hence, under hydrostatic conditions, the weight of a unit column of freshwater extending from the water table to the salt-water interface is balanced by a unit column of salt water extending from sea level to that same point on the interface. Also, for every unit of groundwater above sea level there are 40 units of fresh water below sea level.

In the equation of Ghyben-Herzberg, the thickness of the freshwater zone above sea level is represented as (h) and that below sea level is represented as (z), as shown in Figure (2.3). The two thicknesses are related by:

$$z = \frac{\rho_f}{\rho_s - \rho_f} . h \tag{2.2}$$

where: ρ_f the density of freshwater and ρ_f the density of saltwater

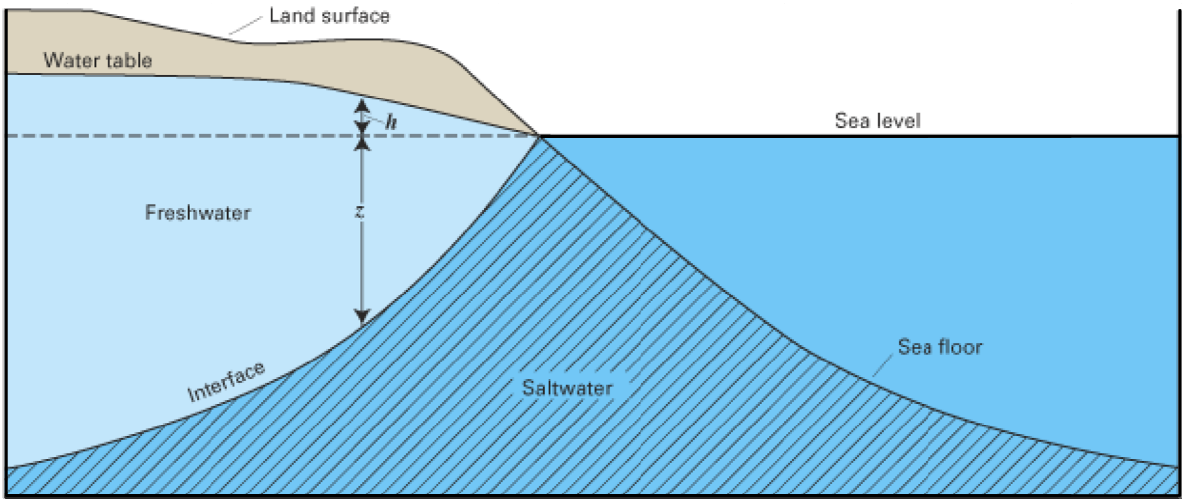

Figure 2.3: Simplified freshwater-saltwater interface in a coastal water-table aquifer (after Barlow 2003).

Incidents of saltwater intrusion have been detected as early as 1845 on Long Island, New York. Intrusion occurs in coastal aquifers worldwide, and is a growing issue in areas including North Africa, the Middle East, the Mediterranean, China, Mexico, and most notably, the Atlantic and Gulf Coasts of the United States, and Southern California. Under normal conditions fresh water flows from inland aquifers and recharge areas to coastal discharge areas to the sea. This natural movement of fresh water towards the sea prevents salt water from entering freshwater coastal aquifers (Barlow, 2003).

Seawater intrusion and contaminant transport in coastal aquifers are two major problems related to environmental and water resources protection in coastal areas and nowadays they are receiving much attention in many countries. Coastal aquifers constitute important sources for water. Since groundwater systems in coastal areas are in contact with saline water, one of the major problems is saltwater intrusion. Saltwater intrusion refers the replacement of fresh

water in coastal aquifers by saltwater due to the motion of a saltwater body into the freshwater aquifer. Saltwater intrusion reduces the available fresh groundwater resources in coastal aquifers. For instance, overexploitation has disturbed the naturally established equilibrium between seawater and freshwater resulting in uncontrolled saltwater encroachment into coastal aquifers which causes seawater intrusion phenomenon.

Coastal aquifers are generally composed of carbonate materials. The theory of carbonate subsaturation by mixing has been extensively used to interpret carbonate dissolution textures found in caves and borehole samples from coastal environments (Plummer 1975). Carbonate minerals constitute ~20% of Phanerozoic sedimentary rock, and at least 60% of the world's known petroleum reserves occur in carbonate reservoirs (Gledhill and Morse, 2006); moreover, Calcite is the major carbonate mineral in sedimentary rocks. The understanding of Calcite dissolution is not important for modeling of geochemical cycle but also has a practical application for the field of petroleum engineering, natural gas reservoirs and water resources management (Morse and Arvidson 2002).

2.4. Transport processes in porous media

The underlying mechanisms controlling the evolution of the fluid-solid system are many. The two phases are generally composed of numerous chemical components ranging from abundant species to trace compounds. This induces various exchange mechanisms (ion exchange, adsorption, surface precipitation/dissolution, nucleation) controlled by complex microscopic physico-chemical phenomena (electrostatic interactions, hydrophobicity). But, the evolution depends also on the coupling transport-chemical reactions. If the geometrical properties of the medium are not modified by the chemical exchanges (Cvetkovic and Dagan, 1994; Walsh et al, 1984), hydrodynamics controls the spatial distribution of the chemical processes especially since the chemical composition of the medium is spatially heterogeneous. On the contrary, if the precipitation/dissolution process characterizes the interaction between the two phases (Steefel et al., 1994; Hoefner et al., 1988), hence, the geometrical characteristics of the permeable medium may alternate. In such a case, we have a coupling with a feedback effect. Hydrodynamics acts on the evolution of the spatial distribution of the chemical species, and the chemical flux between the two phases acts also

on the hydrodynamic properties through the modification of heterogeneities of the porous medium. This kind of interaction is particularly nonlinear. All the parameters describing the state of the system depend on time, except obviously for the boundary and initial conditions, and the feedback induces their mutual coupling.

Owing to the complexity of the feedback process, the theoretical studies are mainly numerical. Some analytical approaches have been carried out in the case of extremely simplified systems (Magnico, 1996; Ortoleva et al., 1987a, b; Schechter et al., 1969; Guin, 1971). Even if they are far from reality at the field scale, they allow an important insight into the fundamental mechanism of chemical reaction-transport coupling.

Transport is a fundamental part of the fluid-rock interaction process for two reasons: 1) it provides the driving force for many of the reactions that take place by continuously introducing fluid out of equilibrium with respect to the reactive solid phase, and 2) it provides a characteristic time scale to be compared with the rates of reaction. In a batch system, the time scale of interest is the time over which equilibrium is achieved (where net reaction rates are, by definition, equal to zero), or rates become so slow that the system effectively no longer changes. In an open system, a good laboratory analogue of which is the continuously stirred tank reactor (CSTR) or well-mixed flow through reactor, the continuous injection of solution that is out of equilibrium (either with itself, or with a solid phase inside the reactor) causes the solution composition coming out of the reactor to reach a steady-state. If the residence time in the CSTR is long enough, equilibrium between the solution and solid phase may be achieved. Otherwise, the solution and solid phase may remain some distance from equilibrium at steady state (Steefel and Maher, 2009).

In porous and/or fractured media, reactions can be driven by a variety of transport processes and changes in porosity, mineral saturation states and mineral abundances can be distributed along a flow path. The most important of these transport processes are advection, molecular diffusion, and mechanical dispersion. Although widely neglected, electrochemical migration is a flux created by the diffusion of charged species at differing rates which may be important in some cases. Below, these transport processes are defined mathematically in terms of fluxes, that is, the amount of solute passing through a unit area per unit time.

2.4.1. Advection

Advection involves the transport in space of dissolved or suspended material at the rate of movement of the bulk fluid phase. No modification of the shape of a front and no dilution occur when transport is purely via advection, a sharp front remains so when undergoing purely advective transport. The advective flux, J_{adv} of a dissolved species in porous media can be described mathematically as:

$$J_{adv} = \phi \, v \, C_i \tag{2.3}$$

where ϕ is the porosity, v is the average linear velocity in the media, and C_i is the concentration of the i^{th} species. In most (but not all) examples of water-rock interaction, flow is through a porous medium and is described with Darcy's Law.

Darcy's Law is applied where the porous medium can be treated as a continuum in which a representative elementary volume (REV) is significantly larger than the average grain size. In the case of flow at the pore scale, the averaging does not apply and Darcy's Law cannot be used.

2.4.2. Molecular diffusion

In water-rock interaction, we are often concerned with transport through low porosity and permeability material, in which case molecular diffusion needs to be included in addition to flow. The treatment of molecular diffusion has also suffered to some extent from the assumption that Fick's First Law (described below) is sufficient, but as shown below, this is true only in the case of diffusion of uncharged species in dilute solutions. A more general formulation relates the diffusive flux linearly to gradients in the chemical potential rather than concentration, but we begin with the simpler Fickian description of diffusion for the sake of simplicity.

Molecular diffusion is usually described in terms of Fick's First Law, which states that the diffusive flux J_i (here shown for only a single coordinate direction x) is proportional to the concentration gradient:

$$J_i = -D_i \frac{\partial C_i}{\partial x} \tag{2.4}$$

Where D_i is referred to as the diffusion coefficient and it is specific to the chemical component considered as indicated by the subscript *i*.

Fick's First Law is a phenomenological theory for diffusion that relates diffusion to the the concentration gradient.

Integrating the diffusive fluxes over a control volume leads to Fick's Second Law (Bear 1972; Lasaga 1998). By defining the fluxes at the faces of an elemental volume in a single coordinate direction *x*, the Fick's Second Law can be written as:

$$\frac{\partial C_i}{\partial t} = -\frac{\partial}{\partial x}\left[D_i \frac{\partial C_i}{\partial x}\right] \tag{2.5}$$

which provides an expression for the change in concentration in terms of the divergence of the diffusive flux.

2.4.3. Hydrodynamic dispersion

The spreading of the solute mass as a result of dispersion is a diffusion-like process that has led to the use of Fick's First Law to describe the process in one dimension as:

$$J_j^{dis} = -D_h \frac{\partial C_i}{\partial x} \tag{2.6}$$

where D_h is the hydrodynamic dispersion coefficient. The coefficient of hydrodynamic dispersion is defined as the sum of molecular diffusion and mechanical dispersion $D_h = D_i + D_m$ since these effects are not separable where flow is involved (Bear 1972).

Mechanical dispersion is a result of the fact that variations in the flow velocities exist, even where an average flow rate (as in Darcy's Law) can be defined for a particular representative elementary volume (REV). If all the detailed flow paths could be captured, then there would be no need for inclusion of a dispersion coefficient.

In porous media the velocity adjacent to a solid grain is slower than the velocities in the center of the pore. Even in the case of a perfectly homogeneous porous medium (e.g., glass beads all of the same size), therefore, spreading of a solute plume will occur. Additional

effects in porous media are related to the tortuosity of flow paths (Figure 2.1) and to differences in pore size, since velocities will be higher in those pores with wider apertures (Bear 1972). Dispersion needs to be quantified at much larger scales in porous media, however, so some averaging of these dispersion mechanisms is usually required. Dispersion in porous media is typically defined as the product of the fluid velocity and dispersivity, α, with longitudinal and transverse components as follows:

$$D_L = -\alpha_L \, v_i \tag{2.7}$$

$$D_T = -\alpha_T \, v_i \tag{2.8}$$

where v_i refers to the average velocity in the principal direction of flow, and the subscripts L (longitudinal) and T (transverse) refer to the dispersion coefficient parallel and perpendicular to the principal direction of flow respectively.

2.4.4. Reaction-induced changes in transport properties

Physical properties of the porous medium evolve as a result of chemical reactions which affect the transport properties. The most commonly identified coupling involves the porosity and permeability as affected by dissolution or precipitation, but other properties like the reactive surface area may evolve as well. A number of experimental studies have been conducted in which reaction-induced permeability change was identified (Dobson et al., 2003). Modeling and experimental studies have also been carried out in which flow and reaction have been explicitly coupled and allowed to evolve (Ortoleva et al., 1987a,b; Steefel and Lasaga 1990, 1994; Steefel and Lichtner 1994; Steefel and Lichtner 1998 a,b; Dobson et al., 2003; Cochepin et al. 2008; Steefel and Maher, 2009). Recently Katz et al. (2011) performed experimental and modeling investigation of multicomponent reactive transport in porous media.

Porosity is typically the first order parameter that is predicted from reactive transport simulations, since it is directly related to the sum of the mineral volumes precipitated or dissolved. It is possible to predict the evolution of the total porosity, therefore, with some degree of confidence. More difficult is to predict the transport parameters, especially permeability and diffusivity, since they depend on the detail pore geometry.

Navarre-Sitchler et al. (2009) studied the evolution of the porosity, pore connectivity, pore geometry, and diffusivity as a function of the extent of chemical weathering in addition they characterized the porosity and pore connectivity as a function of weathering were imaged with X-ray microtomography. This study showed that as the chemical weathering process advanced within the approximately 1 mm wide weathering interface developed within a basalt clast, porosity increased as the primary minerals dissolved (as one would expect), but that pore connectivity increased as well once a critical porosity of ~9% was achieved.

In order to study the reactive transport in porous media, the transport processes outlined above must be combined with expressions for kinetically-controlled geochemical and biogeochemical reaction.

For a constant porosity, tortuosity, and flow system characterized by a first-order precipitation and dissolution reaction that can be described in terms of a single chemical component as follows:

$$\phi\frac{\partial C}{\partial t} = -\phi v\,\frac{\partial C}{\partial x} + \phi D^{*}\frac{\partial^{2} C}{\partial x^{2}} + Ak(1-\frac{C}{C_{eq}}) \qquad (2.9)$$

where k is the rate constant in units of (mol.m^{-2} s^{-1}), A is the reactive surface area of the mineral in units of (m^{2}.m^{-3}) and C_{eq} is the solubility of the mineral in (mol.m^{-3}). The first and second term in the right hand side of equation (2.9) stands for advection and diffusion respectively, where the third term stands source/sink term of the solute due to the chemical reactions. The effective diffusion coefficient D^{*} in porous media is obtained by multiplying the tortuosity by the diffusion coefficient for the solute in pure water.

By converting a partial differential equation to its non-dimensional form, it is possible to define a series of parameters that describe the relative importance of dynamic processes like chemical reaction, advection, and hydrodynamic dispersion.

Considering a length scale, l, this may be a characteristic length scale of the flow length through an aquifer or more commonly a length scale which reflects the spatial distribution of observations. Using this length scale, a nondimensional or fractional distance can be defined:

$$x' = \frac{x}{l} \qquad (2.10)$$

In addition, this allows us to define a characteristic time for dispersive transport

$$t_D = \frac{l^2}{D^*} \tag{2.11}$$

and a characteristic time for advective transport

$$t_A = \frac{l}{v} \tag{2.12}$$

and the characteristic time for reaction can be obtained from

$$t_R = \frac{\phi C_{eq}}{Ak} \tag{2.13}$$

It is possible to define a series of non-dimensional parameters that control the behavior of a water-rock interaction system involving transport: the Damköhler number for advective, Da_I, and diffusive (or dispersive), Da_{II}, systems respectively

$$Da_I = \frac{t_A}{t_R} = \frac{Akl}{\phi v C_{eq}} \tag{2.14}$$

$$Da_{II} = \frac{t_D}{t_R} = \frac{Akl^2}{\phi D^* C_{eq}} \tag{2.15}$$

In addition, the relative importance of advective versus diffusive (or dispersive) transport is compared in the Péclet number

$$Pe = \frac{t_D}{t_A} = \frac{vl}{D^*} \tag{2.16}$$

Each of these numbers depends on the characteristic length scale considered (Steefel and Maher, 2009). By writing a non-dimensional form of the concentration and time

$$C' = \frac{C - C_{eq}}{C_0 - C_{eq}} \tag{2.17}$$

$$t'_D = \frac{D^* t}{l^2} \tag{2.18}$$

where C_0 is the concentration of the fluid injected into the system, consequently equation (2.9) becomes:

$$\frac{\partial C'}{\partial t'_D} = \frac{\partial^2 C'}{\partial x'^2} - Pe\frac{\partial C'}{\partial x'} - Da_{II}C' \tag{2.19}$$

which makes clear how the Péclet and Damköhler numbers control the behavior of the advection-dispersion-reaction equation.. At high Péclet numbers (Pe >>1), advective transport dominates and dispersive and diffusive transport are negligible, where Low Peclet numbers imply that the solute transport is dominated by the dispersion process. High Damköhler number >> 1, reaction times are much faster than transport times for a given length scale. Da < 1, dissolution is surface-reaction-limited and dissolution is assumed spatially homogeneous.

2.5. Carbonate dissolution kinetics

The reaction between a solid and solution is observable by a change in the mass of solid and a change in solution composition. Because these represent ‘‘net’’ changes, it is not usually possible to obtain ‘‘absolute’’ rates of dissolution and precipitation, but only to observe the difference between the opposing reactions. The concept of kinetic equilibrium rests on the idea that at equilibrium the rates of the opposing reactions are equal so that no change is observable with time even though dissolution and precipitation are continually occurring. Dissolution rates of highly soluble and highly insoluble minerals tend to be relatively fast and slow, respectively. Dissolution of highly soluble minerals therefore has a greater likelihood of becoming transport-limited as compared to low solubility minerals which are likely to be interface-limited. Experimentalists often test for transport control of dissolution of minerals by varying the agitation or recycle rate of the reactor (Rosso and Rimstidt, 2000). One mineral that has been investigated in the laboratory under both transport and interface limitation is calcite.

The relative importance of interface versus transport control during calcite dissolution varies with pH (Plummer et al., 1978). Here we review the classic model of Plummer et al. but the reader is also referred to more recent surface complexation models for carbonate dissolution (Pokrovsky and Schott, 2000; Pokrovsky et al., 2005; Pokrovsky et al., 2009).

The most commonly used equation in geosciences to describe the rate of carbonate mineral dissolution (e.g., Morse, 1983) is

$$R = -\frac{dm_{Calcite}}{dt} = \left(k\frac{A}{V}\right)(1-\Omega)^n \tag{2.20}$$

where R stands for a rate constant (mol.cm^{-2}.s^{-1}), m refers to moles of Calcite, t is time, A is the total surface area of the solid, V is the volume of solution, k is the rate constant, n refers to a reaction order, and Ω is saturation sate defined as the ratio between ion activity product and equilibrium constant as follows:

$$\Omega = \frac{\boldsymbol{a}_{Ca^{2+},s}\,\boldsymbol{a}_{CO_3^{2-},s}}{K_{sp}} \tag{2.21}$$

$\Omega < 1$ then subsaturation (dissolution)

$\Omega = 1$ then equilibrium

$\Omega > 1$ then under saturation (precipitation)

where $\boldsymbol{a}_{i,s}$ refers to the activity of the i^{th} aqueous species adjacent to the mineral surface and K is the equilibrium constant for the $CaCO_3$ dissolution reaction ($10^{-8.48}$). Equation (2.20) has the advantage that in a plot of log R vs. $\log(1-\Omega)$ the intercept with the y axis will equal k^* which is equal to $(k\frac{A}{V})$ and the slope will equal n.

Plummer et al. (1978) suggested that the following reactions occur in parallel during carbonate dissolution under ambient conditions:

$$CaCO_{3(s)} + H^+_{(aq)} = Ca^{2+}_{(aq)} + HCO^-_{3(aq)} \tag{2.22}$$

$$CaCO_{3(s)} + H_2CO^*_{3(aq)} = Ca^{2+}_{(aq)} + 2HCO^-_{3(aq)} \tag{2.23}$$

$$CaCO_{3(s)} + H_2O_{(aq)} = Ca^{2+}_{(aq)} + HCO^-_{3(aq)} + OH^-_{(aq)} \tag{2.24}$$

The first reaction dominating the process of proton attack at pH< 3.5, and the second reaction incorporates the effect of H_2CO_3 at higher pH. In the pH still >7 the third reaction becomes important, which reflects simple hydrolysis of Calcite. Finally the backward precipitation reaction was added:

$$Ca^{2+} + HCO^-_3 = CaCO_{3(s)} + H^+ \tag{2.25}$$

These reactions form the basis for rate equation which covers both dissolution and precipitation:

$$r = \underbrace{k_1 a_{H^+} + k_2 a_{H_2CO_3^*} + k_3 a_{H_2O}}_{r_{fw}} - \underbrace{k_4 a_{Ca^{2+}} a_{HCO_3^-}}_{r_b} \quad (2.26)$$

Where r is the specific rate Calcite dissolution (mmol.cm^{-2}.s^{-1}) separated in forward rate r_{fw} and backward rate r_b and k_1, k_2, k_3 and k_3 are rate constants and a_i refers to the activity of the relevant species (Appelo and postma, 2005).

2.6. Mixing of saltwater-fresh water in coastal carbonate aquifer

Coastal carbonate aquifers have received a special attention not only because of seawater intrusion caused by heavy pumping but also because of the complex and interesting geochemical processes associated with the saltwater mixing zone.

Calcite undersaturation and/or carbonate dissolution has been reported in several mixing zones around the world. Thus, the coastal mixing zone of the Yucatan Peninsula is undersaturated with respect to Calcite and aragonite over a wide range of salinities, and the dissolution of these minerals is considered a major geomorphic process in developing caves, coves and crescent-shaped beaches along the Yucatan coast (Back et al., 1979, 1986; Hanshaw and Back, 1980; Stossell et al., 1989). Ng and Jones (1995) studied the geochemistry of Grand Cayman and found that simple mixing of fresh and seawater could not explain water chemistry of the boreholes, but different processes including dissolution and precipitation of Calcite and dolomite have to be considered. Smart et al. (1988) and Whitaker and Smart (1997) reported the results of chemical and rock profiling through the modern mixing zone on Andros Island in the Bahamas. They show Calcite undersaturation close to the seawater end of the mixing zone intercepted in submarine cavities. These authors postulated that oxidation of organic matter produces additional CO_2 and significantly enhances this undersaturation.

Price and Herman (1991) investigated the geochemical processes occurring within the mixing zone on Mallorca, Spain in relation to the diagenesis of Carbonate minerals and to the development of porosity and permeability within the Pleistocene limestone aquifer. They

suggested that limestone dissolution has occurred based on the enrichment of Calcium in groundwater relative to sea water dilution.

Mixing of seawater or saline subsurface water with fresh calcium carbonate groundwater can be of major importance in the chemical diagenesis of carbonate rocks and sediments (Plummer, 1975). For example, mixing of seawater with $CaCO_3$-saturated groundwaters will cause carbonate dissolution, provided the amount of seawater in the mixture is less than 10%, or the CO_2 content of the groundwater is high. This phenomenon is caused by the superposition of several, and in some cases opposite, effects. Among those effects, the algebraic, salinity, pCO_2, pH and temperature are the most relevant (Plummer et al., 1975; Wigley and Plummer, 1976; Corbella et al., 2003).

If the fraction of seawater in the mixing region is high and CO_2 is low (normal atmospheric partial pressure), however, precipitation of $CaCO_3$ may occur upon mixing with fresh ground waters (Plummer, 1975). These factors could explain the absence of dissolution in the coastal aquifer of Mallorca, Spain (Price and Herman, 1991). Moreover, the presence of other dissolved constituents can lead to $CaCO_3$ precipitation in coastal aquifers (Wicks and Herman, 1996), and in some instances mixtures between fresh and saline waters that are undersaturated with respect to Calcite may be supersaturated with respect to dolomite (Plummer, 1975; González and Ruiz, 1991).

On the other hand, some mixing zones are also reported where Calcite undersaturation does not take place. Plummer et al. (1976) concluded that mixing of fresh and seawater is not significant in controlling Calcite saturation in the Bermudas coast. Most of the groundwater samples from a dune aquifer near Coos Bay, Oregon, and from a coastal carbonate aquifer in Mallorca, were saturated with respect to Calcite and dolomite (Magartiz and Luzier, 1985; Price and Herman, 1991). Wicks et al. (1995) and Wicks and Herman (1996) documented that gypsum dissolution generates a solution capable of precipitating Calcite in the mixing zone of upper Floridian aquifer. Maliva et al. (2001) documented that no change in mineralogy, cement type or porosity can be correlated with current or recent location of a mixing zone in the Biscayne aquifer, Florida. Melim et al. (2002) used evidence from the Neogene from Bahamas to conclude that mixing zone diagenesis includes aragonite dissolution and minor low-magnesium Calcite cementation but does not show the cavernous porosity predicted by the diagenetic models for the mixing zone.

Field evidence of carbonate dissolution is found in coastal aquifers such as the Yucatan Peninsula, Mexico (Back et al., 1979; Stossell et al., 1989), the coastal springs of Greece (Higgins, 1980), and Andors Island in the Bahamas (Smart et al., 1988). Both of the latter cases showed the strong influence of CO_2 content in the water on the amount of $CaCO_3$ dissolved. Carbonate dissolution is linked to the enhancement of porosity and permeability (Hanshaw and Back, 1979).

The above studies reflect that the dissolution potential of carbonates in the mixing zone can be diverse, ranging from cases with no apparent dissolution (Bermudas, Florida) to cases with high dissolution rate (Yucatan, Bahamas). It is interesting to note that the dissolution/precipitation features display some relationship with the water/rock ratio.

Numerical modeling (Sanford and Konikow, 1989a,b) suggests that such porosity and permeability changes exert dynamic feedbacks that cause the zones of mixing and dissolution to change with time.

Hereafter we refer to some experimental investigation of Calcite dissolution by mixing water especially the experimental investigation of Singurindy et al. (2004) who conducted laboratory experiments to examine $CaCO_3$ dissolution and precipitation in saltwater-freshwater mixing zones, with a view to understanding and predicting porosity changes in coastal environments. Two-dimensional flow cells filled with glass beads and crushed calcium carbonate rock were used to measure calcium carbonate precipitation and dissolution, respectively. They used artificial seawater and NaCl solutions of different concentrations under different CO_2 partial pressures and with different mixing ratios. End-member solutions were deionized water and 40g/L NaCl solution, both equilibrated with Calcite at room temperature and atmosphere. Dissolution was evidenced to take place for input mixing ratios of 30 and 50% of saline water by an increase in the measured Ca concentration in the outlet solution with respect to that of the inflow mixture. They observed higher dissolution for the 30%-salty mixing and results were in reasonable agreement with predictions from a relatively simple transport model. However, no quantitative relationship of subsaturation and dissolution extent was shown, due to limitations of the experiment design. Indeed, mixing subsaturation and dissolution did not occur uniformly throughout the flow cell.

Recently, Sanz et al. (2011) investigated the process of Calcite dissolution by mixing waters of different salinities and pCO_2, by means of geochemical modeling and laboratory experiments. The Calcite sample used in their study is Iceland spar from a skarn deposit in Martinet (Eastern Pyrenees, Spain) containing only $CaCO_3$. The crystal was ground and sieved to fractions 125-250μm and 25-53μm. Their laboratory experiments confirmed a strong dependence of the dissolution on the mixing ratio and pointed out the critical role of CO_2 variations at the local atmosphere. The maximum dissolution was observed for mixtures less than 17%-salty, which is attributed to the CO_2 exchange between the reaction cell and the laboratory atmosphere. The reaction cell gains CO_2 for mixtures less than 17%-salty and Calcite dissolution is enhanced with respect to a closed system. The opposite also occurs for mixtures higher than 17% salty.

Rezaei et al. (2005) performed 1- and 2D simulations to gain insight into the processes controlling dissolution rate in the fresh-salt water mixing zone, exploring its sensitivity to the chemistry of end-members and the dispersivity of the medium. In the 1D case, enhanced transport at the freshwater end causes dissolution to concentrate there. However, in the 2D $_{case}$ representative of coastal aquifers, maximum dissolution occurs at the saline side near the discharge zone because of a very active convection cell that develops there, which enhances mixing and thus reaction rates. In their simulation the dissolution causing an increase in permeability that would lead to increased seawater flux and mixing, thus enhancing further dissolution. Guadagnini et al. (2009) applied mixing-ratios based formulation to model mixing-driven dissolution experiments.

2.7. Permeability-porosity evolution induced by geochemical reaction

Singurindy and Berkowitz (2003) investigated the evolution of hydraulic conductivity by precipitation and dissolution in Calcareous sandstone (97.5% $CaCO_3$, 2.5% SiO_2). They used rock samples that were crushed and sieved with relatively uniform particles of 0.85– 0.9 mm size and packed into two types of columns, one of 20 cm length and 2.5 cm diameter and the other of 26.5 cm length and 6.5 cm diameter. They injected different concentrations of HCl/H_2SO_4 mixtures at various flow rates. Because the dissolution of calcium carbonate is a mass transfer limited process, they found that higher flow rates cause a more rapid

dissolution of the porous medium; in such cases, with dissolution dominating, highly conductive flow wormholes were observed to develop. At slower flow rates, no wormhole formation was observed, but the porosity varied in different parts of the columns. Analysis of the sectioned parts of the column, after each experiment, showed that total porosity increased significantly by dissolution of carbonate mineral near the inlet of the column and decreased along the interior length of the column by gypsum precipitation. They also observed fluctuations in both of porosity and hydraulic conductivity of the tested columns. Analysis of the sectioned parts of the column, after experiment, showed that total porosity increased significantly by dissolution of carbonate mineral near the inlet of the column and decreased along the interior length of the column by gypsum precipitation.

Noiriel et al. (2005) studied the hydraulic properties and microgeometry evolution in the course of limestone dissolution by CO_2-enriched water. They observed increase in permeability due to the reduction in pore wall roughness and increasing the pore path connectivity, as also observed on the 3D images. Increasing volumetric flow rate also increases the rate of limestone dissolution at low pH, as the calcite rate of dissolution is enhanced by the transport-processes; dissolution rate increases with flow velocity. The permeability increase appears also more marked when the process is transport-limited because the narrow pore paths, where flow velocity is higher, are more rapidly opened. As a general rule, the permeability increase for transport-limited reaction is more rapid compared to surface-limited reaction.

Noiriel et al. (2009) studied the dynamics of porosity and reactive surface area changes during porous limestone dissolution by CO_2-rich water. They observed a decrease in geometric surface area measured with X-ray microtomography whereas the reactive surface area increases continuously with increasing porosity from 20.3 to 30.2%. They used HYTEC code to model the change in reactive surface areas during the experiment. The model based on spherical-grain dissolution and spherical-pore growth fails to reproduce the experimental results, while the sugar-lump model provides reasonable agreement with the experiment.

Luquot and Gouze (2009) investigated experimentally the porosity and permeability changes induced by injection of CO_2 into carbonate rocks where a set of reactive flow-through experiments at temperature 100 °C and total pressure 12 MPa was performed in limestone

reservoir samples. The dissolution experiments display a power scaling between permeability and porosity with distinctly different scaling exponents characterizing the reactivity of the fluid percolating the sample, independently from the decrease with time of the reactive surface area.

Gouze and Luquot (2011) characterized the links between the dissolution mechanisms that control the porosity changes and the related changes of the reactive surface area and of the permeability. They used X-ray microtomography to characterize the porosity, permeability and reactive surface changes during dissolution. Their results showed that the increase of permeability is due to the decrease of the tortuosity for homogeneous dissolution, whereas it is due to the combination of tortuosity decrease and hydraulic radius increase for heterogeneous dissolution.

Chapter 3

Geochemical modeling of different factors affecting Calcite dissolution by mixing waters

3. Geochemical modeling of different factors affecting Calcite dissolution by mixing waters

Summary

Simulation of different factors and conditions controlling the dissolution of Calcite using PHREEQC geochemical code are presented. Two different wide known thermodynamic data bases were implemented to calculate the activity coefficient. The first one is PHREEQC data base which uses Debye Hückel expressions and the second is Pitzer data base which is based on ion activity approach. Two different end member solutions were used to represent mixing of fresh and salty groundwater while, both at equilibrium with Calcite and different levels of partial pressure of CO_2. Results indicated that Pitzer model is more appropriate when dealing with Sodium Chloride dominant system. Solution resulted from mixing both end member solution show undersaturation with low and moderate ionic strength, pCO_2, salinity of salt end member solution increasing and the mixture of slightly acidic fluids is more easily subsaturated than the mixture of more basic ones. Results demonstrated that the maximum subsaturation is expected to occur for mixing ratios of about 15%, while the expected dissolved Calcite reaches its maximum for 45% of mixing. This apparent inconsistency can be explained by the strong influence of the pH in the carbonate speciation, the relative lower activity of CO_3^{2-} compared to that of Ca^{2+} in solution, and the dependency of the activity coefficients with the mixing ratio (i.e., with the salinity variation).

3.1. Mixing process in Carbonate aquifer

Coastal aquifers are generally composed of carbonate materials. The theory of carbonate subsaturation by mixing has been extensively used to interpret carbonate dissolution textures found in caves and borehole samples from coastal environments (Plummer, 1975). Additionally, reactive transport modeling exercises have demonstrated that important porosity development may occur at the salt water-fresh water mixing zone of coastal aquifers on a geological time scale (Sanford and Konikow, 1989a,b; Rezaei et al., 2005, Romanov and Dreybrodt, 2006). Mixing of two fluids with different salinity has also been used as a

hypothesis to explain deep dissolution of carbonates and the formation of hydrothermal mineral deposits (Corbella et al., 2004).

When mineral solutions of different compositions are mixed, the molalities and activities of individual ions in the mixture are often non-linear functions of their end-member values. This non-linearity is particularly significant in determining mineral saturation levels. Mixtures of saturated solutions may be either undersaturated or supersaturated depending on the end-member compositions and the physical conditions in which end-members and their mixtures exist. In carbonate solutions important non-linear effects occur due to redistribution of carbonate species. Mixing of Calcite-saturated ground waters may lead to under-saturated solutions thus having a potential for Calcite dissolution in carbonate formations. This phenomenon is caused by the superposition of several, and in some cases opposite, effects. Among those effects, the algebraic, salinity, pCO_2, pH and temperature are the most relevant (Plummer et al., 1975; Wigley and Plummer, 1976; Corbella et al., 2003).

Here the saturation state will be given as Ω, which is the ratio of the ion activity product (IAP) to the solubility product (K_{sp}) for the solid ($\Omega = IAP/K_{sp}$) (see equation (2.21)).

A common one is the ‘‘saturation index’’, SI, which is generally equal to log Ω. The extent of disequilibrium is then simply the difference between Ω and 1. Thus, for undersaturation it must range from 0 to 1, whereas for supersaturation it can range from 0 up to numbers substantially > 1 (Morse and Berner, 1979; Morse, 1983; Morse and Arvidson, 2002).

In this context the different factors and conditions controling the dissolution of Calcite were simulated using PHREEQC a Computer Program for Speciation, Batch-Reaction, One Dimensional Transport, and Inverse Geochemical Calculations (Parkhurst and Appelo, 2006). The program is based on equilibrium chemistry of aqueous solutions interacting with minerals, gases, solid solutions, exchangers, and sorption surfaces.

PHREEQC is based on the FORTRAN program PHREEQE (Parkhurst et al., 1980). PHREEQE was capable of simulating a variety of geochemical reactions for a system including mixing of waters, addition of net irreversible reactions to solution, dissolving and precipitating phases to achieve equilibrium with the aqueous phase, and effects of changing temperature.

PHREEQE calculated saturation indices, concentrations of elements, molalities and activities of solid, aqueous and gaseous species, pH, pe and mole transfers of phases to achieve equilibrium as a function of specified reversible and irreversible geochemical reactions.
PHREEQC includes different data base generated by different aqueous models to calculate the activity coefficient of different species.

3.1.1. Activity coefficient calculation

Two different wide known thermodynamic data base were examined. The first data base is based on the Davis and Debye Hückel expressions (Parkhurst and Appelo, 2006) and the second one is based on ion interaction approach for calculating activity coefficient (Pitzer, 1979; Harvie and Weare, 1980; Harvie et al., 1984; Plummer et al., 1988; Rard and Wijesinghe, 2003; Parkhurst and Appelo, 2006).

3.1.1.1. Davis and Debye Hückel expressions

Default PHREEQC data base which uses ion-association equation given by Davis and Debye Hückel expressions to account for the non-ideality of aqueous solutions. This type of aqueous model is adequate at low ionic strength but may break down at higher ionic strengths as in the range of seawater and above (Parkhurst and Appelo, 2006).
Activity coefficients (γ_i) of aqueous species are defined with the Davies equation:

$$\log \gamma_i = -Az_i^2 \left(\frac{\sqrt{I}}{1-\sqrt{I}} - 0.3I \right) \tag{3.1}$$

or the extended or WATEQ Debye-Hückel equation:

$$\log \gamma_i = -\frac{Az_i^2\sqrt{I}}{1+Ba_i^o\sqrt{I}} + b_i I \tag{3.2}$$

where z_i is the ionic charge of aqueous species i, I is the Ionic strength and A and B are constants dependent only on temperature. Equation (3.2) is the extended Debye-Hückel equation, if b_i is zero, or the WATEQ Debye-Hückel equation, if b_i is not equal to zero. In the extended Debye-Hückel equation, a_i^o is the ion-size parameter, whereas in the WATEQ

Debye-Hckel equation a_i^o and b_i are ion-specific parameters fitted from mean-salt activity-coefficient data.

In sodium chloride dominated systems, the model may be reliable at higher ionic strengths. For high ionic strength waters, the specific interaction approach to thermodynamic properties of aqueous solutions should be used (Pitzer, 1979; Rard and Wijesinghe, 2003; Parkhurst and Appelo, 2006).

3.1.1.2. Pitzer Model (Ion interaction approach)

Pitzer, (1979) presented a treatment of the aqueous model based largely on ion interaction approach as presented by Harvie and Weare (1980) and Harvie et al. (1984) who demonstrated that Pitzer's model could be used to reliably model the solubilities of solutes present in complex, highly concentrated, natural brines, and to model the diagenetic precipitation sequences resulting from evaporation of diverse types of natural waters. Several years later, Plummer et al. (1988) wrote a geochemical modeling code named PHRQPITZ that incorporated both Pitzer's model and the computational approach of Harvie et al. (1984). Plummer et al. (1988) made this code PHRQPITZ widely available to the scientific community.

The original version of Pitzer's ion interaction model contains an ionic-strength dependent virial coefficient for two-ion interactions, but the virial coefficient for three-ion interactions is set to an empirically determined constant value.

Extended versions of the ion-interaction model are now in common use, where the virial coefficient for three-ion interactions is also allowed to depend on the ionic strength, and terms for higher-order interactions may also be included (Rard and Wijesinghe, 2003). Mean activity coefficients of a single electrolyte are given by:

$$\begin{aligned}\ln \gamma_{\pm}^{P} = &-|z_M z_X| A_{\phi}\{I^{1/2}/(1+bI^{1/2}) + (2/b)\ln(1+bI^{1/2})\} + \\ &(2\nu_M\nu_X/\nu)m\big[2\beta^{(0,P)}(M,X) + \\ &2\{\beta^{(1,P)}(M,X)/\alpha_1^2 I\}\{1-\left(1+\alpha_1 I^{1/2}-\alpha_1^2 I/2\right)exp(-\alpha_1 I^{1/2})\}\big] + \\ &\{3(\nu_M\nu_X)^{3/2}/\nu\}m^2 C^{\phi,P}(M,X).\end{aligned} \tag{3.3}$$

where, M denotes the cation and X the anion; m is the stoichiometric molality; b = 1.2 $kg^{1/2}.mol^{-/2}$; A_ϕ is the Debye–Hückel limiting law slope for ϕ; I is the stoichiometric, molality-based, ionic strength; z_M and z_X are the valences of ions M and X; ν_M and ν_X are the number of M and X ions formed by complete dissociation of one molecule of the solute $M_{\nu M}$, $X_{\nu X}$; and $\nu = \nu_M + \nu_X$ is the stoichiometric ionization number of the total electrolyte. The coefficient α_1 is usually assigned a value of $\alpha_1 = 2.0$ $kg^{1/2}.mol^{-1/2}$; $\beta^{(0)}$ (M, X), $\beta^{(1)}$ (M, X) and C^ϕ are parameters representing the ion interactions for Pitzer model.

3.1.2. End member solutions

Two different end member solutions were used to represent the fresh and salty groundwaters both at equilibrium with Calcite and different levels of partial pressure of CO_2. Those two end member solution were mixed at different mixing ratios as shown in Table (3.1).

Table 3.1: **Input end member solution and in between mixed solution at different mixing ratios used in numerical simulation**

Mixing ratio (%)	pH	Ca tot (mol)	C tot (mol)	Na tot (mol)	Cl tot (mol)	PCO_2 Bar	Ω $CaCO_3$	Ionic strength
0*	8.27	5.30×10^{-4}	1.05×10^{-3}	0	0	$10^{-3.5}$	1	1.58×10^{-3}
15	7.81	1.01×10^{-3}	2.04×10^{-3}	1.50×10^{-1}	1.50×10^{-1}	$10^{-2.86}$	0.35	1.53×10^{-1}
45	7.53	2.11×10^{-3}	4.34×10^{-3}	4.50×10^{-1}	4.50×10^{-1}	$10^{-2.34}$	0.53	5.06×10^{-1}
100**	7.38	3.70×10^{-3}	7.62×10^{-3}	1.00	1.00	$10^{-2.0}$	1	1.011

* Mixing ratio=0, (fresh end member solution).
** Mixing ratio=100, (salt end member solution).

The saturation state, molalities and activities of different species included were calculated as a function of mixing ratio under different levels of PCO_2, salinity, pH and temperature in order to evaluate the Calcite saturation state under different experimental conditions.

First we show the difference between Davis and Debye Hückel expressions (Parkhurst and Appelo, 2006) and ion interaction approach for calculating activity coefficient (Pitzer, 1979; Harvie and Weare 1980; Harvie et al., 1984; Plummer et al., 1988; Rard and Wijesinghe, 2003).

The saturation state of Calcite under different mixing ratios between the two end member solutions used in the current simulations shows higher values of saturation when using

Hückel model than those values of saturation when using Pitzer model (Figure 3.1). This difference is clearly noted when mixing ratio increases and is in agreement with Rard and Wijesinghe (2003) and Parkhurst and Appelo (2006) who mentioned that Pitzer model is more appropriate when dealing with Sodium Chloride dominant system.

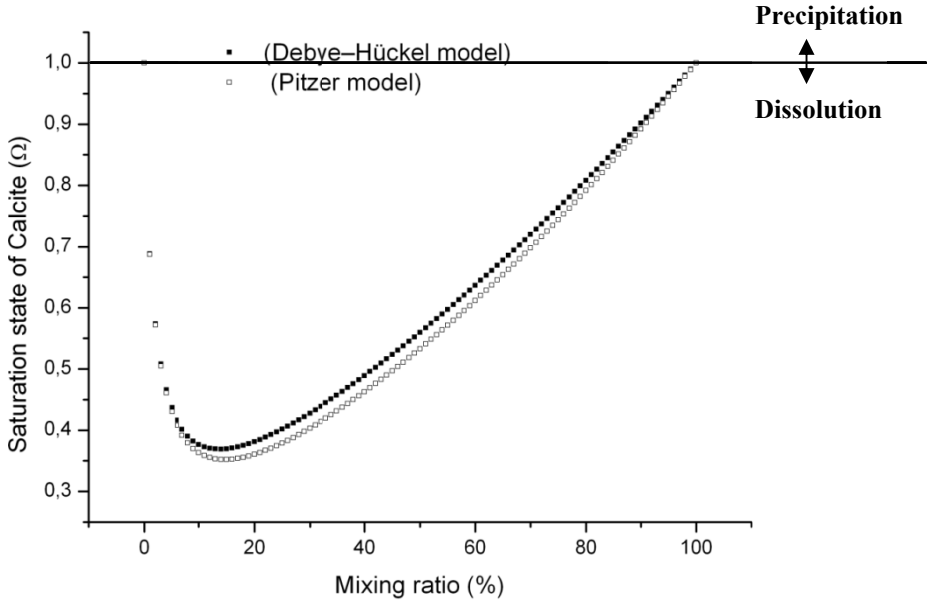

Figure 3.1: Comparison between both Pitzer and Debye-Hückel models in calculation of Calcite saturation (salinity increases to right).

3.1.3. Simulation of different conditions affecting saturation state of Calcite

As Pitzer model is more appropriate when dealing with Sodium Chloride dominant system hence, during all onward simulation, the Pitzer model is implemented. Among those effects that we examine are the algebraic, salinity, pCO_2, pH and temperature which are the most relevant factors affecting Calcite dissolution by mixing water.

3.1.3.1. Algebraic effect

The algebraic effect refers to the non-linearity of the ion activity product at equilibrium (K_{eq}) with respect to the mixing ratio, compared to the linear variation of total species concentrations. This causes oversaturation of mixtures, even if end members are in

equilibrium, because the ion activity product (IAP) of any linear mixture is always higher than K_{eq} (Figure 3.2).

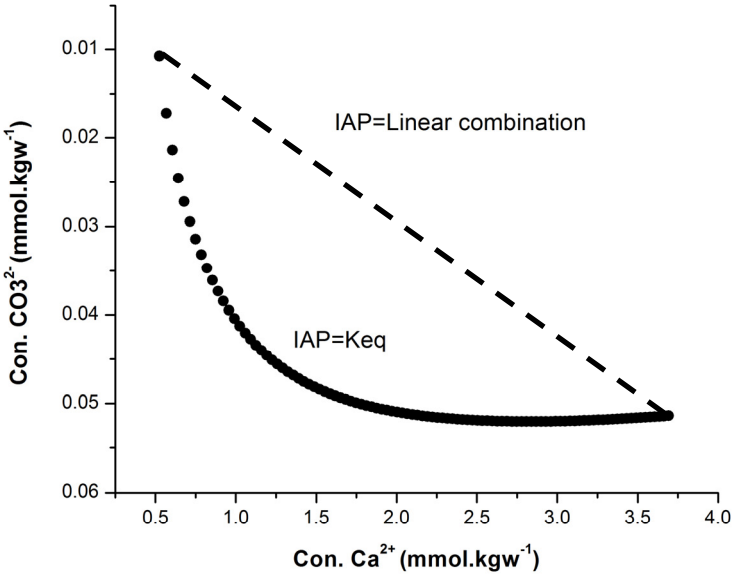

Figure 3.2: Carbonate vs Calcium species concentration when IAP = K_{eq} and when IAP is equal to the linear combination which demonstrates the algebraic effect (Pitzer model).

3.1.3.2. Salinity effect and salinity degree

The salinity effect (also called Ionic strength effect) occurs when two solutions having different salinity are mixed together. The resulting solution is subsaturated in Calcite as a consequence of the non-linear dependence of the ion activity coefficients with ion strength especially at low to moderate ion strengths. Because the activity coefficient of ions in a mixture is less than that of the linear combination of the end-member solutions, the mixture presents a higher solubility of Calcite and therefore is undersaturated as shown in Figure (3.3). The saturation state of Calcite as a function of mixing ratio was simulated at three different salinities of salty end member solutions where NaCl concentration ranged from 1 to 3 mol.kgw^{-1}, all are equilibrated with Calcite and pCO_2 of 10^{-2} bar while the fresh end member solution is equilibrated with Calcite too but at the atmospheric pCO_2 of $10^{-3.5}$ bar. The results indicated that when the salinity of the salty solution increased, the Calcite

saturation state decreased at different mixing ratio of end member solutions which confirms the salinity effect on saturation state of Calcite as shown in Figure (3.4).

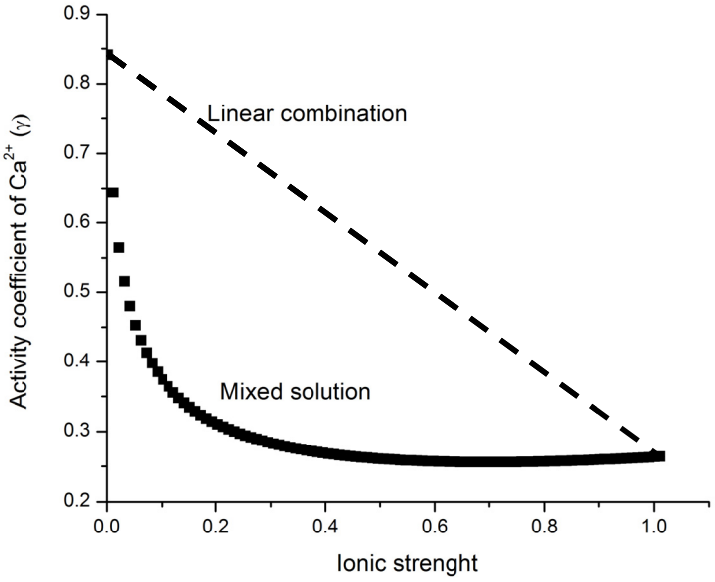

Figure 3.3: Activity coefficient of Calcium species vs Ionic strength for mixed two end member solutions and linear combination which demonstrates the ionic strength effect (Pitzer model).

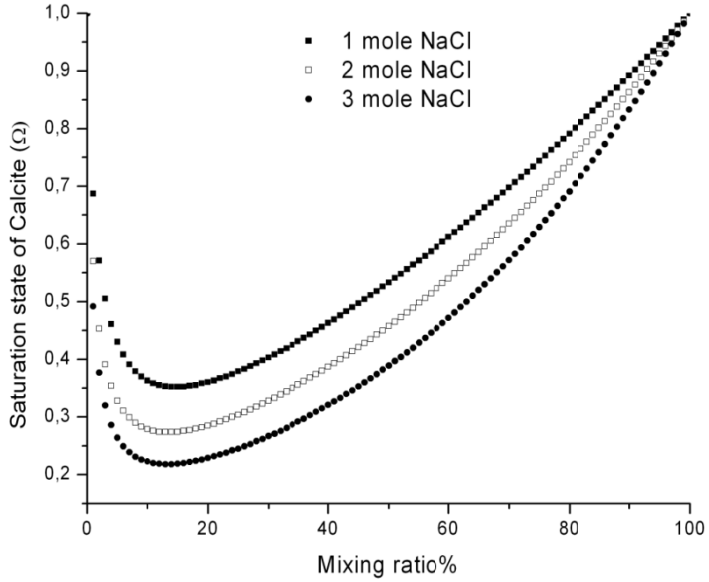

Figure 3.4: Calcite saturation state as a function of mixing ration at different level of salinity of the salty end member solutions.

3.1.3.3. Partial pressure of CO_2 and pH

The saturation of a mixture also depends on the pCO_2 and pH because of the strong dependence of the carbonate species with pH (Figure 3.5). Thus, the CO_3^{2-} concentration will be higher under slightly basic conditions than under acidic ones. Therefore, the mixture of slightly acidic fluids will be more easily subsaturated than the mixture of more basic ones.

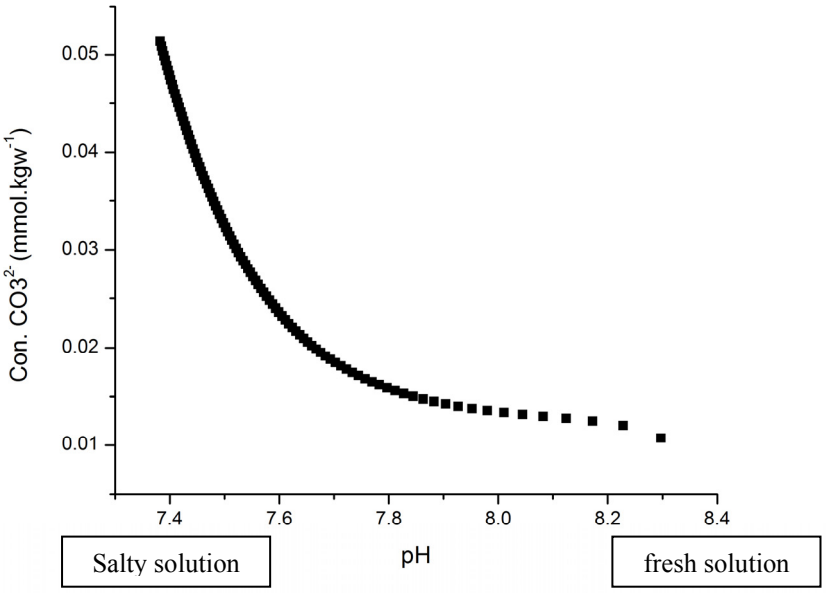

Figure 3.5: Concentration of carbonate species as a function of pH at different mixing ratio between salt and fresh end member solution (note that salinity decrease to right).

The saturation state of Calcite shows different degrees of saturation when the pCO_2 of the salty end member solution increased where the fresh end member is kept at atmospheric pCO_2, hereafter the saturation state of Calcite as a function of mixing ratio at different pCO_2 was simulated and the pH profile for the different pCO_2 was plotted with the mixing ratio as shown in Figures (3.6), (3.7).

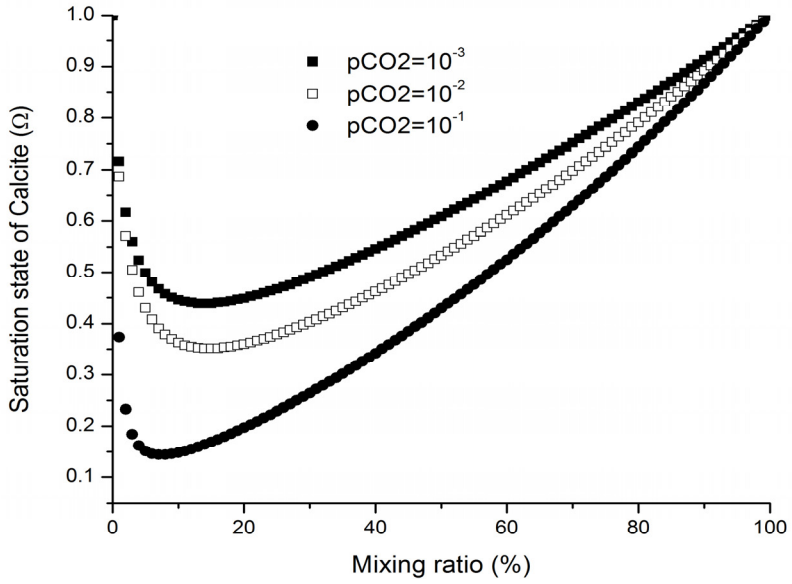

Figure 3.6: Saturation state as a function of mixing ratio at different level of pCO_2 of the salty end member solution where pCO_2 of fresh end member solution is $10^{-3.5}$ bar.

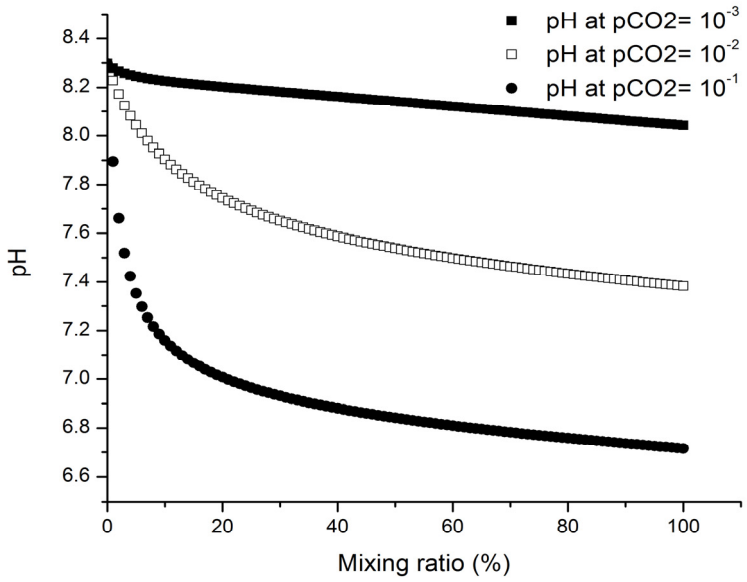

Figure 3.7: pH profile as a function of mixing ratio at different level of pCO_2 of the salty end member solution where pCO_2 of fresh end member solution is $10^{-3.5}$ bar.

3.1.3.4. Temperature effect

Finally, temperature variations may also affect the saturation of a mixture due to the non-linear dependence with the mineral equilibrium constants. However in non-geothermal groundwaters, temperature variations exceeding 10ºC are not expected within the range of a few meters (the scale of the carbonate cavities) and the temperature effect becomes practically negligible in such environments (Corbella and Ayora, 2003). The saturation state decreases with temperature especially for low mixing ratio.

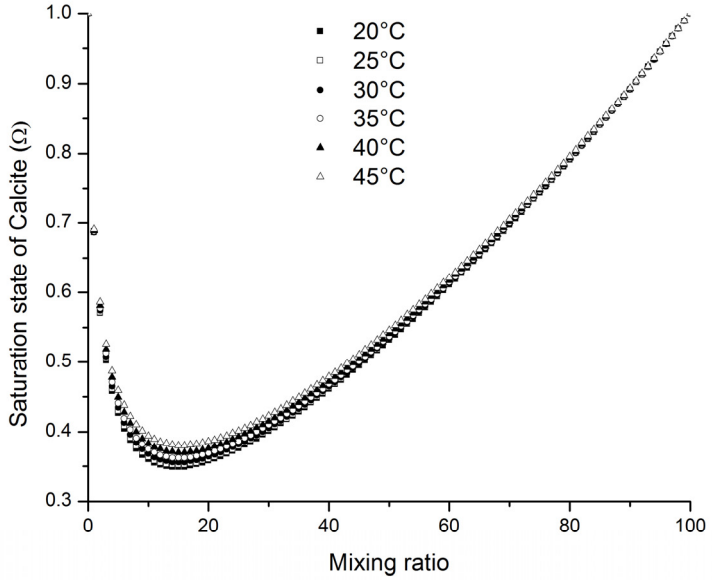

Figure 3.8: Saturation state of Calcite as a function of mixing ration for different temperatures.

3.1.4. Calcite saturation as an indicator of potential dissolution

Sanz et al. (2011) studied the Calcite dissolution by mixing water, they stated that in a closed system, the maximum subsaturation occurs for mixing ratios of about 15%-salty, while the dissolved Calcite is maximum for 50%-salty because the dissolution is affected by carbonate speciation, and by the dependence of activity coefficients on salinity as shown before in Figure (3.3). Their laboratory experiments confirmed a strong dependence of the Calcite dissolution on the mixing ratio and pointed out the critical role of CO_2 variations at the local atmosphere. The maximum dissolution was observed for mixtures less than 17%-salty, which

is attributed to the CO_2 exchange between the reaction cell and the laboratory atmosphere. The reaction cell gains CO_2 for mixtures of less than 17%-salty and Calcite dissolution is enhanced with respect to a closed system. The opposite also occurs for mixtures higher than 17%- salty solution. Including CO_2 exchange, both calculations and dissolution experiments at different flow rates demonstrated a high sensitivity of the amount of Calcite dissolved to minor variations of CO_2 partial pressure of the local atmosphere

The selection of the two end-member solutions (Table 3.1) was proposed on the basis of a plausible seawater intrusion mixing zone in natural coastal aquifers (Rezaei et al., 2005).

Simulation results are presented in Figure (3.9) in terms of variation of the Calcite saturation and dissolved Calcite up to equilibrium with respect to the mixing ratio. It is shown that the maximum dissolution is calculated to occur for a mixing ratio of about 45% while the higher subsaturation is obtained for a mixing ratio of 15%.

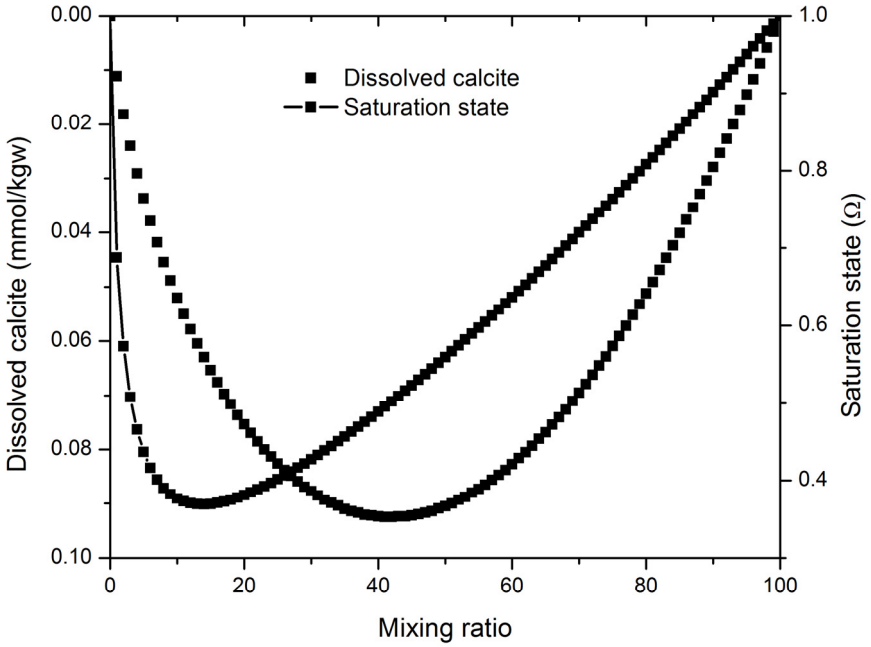

Figure 3.9: Computed input saturation state and dissolved Calcite after reaction to equilibrium for mixtures of the two solutions described in Table (3.1).

Chapter 4

Materials and Methods

4. Materials and Methods

4.1. Description of the tested rock samples

In the present study, the tested Carbonate samples were taken from two different sites, the first site is a Miocene reef drilled to 100 m-dept near Campos, in the SE part of Mallorca 6 km away from the coast in Spain. The second site is the Lavoux (central France). The selection of the samples was based on geometrical, petrophysical and chemical characteristics; hereafter we shall browse a description for both Mallorca and Lavoux samples.

4.1.1. Mallorca samples

The first limestone samples were taken from Campos site which is located in the South East part of Mallorca, 6 km away from the present sea-shore, where the tested samples were cored from the MC10 at 94 m depth as mentioned in Figure (4.1).

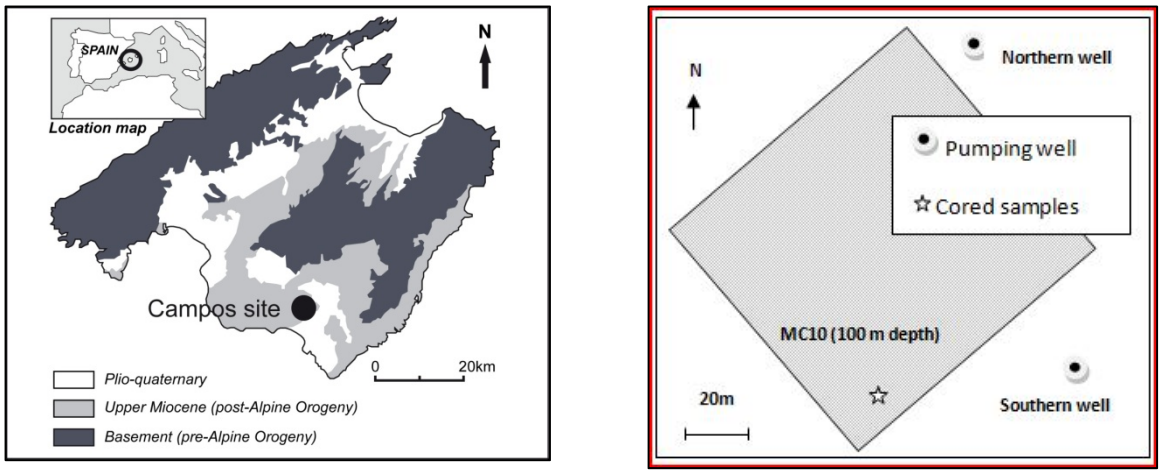

Figure 4.1: The Campos site at Mallorca and the MC10 cored observation well where Mallorca sample were taken at 94 m depth.

The geological structure of the site is that expected for a Miocene reef, with lagoonal and platform-like structures at the top, karstified reefal constructions in the middle and slope deposits at the base. Similar structures are exposed along the coast, at Cabo Blanco, a 100

meters high cliff. The high heterogeneity of the formation has a major impact on fluid flow and the freshwater/saltwater transition zone.

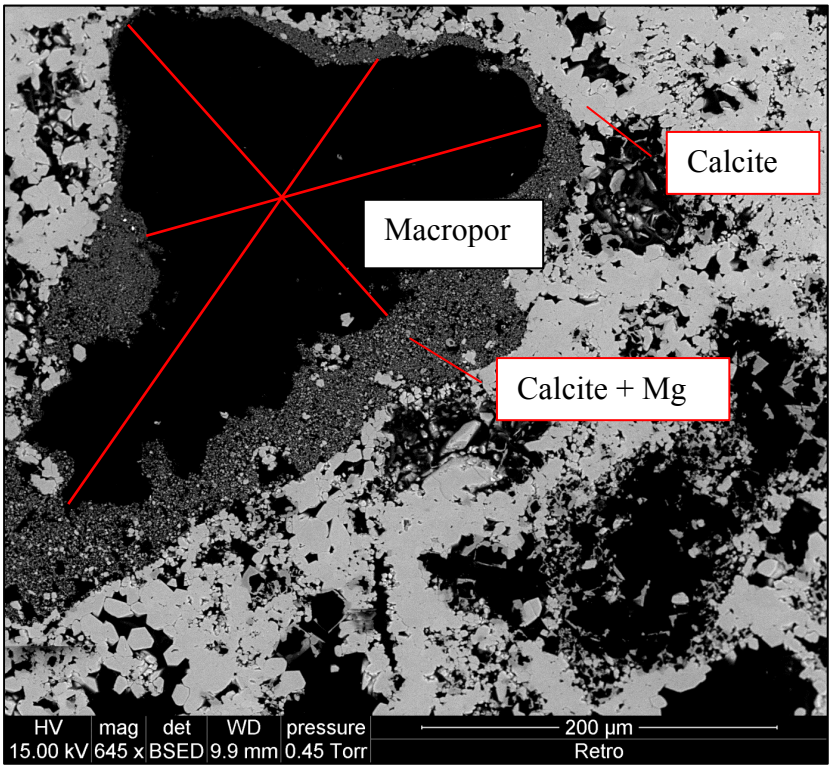

Figure 4.2: SEM image of Mallorca sample (MC10_94 m depth).

The X-ray diffraction (XRD) and The Scan Electron Microscopy (SEM) analyses which represents the crystallographic, chemical composition and physical properties of the sample were carried out at Geosciences Montpellier laboratories (Montpellier - France), the results show that chemical composition of Mallorca sample MC10 at 94m includes two main minerals, Calcite and Dolomite (Calcite with Magnesium). Mallorca samples show in general a high level of heterogeneity in terms of structure and chemical composition. One can observe the structure heterogeneity of Mallorca sample in figure (4.2) the white color is corresponding to the Calcite grains whereas the grey one represents the Dolomite grains which is smaller than the Calcite grains, the black color shows the pore shape and surrounding it the Dolomite grains.

4.1.2. Lavoux samples

The second limestone samples were taken from Lavoux Parisian basin which is fine and homogeneous rocks, it comes from a limestone quarry located in the South-west of the Parisian basin near Poiliters. The samples contain some grain stone with Peloids, Oolits, bioclasts and algae (Honeyborne, 1982; Ioannou et al., 2004). Figure (4.3) shows the homogeneous structure of Lavoux samples. These sample are quiet homogenous but it is less permeable than Mallorca sample.

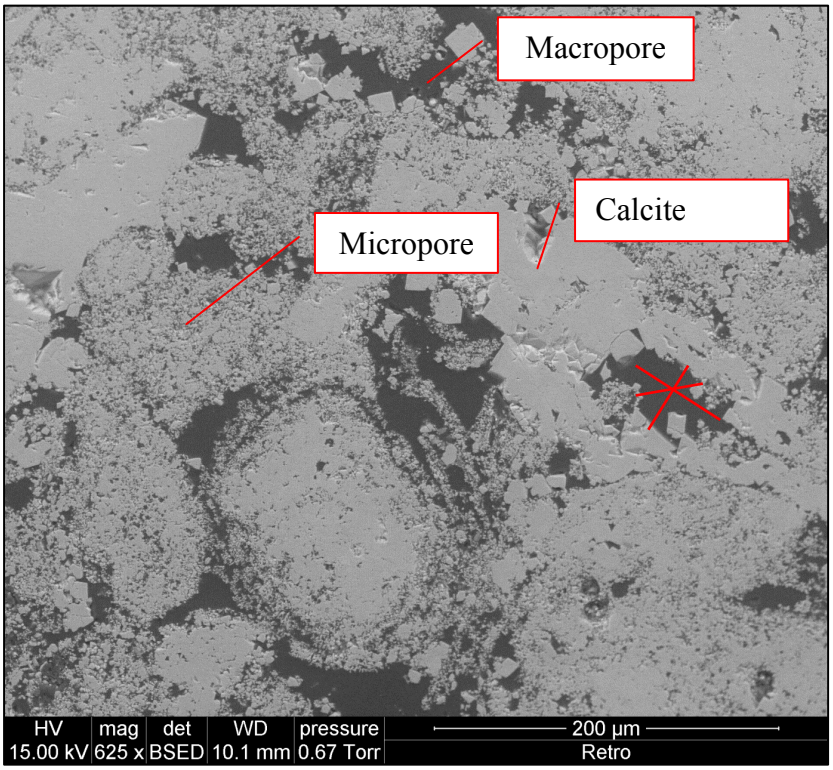

Figure 4.3: SEM image shows the homogeneous structure of Lavoux samples.

One can observe that the distribution of pores of Lavoux samples is more homogeneous than those for Mallorca samples as we will see here after.

The X-ray diffraction (XRD) and The Scan Electron Microscopy (SEM) analyses which represent the crystallographic, chemical composition and physical properties of the sample were carried out at University of Montpellier laboratories (Montpellier - France).

4.2. The analytical techniques of the tested samples

4.2.1. Scan electron microscopy (SEM)

The scanning electron microscope (SEM) uses a focused beam of high-energy electrons to generate a variety of signals at the surface of solid specimens. The signals that derive from electron-sample interactions reveal information about the sample including external morphology (texture), chemical composition, and crystalline structure and orientation of materials forming the sample. In most applications, data are collected over a selected area of the sample surface, and a 2-dimensional image is generated displaying spatial variations of these properties (Goldstein, 2003). Areas ranging from approximately 1 cm to 5 microns in width can be imaged in a scanning mode using conventional SEM techniques (magnification ranging from 20X to approximately 30000X, spatial resolution of 50 to 100 nm).

The SEM is also capable of performing analyses of selected point locations on the sample surface; this approach is especially useful in qualitatively or semi-quantitatively determining chemical compositions (using EDS), crystalline structure, and crystal orientations (using EBSD). The fundamental principles of SEM is based on accelerated electrons in a SEM carrying significant amounts of kinetic energy, and this energy is dissipated in a variety of signals produced by electron-sample interactions when the incident electrons are decelerated in the solid sample. These signals include secondary electrons (that produce SEM images), backscattered electrons (BSE), diffracted backscattered electrons (EBSD that are used to determine crystal structures and orientations of minerals), photons (characteristic X-rays that are used for elementary analysis and continuum X-rays), visible light (cathodolumine scence- CL), and heat.

Secondary electrons and backscattered electrons are commonly used for imaging samples: secondary electrons are most valuable for showing morphology and topography of samples and backscattered electrons are most valuable for illustrating contrasts in composition in multiphase samples (i.e. for rapid phase discrimination). X-ray generation is produced by inelastic collisions of the incident electrons with electrons in discrete ortitals (shells) of atoms in the sample. Some of the tested samples were scanned by SEM before and after percolation experiments. Hereafter, we present the SEM images before the experiments.

4.2.1.1. SEM description of Mallorca samples MC10_94 m

In order to perform a SEM test, samples were prepared at the Geosciences Montpellier laboratories where a thin section was taken from a representative sample of Mallorca at MC10_94 m depth.

Thin sections were prepared by fixing a billet of the rock to a glass slide and then lapping it to 30 microns in thickness. In order to prepare the thin section for SEM analysis, it is polished down to 1 micron grit. Then each thin section was scanned with SEM system at the Geosciences Montpellier laboratories. Hereafter we report some SEM images of Mallorca samples that were taken from the same location of those used in the percolation experiments. The images were taken at different resolutions in which we can observe the structure heterogeneity in addition to significant rock properties, pores, pore throats, framework grains and cements as well as elemental abundance from EDS analysis.

The chemical analysis of the tested section, where we can see that light grey color represents Calcite with low Magnesium 0.83 % content whereas the dark grey color represents Calcite with high Magnesium content 5.81 % based on Energy Dispersive Spectrometer (EDS) analysis as reported in Table (4.1).

Figure (4.4) illustrates the distribution of Calcite (light grey color) and Dolomite (dark grey) in additional to the pores shapes (dark color). The spectrums were taken during the SEM analysis indicate that the matrix is formed by two types of minerals: calcite and dolomite or Mg-calcite. The pore feature is typical of a dissolution process, with big “smooth” pores (150- 450 μm) and a low micro pores (pore size 0.5 μm).

Table 4.1: EDS chemical analysis of Mallorca.

Element	Light grey color (Atomic %) Spectrum 1	Dark grey color (Atomic %) Spectrum 2
C	28.24	28.31
O	56.98	57.01
Mg	0.83	5.81
Ca	13.93	8.87

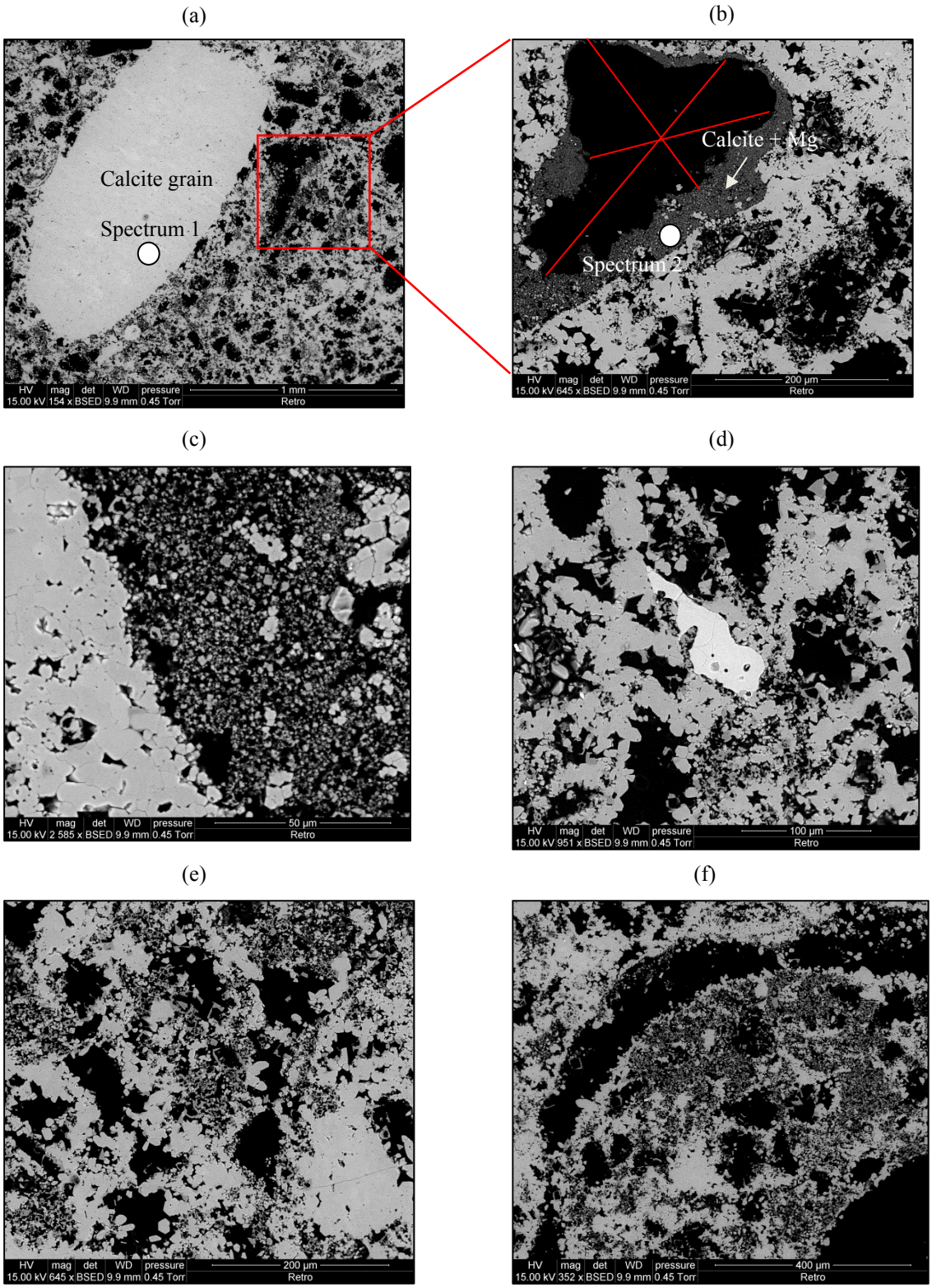

Figure 4.4: Scan electron Microscopy (SEM) images of MC10_94m depth, (a) 1 mm resolution image representing Calcite grain (light grey color), Pores (dark color) surrounding with Calcite enriched with Dolomite (dark grey color), (c), (d), (e), (f), represent the structure heterogeneity at different resolution levels of 50, 100, 200, 400 microns.

4.2.1.2. SEM description of Lavoux sample.

Lavoux samples are mainly composed of 99.7 % of Calcite with a very little amount of Calcite containing Magnesium. The spectrums were taken during the SEM analysis indicate that the matrix is formed by almost Calcite mineral. Table (4.2) summarize the chemical analysis of a tested section in which we can see that both white color and light grey color represent nearly the same abundance of Calcite based on Energy Dispersive Spectrometer (EDS) analysis. That confirms the homogeneity of chemical composition of Lavoux samples.

Table 4.2: EDS chemical analysis of Lavoux.

Element	White color (Atomic %) Spectrum 1	Grey color (Atomic %) Spectrum 2
C	40.28	42.00
O	46.82	46.28
Mg	0.21	0.18
Ca	12.69	11.53

Figure (4.5) illustrates the homogenous distribution of Calcite grains in additional to the pores shapes (dark color). The microspores features are represented in light grey. It is typical of relatively big “smooth” pores (20-50 μm) and small micro pores (pore size 0.5 μm).
The homogeneity in terms of structure and porosity distribution can be seen in Figure (4.5 a,b,c,d,f) at different resolution levels. One can see that there are some algae presented in Figure (4.5 b, d). In general, Lavoux samples were considered as homogenous porous media in terms of porosity distribution and mineral composition.

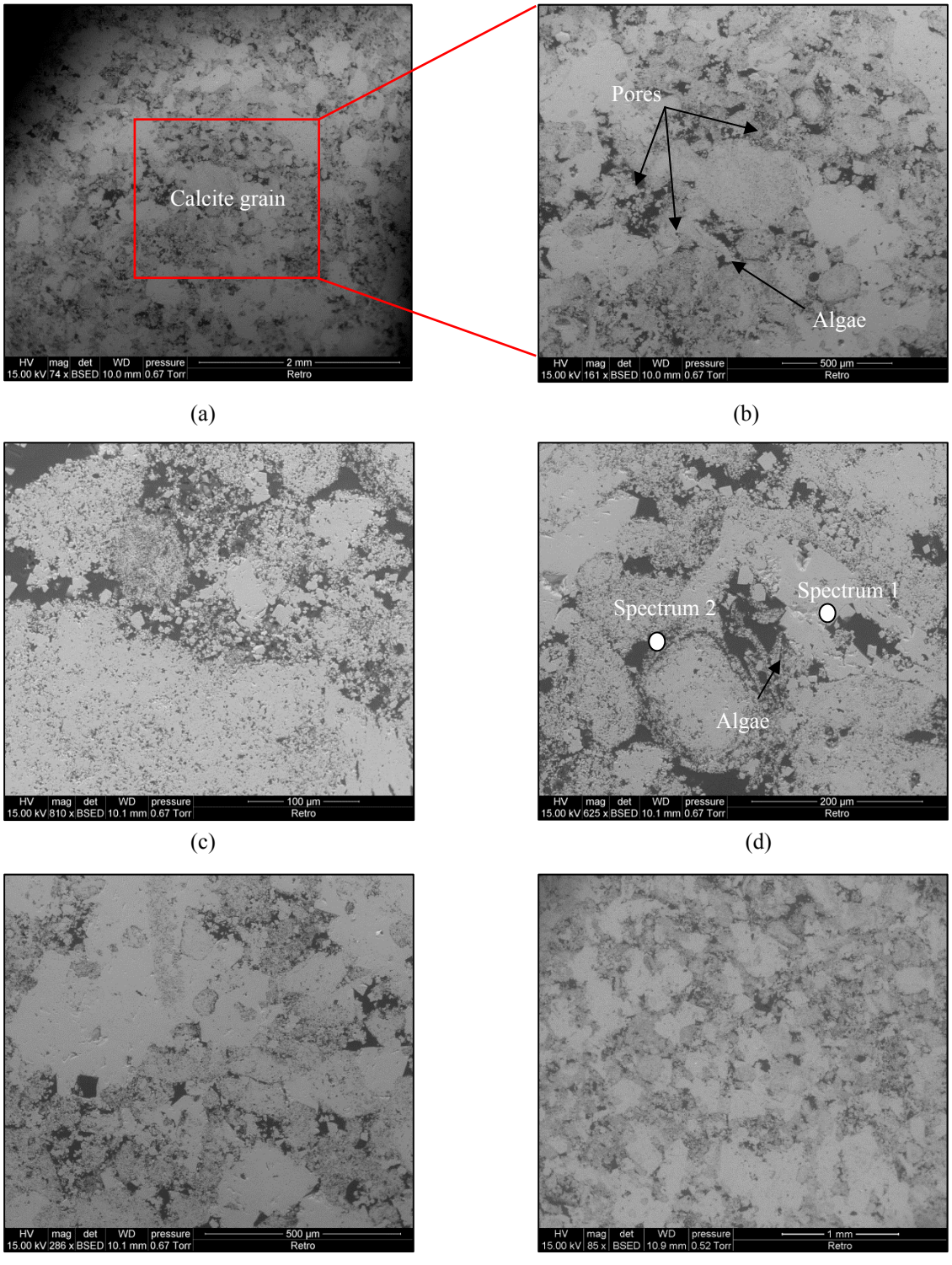

Figure 4.5: Scan electron Microscopy (SEM) images of Lavoux, (a) 2 mm resolution image representing Calcite structure, (b) Calcite grain (light grey color), Pores (dark color) surrounding and Algae found in the this section; (c), (d), (e), (f), represent the structure homogeneity at different resolution levels of 100, 200, 500 microns and 1 mm.

4.2.2. X-Ray Diffraction Method (XRD):

X-ray diffraction is based on constructive interference of monochromatic X-rays and a crystalline sample. These X-rays are generated by a cathode ray tube, filtered to produce monochromatic radiation, collimated to concentrate, and directed towards the sample.

The interaction of the incident rays with the sample produces constructive interference (and a diffracted ray) when conditions satisfy Bragg's Law ($n \lambda = 2\ d \sin\theta$). This law relates the wavelength of electromagnetic radiation to the diffraction angle and the lattice spacing in a crystalline sample. These diffracted X-rays are then detected, processed and counted. By scanning the sample through a range of 2θ angles, all possible diffraction directions of the lattice should be attained due to the random orientation of the powdered material. Conversion of the diffraction peaks to d-spacings allows identification of the mineral because each mineral has a set of unique d-spacings.

The results indicated that the chemical composition of Lavoux samples is about 99.7% Calcite and about 0.3% Calcite with Magnesium. Figure (4.6) indicates standard XRD analysis of Calcite power and the XRD analysis of Lavoux sample. The diffraction peaks and d-spacings identify the Calcite mineral (C,O,Ca) with non significant Mg content.

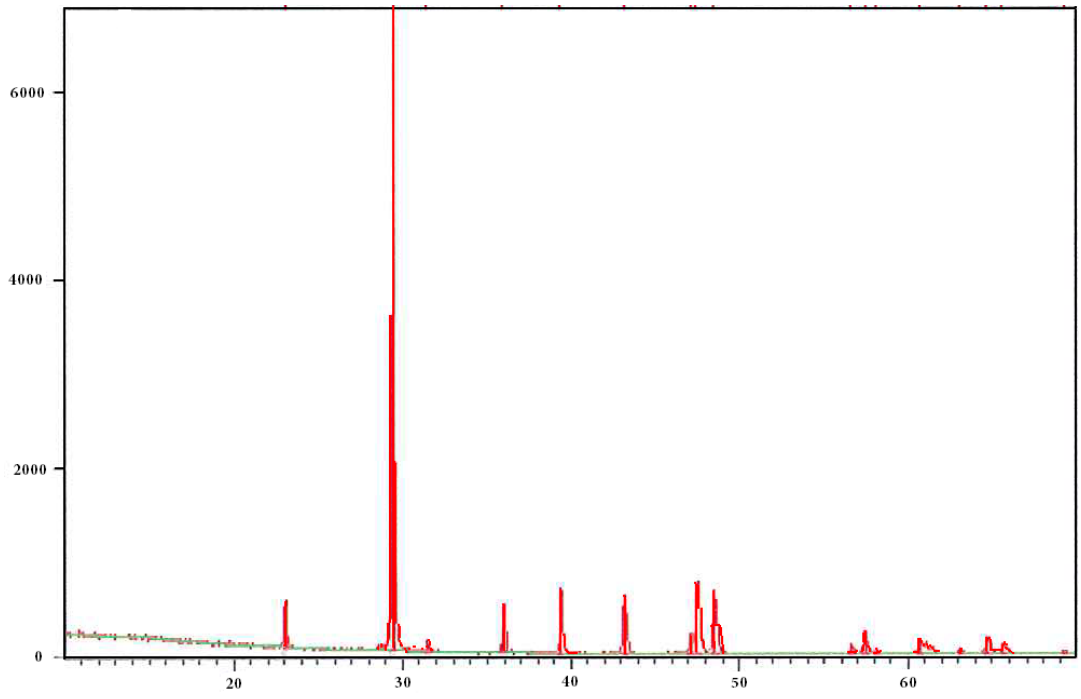

Figure 4.6: X-Ray Diffraction analysis of Lavoux samples.

4.2.3. X-Ray Micro Tomography (XRMT)

Recent advances in X-ray computed microtomography (XRMT) have considerably improved the direct measurement of multi-granular porous media structure (Coker et al., 1996; Lindquist et al., 1996; Delerue et al., 1999; Lindquist and Venkatarangen, 1999; Lindquist et al., 2000; Taud et al., 2005). XRMT is a 3D nondestructive radiographic imaging technique with a spatial resolution limited by the width of the beam, the scintillator efficiency, the number of pixels on the camera and the X-ray absorption coefficient of the rock-forming minerals.

A few experiments using XRMT have recently been published, for example, the dissolution of fractures in carbonated rocks (Gouze et al., 2003; Gouze and Luquot, 2011). Noiriel et al. (2004) investigated of porosity and permeability effects from microstructure changes during limestone dissolution. At present, most of the technological and data processing problems have been resolved and complex media can be investigated.

The X-ray linear attenuation coefficient of a sample depends on its chemical composition and on the energy of the X-ray beam, and is proportional to the rock assemblage density. The tomography apparatus installed at the ID19 beam line of the European Synchrotron Radiation Facility (ESRF, Grenoble, France) takes advantage of the homogeneous, parallel, monochromatic, and highly coherent very high photon flux produced by the synchrotron. So, the scanning of 9 mm thick cylindrical core of carbonate is tractable. The detection device is composed of a shutter controlling the exposure time, an X-ray/visible light converter. For each X-ray reading, the monochromatic X-ray beam passes through the sample and then reaches the scintillator, which converts it into visible light recorded by a high-speed digital CCD camera (2048 × 2048 pixels). With the selected optics, the pixel size is 5.06 μm. The core is fixed on a mechanical bench; all scans are perpendicular to the cylinder axis. The incident beam illuminates the entire diameter of the core in order to decrease as much as possible the diffusion effect and the resulting reconstruction artifacts. As the entire core cannot be imaged in one run, the beam is adjusted to image the part close to the fluid injection side of the core (at about 1 mm from the inlet surface). A total of 1500 X-ray readings were recorded, using an exposure time of 2 s at each angle and a rotational interval of 0.12 degree along the core axis. This results in high-quality images having a resolution of

about the size of the voxel dimension. For a given energy of incident X-ray beam (here 40 keV), the attenuation depends on the chemical composition of the rock, specifically the atomic number of its components and their mass fraction per volume (i.e. the density). Figure (4.7) shows a schematic description of X-ray microtomography techniques in which a source of X-ray crossing the sample passing through a collimator to narrow and align the beam (parallel rays), followed by Optics and CDD Camera to capture the photos of each slide of the test rock sample.

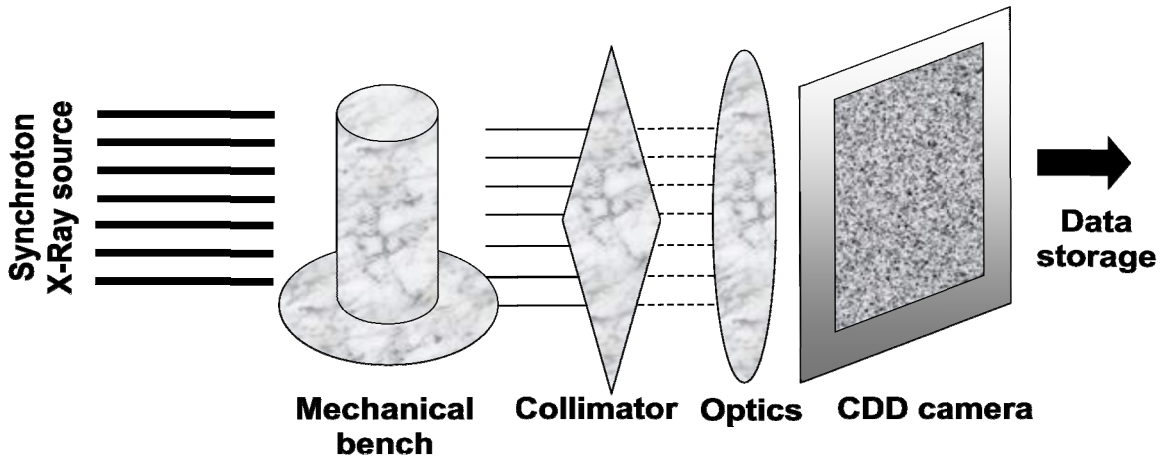

Figure 4.7: A schematic description of f the X-ray microtomography setup.

XRMT imaging was performed for some tested sample before and after percolation experiments; hereafter a description of structure properties is presented for both Mallorca and Lavoux sample before the percolation. In the results and discussions chapter we compare some of XRMT images for some of the tested sample before and after the percolation.

4.2.3.1. XRMT description of Mallorca sample

From the analysis of XRMT images, we realize that the macroporous phase is connected by microporous phase for both of MC_T1 and MC_E13 as show in Figure (4.8).

For MC10_T1, the mean diameter for both macroporous and microporous phases were estimated of 100 and 47 microns, whereas it was estimated about 65 microns for indurate bioclasts.

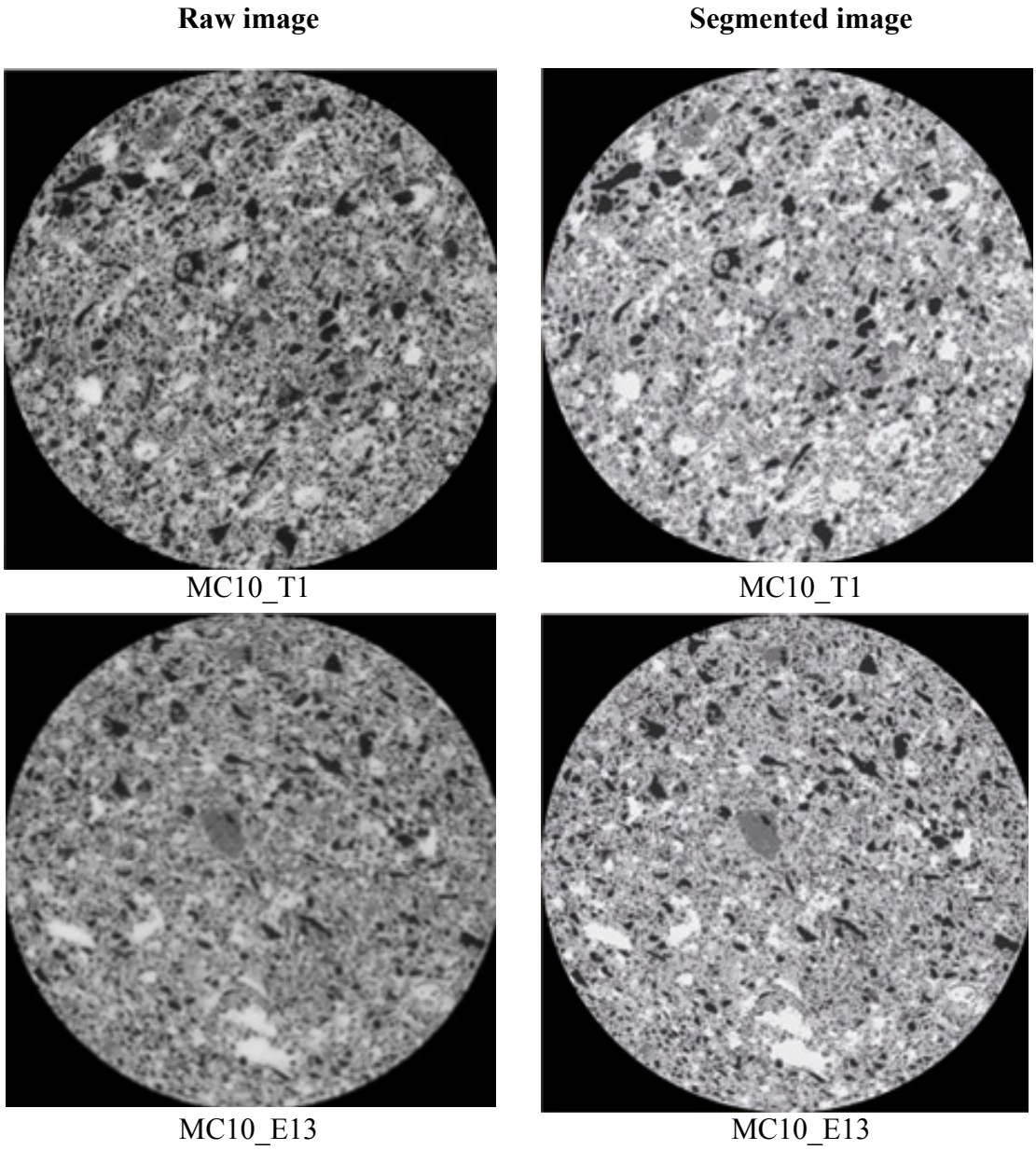

Figure 4.8: Two dimensional XRMT images of MC10_T1 sized of (1201×1201) pixels and MC10_E13 sized of (1561×1561) pixels. Images on the left are raw and on the right are segmented in 4 phases (pore phase, micropore phase, solid phase and indurate bioclasts phase) with pixel size of 5.06 µm.

For MC10_T1, the mean diameter for both macroporous and microporous phases were estimated of 93 and 39.3 microns respectively, whereas it was estimated of 88 microns for indurate bioclasts.

4.2.3.2. XRMT description of Lavoux sample

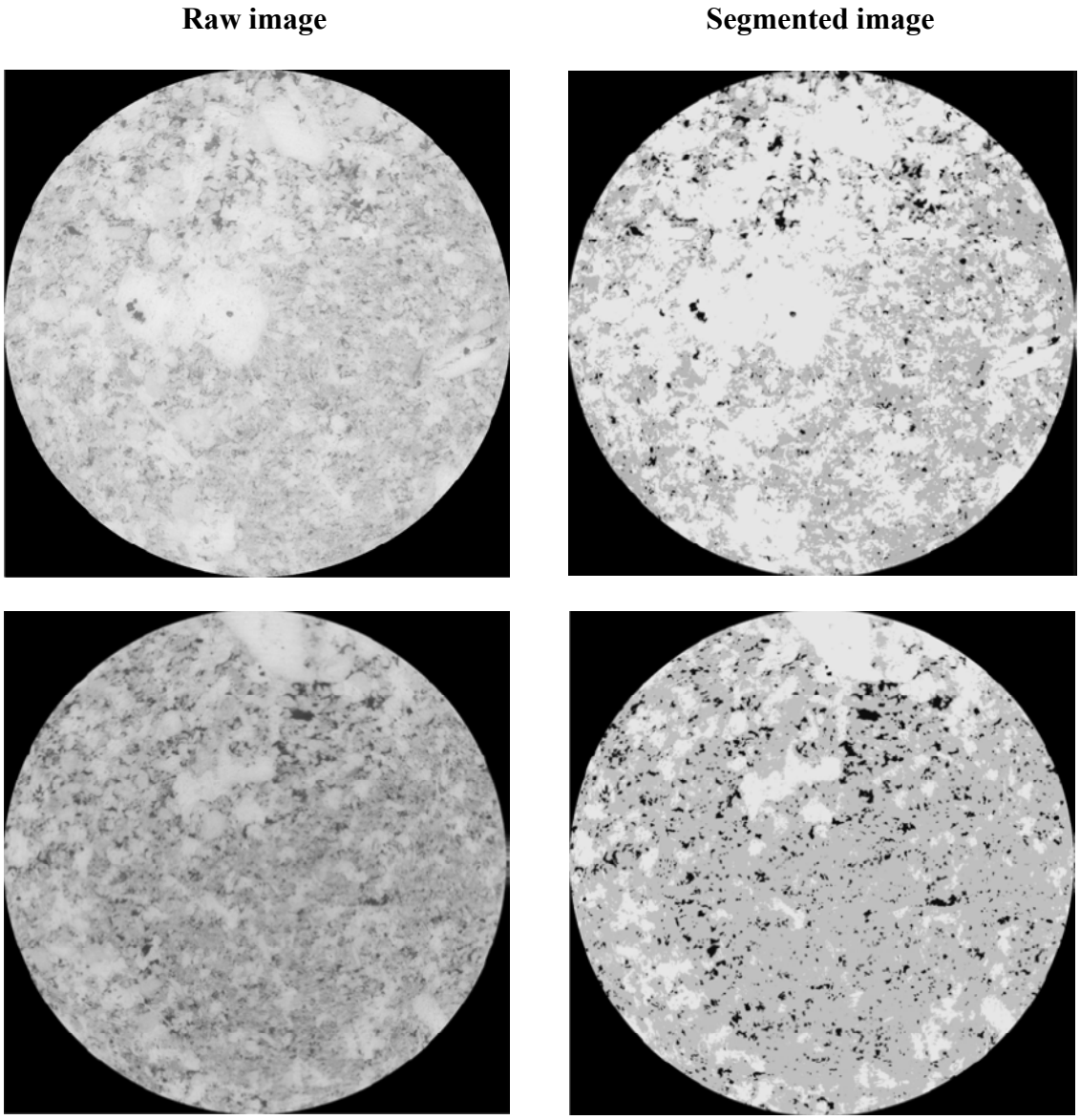

Figure 4.9: Two dimensional XRMT images of two section (1541×1541) pixels of Lavoux sample , the images on the left are raw images and on the right are segmented in three phases (pore phase, micropore phase and solid phase) with a pixel size of 5.06 µm.

From the analysis of XRMT images we realize that the macroporous phase is connected by microporous phase as show in Figure (4.9), the main pore diameter of the macroporous phase was found 25.4 microns where it was found 2.85 for the microporous phase.

4.3. The experiment protocol

4.3.1. Calcite dissolution by mixing waters

The results obtained from the PHREEQC numerical simulations (Chapter 3) demonstrated that the maximum subsaturation is expected to occur for mixing ratios of about 15%, while the expected dissolved calcite reaches its maximum for 45% of mixing.

This apparent inconsistency can be explained by the strong influence of the pH on the carbonate speciation, the relative lower activity of CO_3^{2-} compared to that of dissolved Ca^{2+}, and the dependency of the activity coefficients on the mixing ratio (i.e. with salinity variation). Therefore, the capacity of a certain mixture to dissolve calcite should be addressed in terms of calcite dissolution, rather than on the variation of calcite saturation with the mixing ratio.

In order to examine these results experimentally, two end member solutions were initially mixed together at two different mixing ratios of 15 and 45% of salty end member solution; each solution was prepared inside a well isolated reservoir in order to keep the same level of calcite saturation state and pCO_2. The chemical composition is summarized in Table (4.3).

Table 4.3: The chemical composition of injected waters at different mixing ratios of salt and fresh end member solutions.

Saltwater (%)	pH	Ca tot (mol)	C tot (mol)	Na tot (mol)	Cl tot (mol)	PCO2 Bar	Ω CaCO3	Ionic strength
0*	8.27	5.30×10^{-4}	1.05×10^{-3}	0	0	$10^{-3.5}$	1	1.58×10^{-3}
15	7.81	1.01×10^{-3}	2.04×10^{-3}	1.50×10^{-1}	1.50×10^{-1}	$10^{-2.86}$	0.35	1.53×10^{-1}
45	7.53	2.11×10^{-3}	4.34×10^{-3}	4.50×10^{-1}	4.50×10^{-1}	$10^{-2.34}$	0.53	5.06×10^{-1}
100**	7.38	3.70×10^{-3}	7.62×10^{-3}	1.00	1.00	$10^{-2.0}$	1	1.011

* and ** are the fresh and salt input end member solutions respectively.

Many testes have been done to check the experimental setup and the measuring instruments before starting the percolation experiments. Table (4.4) summarized the experiments that were carried out for both Mallorca and Lavoux samples at 15 and 45% of salty end member solution.

PHREEQC was used to calculate the actual saturation index and pCO_2 corresponding to the input concentrations of laboratory solution of Ca^{2+}, Mg^{2+}, Na^{+} and Cl^{-} and pH. PHREEQC calculates thus the concentration of Carbon that is in equilibrium with these conditions.

Table 4.4: **Summary of experiments that were carried out with 15 and 45% mixing ratios**

Experiment ID	Sample	Mixing ratio	Flow rate ($cm^3.hr^{-1}$)
MC10_E4	Mallorca[1]	15%	100
MC10_E5	Mallorca	15%	10
MC10_E7	Mallorca[1]	15%	10
MC10_E9	Mallorca[1]	45%	10
Lav_E3	Lavoux[1]	45%	10
Lav_E1	Lavoux[1,2]	45%	10

[1] Chemical analysis of outlet solution was done.
[2] X-ray micro tomography was done before and after experiment.

4.3.2. Calcite dissolution under long term injection of deionized water

Some experiments were carried out only by injection of deionized water or double deionized water to elucidate the effect of dissolution mechanisms on the permeability and the porosity of the tested samples. Long term experiments were carried out for Mallorca sample. The following Table (4.5) summarizes the initial conditions of these experiments.

Table (4.5): Summary of experiments carried out with deionized water injection.

Experiment ID	Sample	Injected water	Flow rate ($cm^3.hr^{-1}$)
MC10_E2	Mallorca[1]	deionized water	10
MC10_T1	Mallorca[1,2]	deionized water (sterilized)	10

[1] Chemical analysis of outlet solution was done.
[2] X-ray micro tomography was done before and after experiment.

4.3.3. Calcite dissolution under sequential injection of deionized water and deionized water enriched of CO_2

Some experiments were carried out to test the hydrodynamic behavior of the tested samples when injecting deionized water followed by injection of deionized water enriched with CO_2 and reiterate the injection cycle. For those sorts of experiments two tanks were used to provide deionized water and deionized water enriched with CO_2. The idea here was to test the hydraulic behavior of the tested sample when injecting less aggressive water (deionized) followed by aggressive water (deionized + CO_2), in other words, the effect of solution reactivity and Calcite dissolution mechanisms on the structure and hydro-physical properties of the tested Calcite samples.

The experimental setup was used to carry out these sorts of experiments where the CO_2 gas was added using a manual pump with a net volume of 24.8 cm^3. The pump was filled with CO_2 at 5 bars from the CO_2 cylinder bottle, and then connected to the tank through a connection tube prepared for this purpose. The pH evolution was recorded until it reached to a stable value. The corresponding pCO_2 was calculated using PHREEQC and it was $10^{-1.5}$ bars; the total mass of dissolved CO_2 was 1.099×10^{-3} $mol.kgw^{-1}$.

A summary of the experiments that were carried out for both Mallorca and Lavoux is reported in Table (4.6) , where sequential injection of deionized and deionized enriched with CO_2 were implemented.

Table 4.5: Summary of experiments that were carried out with deionized and deionized enriched of CO_2

Experiment ID	Sample	Injected water	Flow rate ($cm^3.hr^{-1}$)
Lav_MK	Mallorca[1]	Milli-Q then (Milli-Q+CO_2)	10
MC10_E13	Lavoux[1,2]	Milli-Q then (Milli-Q+CO_2)	10

[1] Chemical analysis of outlet solution was done.
[2] Scan electron microscopy SEM was performed after percolation.

4.4. Experimental setup

A laboratory flow apparatus was designed and built to examine these processes in Calcite core samples as shown in Figure (4.10). The fluid was prepared in a cylindrical tank designed for mixing and connected to a dual piston pump for fluid injection as shown in figure (4.10). The two motorized piston pumps are equipped with displacement encoders, which allow an accurate control of the flow rate. This motorized dual pump system is operated to obtain a continuous flow rate. The piston pump motion and the pneumatically-controlled valves are operated by LabView based software.

In the percolation cell, a radial confining pressures equals to the inlet pressure is applied to the sample to avoid deviatory stresses that may damage the sample irreversibly. The radial confining pressure is obtained by pressurization of the silicon jacket covering the sample.

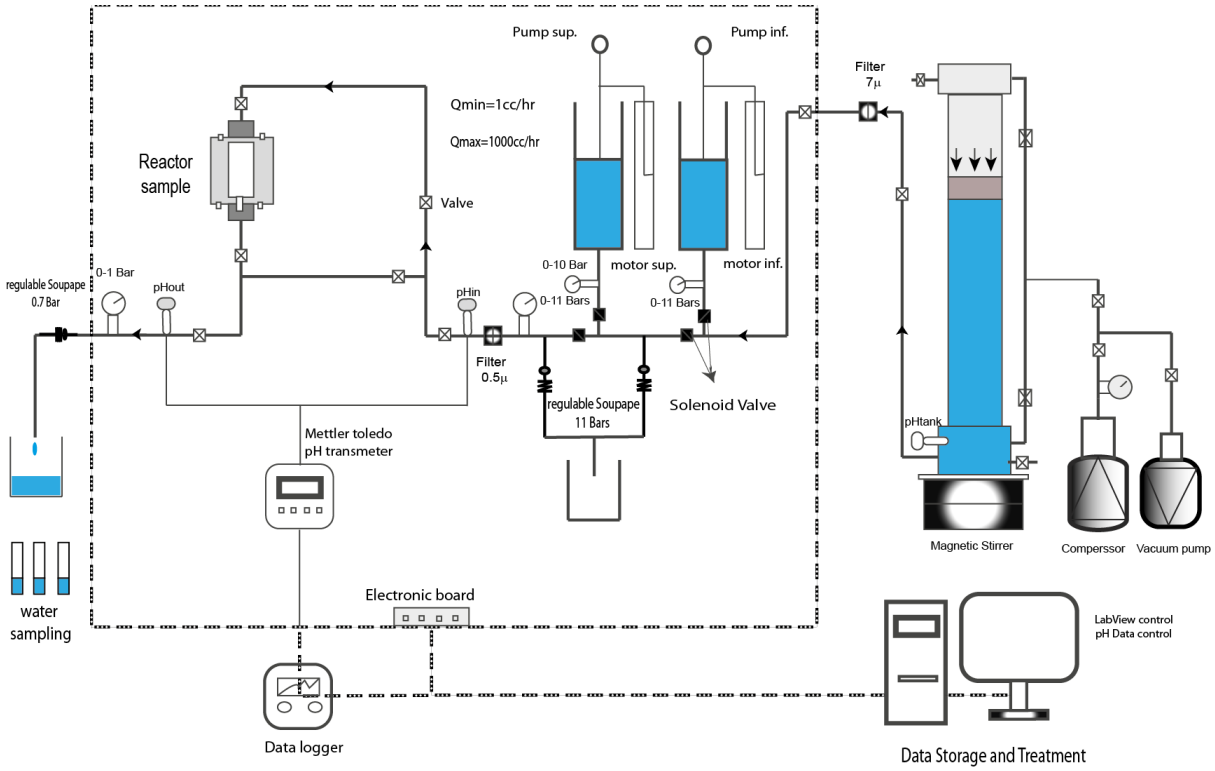

Figure 4.10: Schematic representation of DIAPOR setup.

Data acquisition and storage, setting of regulation parameters and automation of the piston pump motion and the pneumatically-controlled valves were performed via LabView software. Pressure is measured at the inlet in the range [0 ± 0.0005; 10 ± 0.0005] bars using KELLER digital pressure sensor PR-33X. The pressure at the outlet is measured in the range [0 ± 0.0005; 1 ± 0.0005] bars using SCAIME digital pressure sensor followed by a back-pressure controller of maximum 0.7 bars to avoid degassing during the experiment.

The pH and temperature of the inlet and outlet fluid was measured with a pH sensor InPro 4800i/SG/120 (METTLER TOLEDO) to detect the pH variation during the percolation see Figure (4.10). The pH sensors are connected with ALMEMO® 3290 data logger device and acquisition and storage was performed via data control software package as shown in Figure (4.11). The interface of LABVIEW and data control based software is shown in Figure (4.14).

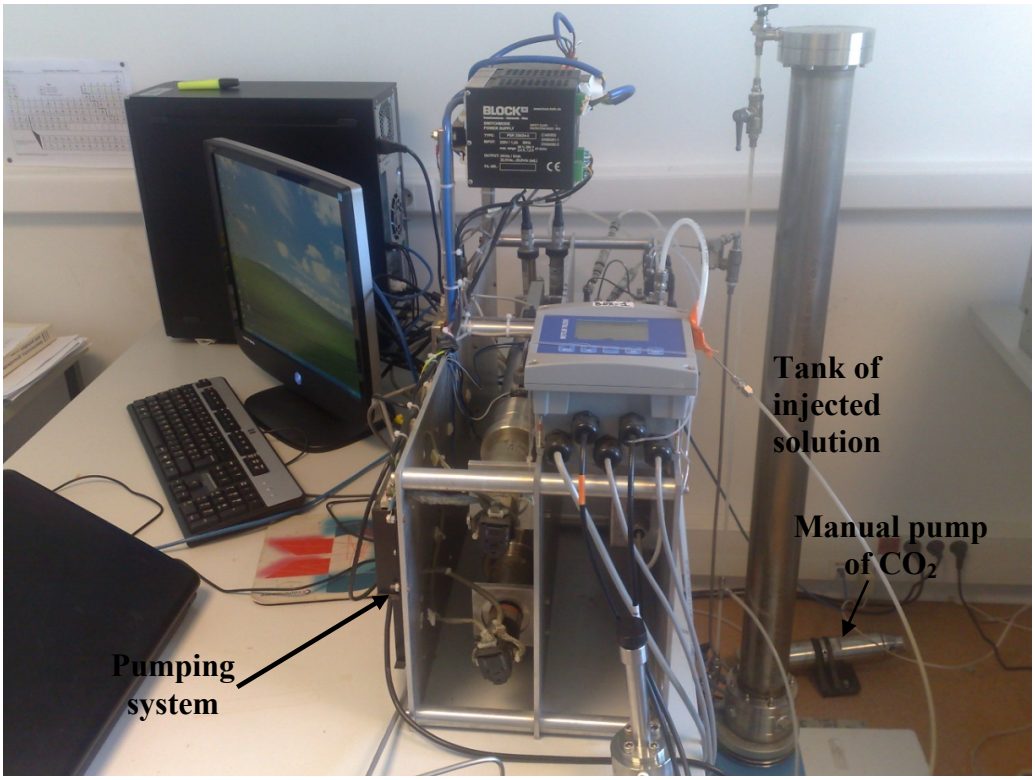

Figure 4.11: photograph represents the experimental branch.

Limestone cylindrical cores dimensioned of 9 mm diameter and 18 mm length were prepared to suit the experimental procedure. A sample volume was considered as a representative elementary volume (REV) of rock and contains thousands of pores while heterogeneities

larger than the sample size are clearly not included in this REV, the experimental results can be easily upscaled to the reservoir scale in terms of matrix properties. The core was fixed with silicon glue in a Teflon® sleeve to seal the core periphery as shown in Figures (4.12) and (4.13).

4.4.1. Permeability measurements

The permeability and the porosity of the tested samples were measured before starting the percolation experiments. To initialize the experiment, the core was saturated under vacuum with calcite-equilibrated water. A constant flow rate was applied to measure the initial permeability. At elapsed time t = 0, the prepared solution were injected at constant flow rate in the sample installed in the percolation cell with a confining pressure equal to the pressure at the sample inlet. The experiments were conducted at room temperature.

In order to deduce the initial sample permeability, equilibrated solution with respect to the sample mineral was prepared to avoid any interaction with the sample. A range of flow rates from 10 to 100 $cm^3 \cdot h^{-1}$ were applied and the pressure gradient corresponding to each flow rate was registered at the output files of LABVIEW software. Then the data was treated and refined by correcting the flow rate of each pump.

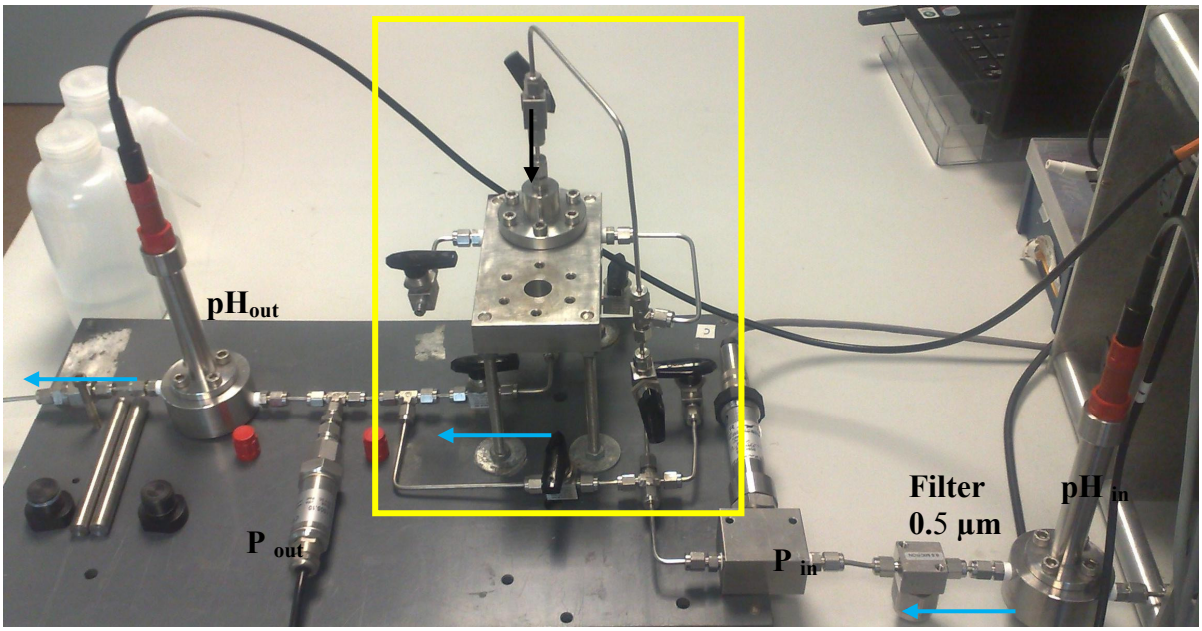

Figure 4.12: photograph represents the flow cell, pressure sensors and pH meters.

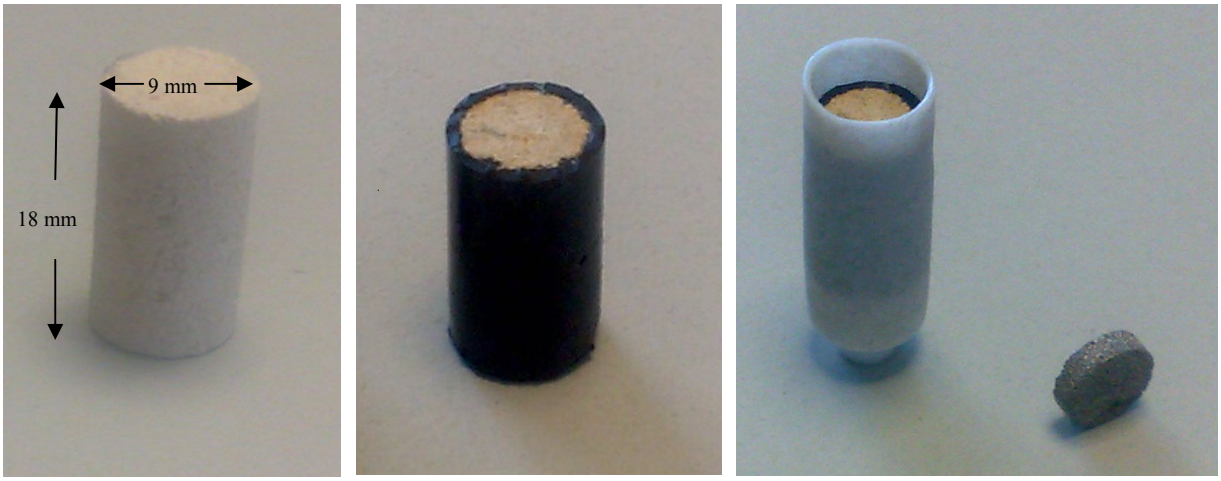

(a) (b) (c)

Figure 4.13: Sample preparation stages a) cored sample, b) in silicon glue, c) in Teflon sleeve.

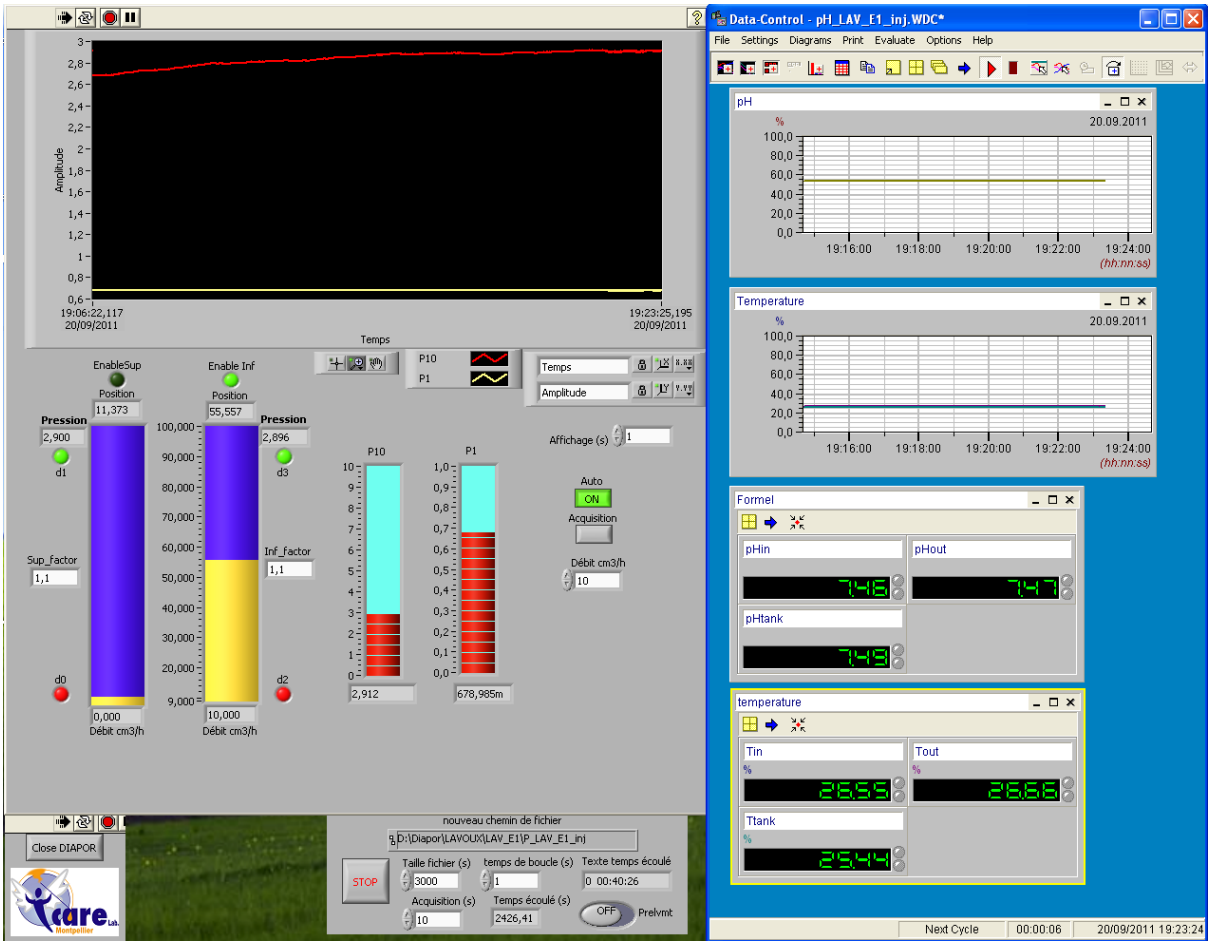

Figure 4.14: User interface of LABVIEW and data control software that allow following the evolution of ΔP and pH at the inlet and outlet of the sample.

Time-resolved sample permeability $k(t)$ is directly deduced from monitoring the pressure difference $\Delta P(t)$ (Pa) between the reactor inlet and outlet using Darcy's Law, where the ratio of volumetric flow rate Q ($m^3 \cdot s^{-1}$) over the pressure difference ΔP is directly related to the permeability of the sample k (m^2) by:

$$k = -\frac{\mu L}{S}\frac{Q}{\Delta P} \tag{4.1}$$

Where, L is the length of the sample in the flow direction (m), S is the section of the sample (m^2) and μ is the dynamic viscosity of the fluid (Pa·s). Permeability values are reported in mD, ($1mD \approx 0.987\ 10^{-15}\ m^2$).

These experiments were carried out at room temperature which was variable. Some of these experiments were carried out using saline solution. Therefore, the time resolved permeability values were corrected with temperature and salinity of the injected water. Variation of viscosity as a function of temperature and salinity is illustrated in Figure (4.14).

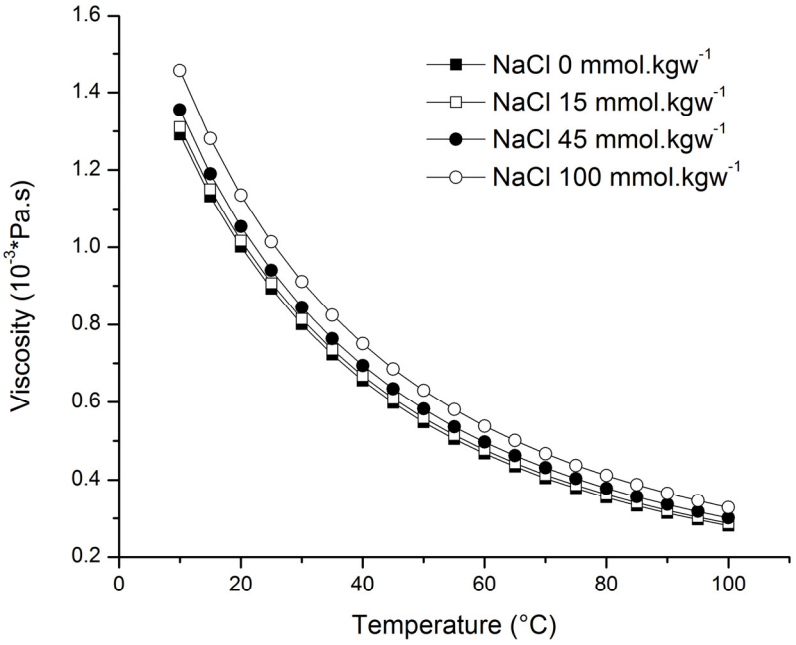

Figure 4.15: Viscosity variation as a function of temperature and salinity.

The correlation of dynamic viscosity (El-Dessouky and Ettouny, 2002) of the injected solution is given by:

$$\mu = (\mu_W) * (\mu_R) * 10^{-3} \quad (4.2)$$

$$\ln(\mu_W) = -3.79418 + 604.129/(139.18 + \mathrm{T}) \quad (4.3.a)$$

$$\mu_R = 1 + \mathrm{A} \times \mathrm{S} + \mathrm{B} \times \mathrm{S}^2$$

where:

$$\mathrm{A} = 1.474 \times 10^{-3} - 1.5 \times 10^{-5}\mathrm{T} - 3.927 \times 10^{-8}\mathrm{T}^2 \quad (4.3.b)$$

$$\mathrm{B} = 1.0734 \times 10^{-5} - 8.5 \times 10^{-8}\mathrm{T} - 2.23 \times 10^{-10}\mathrm{T}^2$$

where: μ in $kg.m^{-1}s^{-1}$, T in °C and S in $gm.kg^{-1}$. The above correlation is valid over the following range: $0 \leq S \leq 130$ gm/kg and $10 \leq T \leq 180$ °C.

Results indicated that the initial permeability of Mallorca samples showed high level of heterogeneity ranged from 20 to 100 mDarcy, whereas the Lavoux samples permeability ranged from 4 to 12 mDarcy.

In the percolation experiments the same procedure was applied except the injected solution which was varied according to each experimental conditions, hereafter explained.

4.4.2. Porosity measurements:

The bulk connected porosity of the limestone sample was measured by the triple-weight method. Three specimens from a representative sample of each rock were machined to conform closely to the geometry. The dry weight of each specimen was measured, and then the specimens were vacuumed and saturated with water. The saturated mass, as well as the immersed mass, were measured.. The porosity of each specimen was calculated using the flowing equation:

$$Porosity\ (\emptyset) = \frac{Saturated\ mass - Dry\ mass}{Saturated\ mass - immersed\ mass} \times 100\% \quad (4.4)$$

The results of the porosity calculations using the triple method are summarized in Tables (4.6) and (4.7). The the average Mallorca samples porosity is 41.65% with standard deviation of 1.5, whereas the average Lavoux samples porosity is 25.12% with standard deviation of 0.5.

Table 4.6: Porosity measurements of Mallorca Samples using the triple method.

Sample	Dry mass (g)	Immersed mass (g)	Saturated mass (g)	Porosity (%)
MC10_94m_P1	2.705	1.673	3.446	41.79
MC10_94m_P2	2.933	1.831	3.75	42.57
MC10_94m_P3	3.084	1.926	3.84	39.50
MC10_94m_P4	2.938	1.842	3.757	42.77

Table 4.7: **Porosity measurements of Lavoux Samples using the triple method.**

Sample	Dry mass (g)	Immersed mass (g)	Saturated mass (g)	Porosity (%)
Lavoux_A	2.044	1.287	2.305	25.63
Lavoux_B	3.61	2.274	4.047	24.64
Lavoux_C	3.732	2.349	4.195	25.08

4.4.3. Dissolved Calcite measurements and temporal variation of porosity

Porosity estimation of tested samples was done using the chemical analyses of the outlet solution to detect porosity variation during percolation experiments. Moreover, the macro and micro porosity were estimated from the X-ray computed microtomography image analyses before and after the experiments to elucidate the trend of macro and micro porosity evolution throughout the sample.

Fluid samples were collected at the outlet for the chemical analysis of cation and anion concentrations, using electrophoresis and inductively coupled plasma-atomic emission spectrophotometer (ICP-AES) to deduce the chemical composition evolution with time of percolation. The concentrations of Ca^{2+}, Mg^{2+}, Na^{+}, Cl^{-} are reported in ($mmol.kgw^{-1}$).

The total dissolved mass of Calcite (g) was calculated from the difference between the outlet and inlet Calcium concentration in (mol.l^{-1}), the molar mass of Calcite $M_{m,CaCO_3}$ (g.mol^{-1}) and the injection flow rate Q (l.hr^{-1}) as follow:

$$mCaCO_3 = M_{m,CaCO_3} \times Q \times \int_{t=to}^{t} \Delta C_{Ca} \, . \, dt \tag{4.5}$$

The temporal variation of porosity is deduced from the dissolved Calcite based on:

$$\emptyset_t = \emptyset_0 + \frac{V_{m,CaCO3}}{V_{core}} \times Q \times \int_{t=to}^{t} \Delta C_{Ca} \, . \, dt \tag{4.6}$$

where $\emptyset_t$ denotes the total core porosity at time *t*, $\emptyset_0$ stands for the initial core porosity, t_0 represents the time at the start of the experiment, $V_{m,Ca}$ refers to the molar volume of Calcite (3.7×10^{-5} m^3.mol^{-1}), and V_{core} designates the total core volume (1.145×10^{-6} m^3). Equation (4.5) can be used to determine the porosity of a dissolving core by numerically integrating this equation yielding:

$$\emptyset_t = \emptyset_0 + \frac{V_{m,CaCO3}}{V_{core}} \times Q \times \sum_{i} \Delta C_{Ca,i} \Delta t_i \tag{4.7}$$

where $\Delta C_{CaCO3,i}$ stands for the i^{th} experimentally measured value of $\Delta C_{Ca,i}$ and Δt_i represents the elapsed time between the i^{th} and the $(i - 1)^{th}$ outlet solution sampling.

Chapter 5

Results and Discussions

5. Results and Discussions

5.1. Mixing percolation experiments

Percolation mixing experiments were carried out for both Mallorca and Lavoux samples by injecting mixture of the two end member solutions mentioned in Table (3.3) in the Material and method chapter at 15 and 45 % of the salty end member solution.

Here after a summary of experimental conditions at both mixing ratios 15 and 45% for Mallorca and Lavoux samples is reported in Table (5.1). The chemical analysis of the out let solution was performed for some experiments.

Table 5.1: Summary of mixing percolation experiments

Experiment ID	Mixing ratio (%)	Flow rate ($cm^3.hr^{-1}$)	K_{ini} (mDarcy)	K_{fin} (mDarcy)	Duration (hours)	Dissolved Calcite (mg)
MC10_E4	15	100	21.3	9.92	40	28.5
MC10_E5	15	10	92	10	145	-
MC10_E7	15	10	22.2	18	41	12.5
MC10_E9	45	10	45	6.2	122	-7.23*
Lav_E3	45	10	4	1.58	106	-3.55*
Lav_E1	45	10	3.8	2.7	664	11.54

* refers to precipitation of Calcite.

Hereafter, the experiments are described, and the results of time resolved permeability as well as the evolution of the pH at the outlet are plotted. The chemical analysis of the outlet solution and the relation between the permeability and the temporal variation of porosity are mentioned. Some experiments are mentioned in this section to elucidate the evolution of permeability and the pH at the outlet but the chemical analysis of the outlet water was not performed.

5.1.1. Percolation experiment at 15% mixing ratio

5.1.1.1. MC10_E4 (Mallorca)

The system was cleaned and vacuumed then the initial permeability measurements of the tested sample were done before starting the percolation experiment MC10_E4.

Equilibrated water with respect to Calcite was prepared for the initial permeability measurements to minimize any chemical reaction effect on the measurements. Three different flow rates of 50, 75 and 100 $cm^3.hr^{-1}$ were applied for injection into the sample and the corresponding time resolved permeability was calculated using Darcy Law. The permeability values were found 21.4, 21.5, 21.02 mDarcy at each flow rate respectively. Figure (5.1) illustrates the calculated permeability at three different flow rates showing that the average initial permeability of the sample is about 21.3 mDarcy.

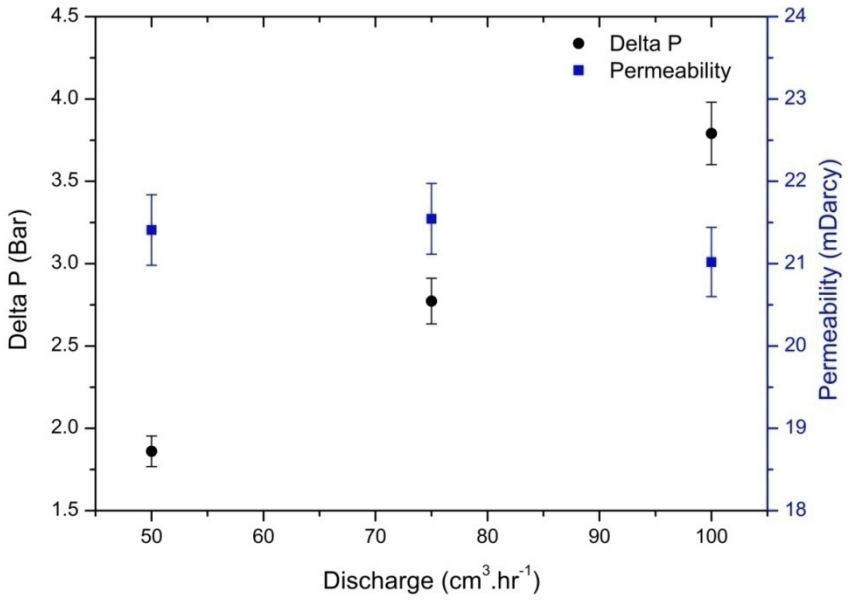

Figure 5.1: The initial permeability of the tested sample.

On the other hand the initial porosity of sister samples was measured using the triple method and was found around 41.6%.

The mixing was done by adding the $CaCl_2$ and $NaHCO_3$ salts corresponding to the chemical composition of the 15% of mixing ratio inside the tank then the tank was vacuumed and was filled with 5 liters of diluted NaCl in deionized water. The mixture was stirred using a

magnetic stirrer and the pH evolution of the solution were monitored by the pH sensor installed at the tank. A sample of injected water was analyzed and compared to the prepared one at the laboratory as shown in Table (5.2).

The percolation experiment started when the pH of the solution reached a stable value (nearly 7.3) which is lower than the pH obtained from PHREEQC calculation.

The flow rate was fixed at 100 ($cm^3.hr^{-1}$). The outlet water was sampled for the chemical analyses from time to time to measure the concentration of Ca^{2+}, Mg^{2+}, Na^+ and Cl^- at the outlet.

Table 5.2: The chemical characteristics of injected solution from both theoretical calculation (PHREEQC) and prepared laboratory solution.

Solution	pH	Ca tot ($mol.l^{-1}$)	Na tot ($mol.l^{-1}$)	Cl tot ($mol.l^{-1}$)	Ω ($CaCO_3$)	pCO_2
PHREEQC	7.81	1.01×10^{-3}	1.50×10^{-1}	1.50×10^{-1}	0.35	$10^{-2.86}$
Laboratory	7.29	1.074×10^{-3}	1.44×10^{-1}	6.05×10^{-1}	0.125	$10^{-2.3}$

The experiment was stopped when the concentration of the Calcium at the outlet reached a stable value. The time resolved permeability was calculated based on Darcy law and the effect of temperature and salinity on the viscosity of the injected water was taken into account by correcting the permeability values using El-Dessouky and Ettouny (2002) equation.

The resolved time permeability evolution and the evolution of the pH after the sample are shown in Figure (5.2).

Regarding to the permeability evolution with time, one can notice that the instantaneous permeability measured of the tested sample decreased in two stages: sharply sharp decrease during the first 5 hours followed by a smoother decrease until the end of the injection where it reached 42% of its initial value as show in Figure (5.2).

The pH evolution at the outlet showed an instantaneous increase from 7.3 to 7.6, followed by a stable value of 7.7.

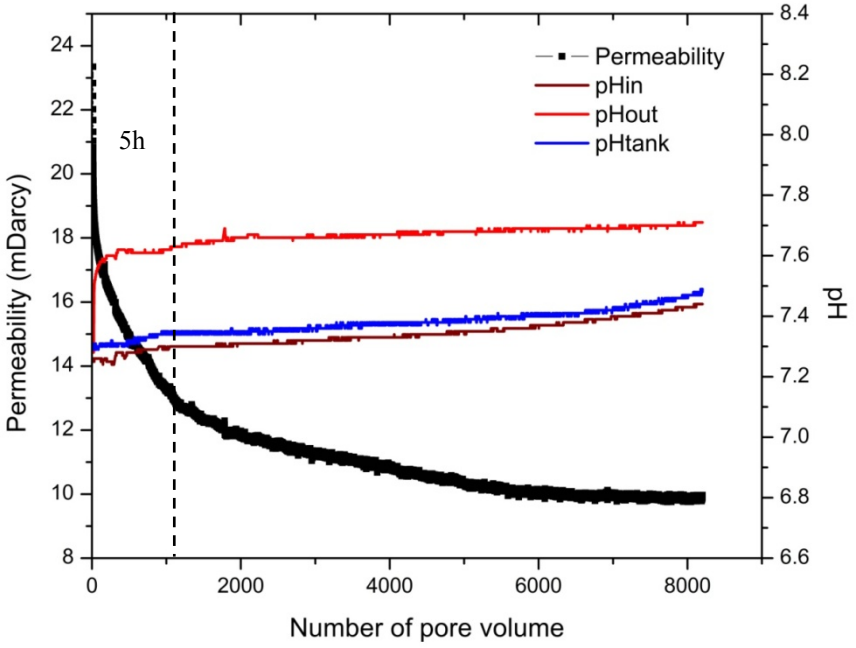

Figure 5.2: Time resolved permeability and pH (in the tank and at the sample inlet and outlet) as a function of the number of pore volume.

The rapid increase of the pH of the outlet solution at the beginning of the experiment reflects the interaction between the injected solution and the rock sample and dissolution reaction was started. Later, a stable value of pH reflects that the reaction has reached a constant level. This was in agreement with chemical analysis of the outlet solution.

The permeability decreased rapidly in the first stage might be due to the migration of detached particles due to dissolution toward the outlet of the sample. The detached particles are then redistributed inside the pore network. Some of these particles are transported towards the outlet of the core while others are trapped inside, yielding thus to pore clogging and consequently permeability reduction.

Regarding to the chemical analysis of the outlet solution in Table (5.3) and the laboratory solution in Table (5.2), one can see that both of Ca^{2+} and Mg^{2+} concentration have increased.

As shown as in Figure (5.3), during the first hour of injection, ΔCa^{2+} reached a maximum value of 0.08 ($mmol.kgw^{-1}$) then it decreased linearly until reaching a minimum value of 0.05 ($mmol.kgw^{-1}$) at the 4^{th} hour of injection. From the 5^{th} hour until the end of injection it

became stable. The fluctuation appears in the ΔCa^{2+} could be due to the change of reactive surface area of the tested sample. PHREEQC was used to calculate ΔCa^{2+} at equilibrium (0.15 mmol.kgw^{-1} and pH of 8.069) which indicates that the outlet solution was always undersaturated with respect to Calcite.

Table 5.3: The chemical analysis of the outlet solution.

ID	Injection time (hour)	Ca^{2+} (mmol. kgw^{-1})	Mg^{2+} (mmol. kgw^{-1})	Na^{+} (mmol. kgw^{-1})	Cl^{-} (mmol. kgw^{-1})
E4-1	0.128	1.171	-	144.12	60.50
E4-2	0.461	1.176	0.022	144.93	75.71
E4-3	0.794	1.168	-	145.93	35.06
E4-4	1.378	1.157	0.022	142.97	49.33
E4-5	2.211	1.159	-	144.40	48.09
E4-7	4.045	1.158	-	148.09	39.71
E4-8	16.462	1.167	0.010	146.84	77.57
E4-12	20.762	1.160	-	150.38	35.37
E4-15	26.462	1.167	0.010	147.75	102.39

(-) not analyzed

On the other hand the injected water contained a very low concentration of Mg^{2+} coming from the equilibrated water that was used in the initial permeability measurements and the outlet concentration of Mg^{2+} is lower than the inlet because Mg^{2+} precipitated inside the sample. The total dissolved Calcite was found about 28.5 mg at the end of the whole experiment. It was calculated by integration of the curve in Figure (5.3) and applying mass balance. The concentration of Na^{+} at the out let solution as shown in Figure 5.4 fluctuated during the beginning of injection before getting stabilized at a value close to the inlet concentration. This trend is conceptual because the sample contained NaCl in origin.

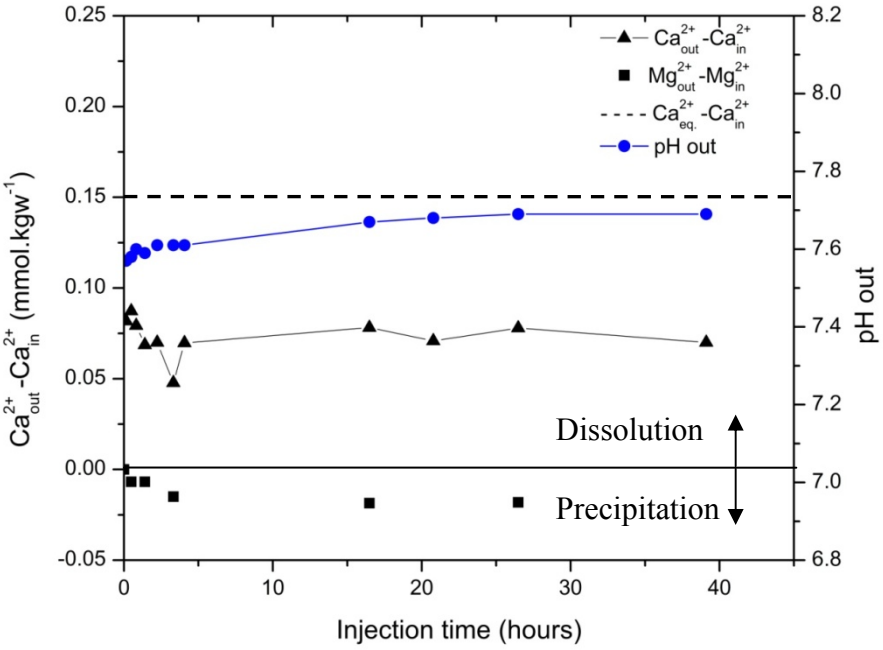

Figure 5.3: Evolution of ΔCa^{2+} and ΔMg^{2+} concentration between the outlet solution and the inlet solution, ΔCa^{2+} at equilibrium, and pH of the outlet solution.

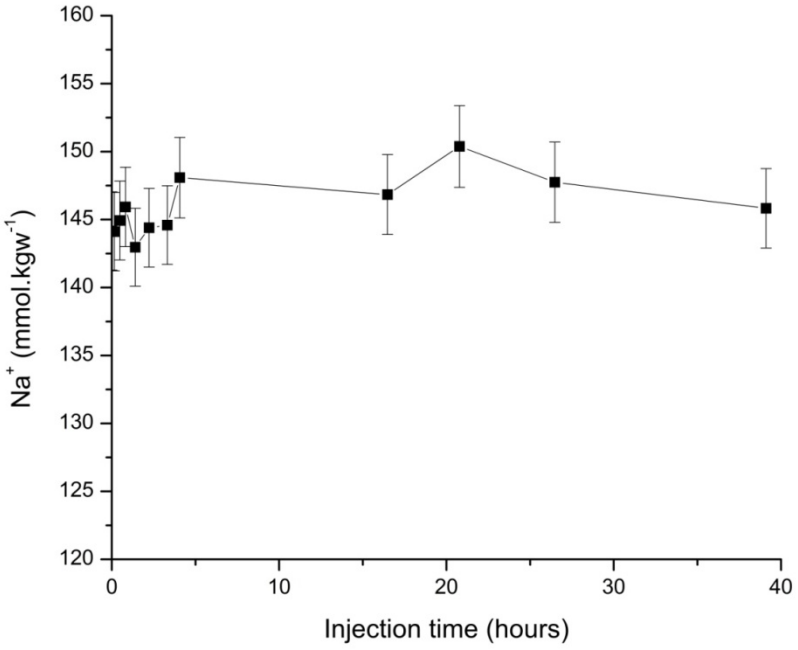

Figure 5.4: Evolution of Na^+ concentration at the outlet.

In fact the normalized porosity change (ϕ/ϕ_0) deduced from the dissolved Calcite was very little, in Figure (5.5) the normalized permeability (k/k_0) dropped at beginning of injection while the porosity change due to dissolution in very little. This suggests that there is some other phenomenon cause the permeability reduction which could be a detachment and transport of small (micro) particles that might cause clogging of the connected pores. The migration of micro particles would thus cause a rearrangement of the sample structure (solid matrix and pore network).

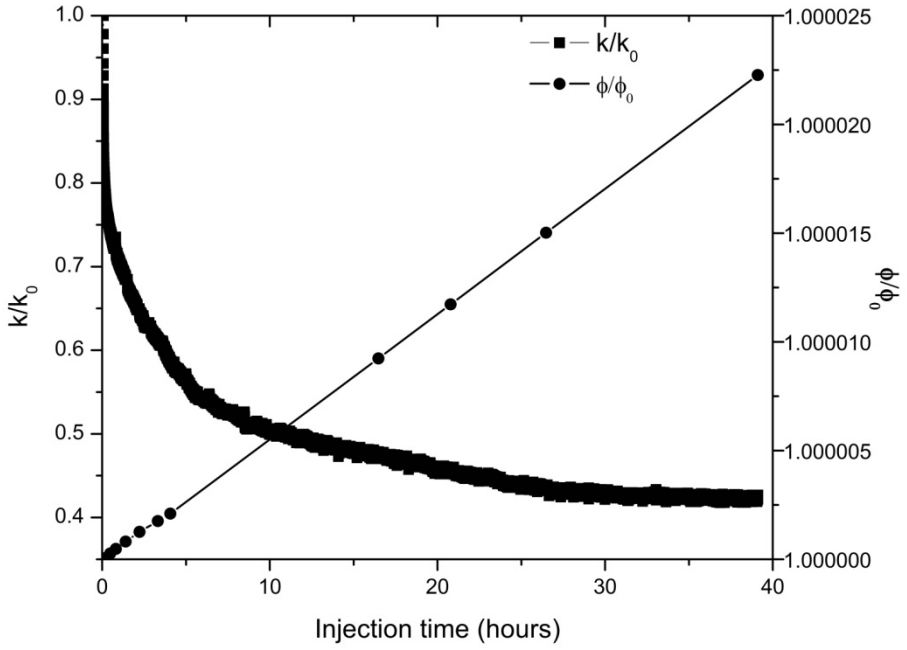

Figure 5.5: Evolution of normalized permeability and porosity corresponding to the sampling time of outlet water.

5.1.1.2. MC10_E5 (Mallorca)

The experimental branch was cleaned and the rock sample was vacuumed then the mixed solution was injected through the sample. The initial permeability of the tested sample was taken from the data file when the steady state flow was reached. It was around 93 mDarcy.

The injected solution contained 15% of salty end member solution and was prepared in the same way as in the previous experiment (**MC10_E4**) and the injection was started when both of pH at the inlet and outlet were read the same value at a flow rate of 10 $cm^3.hr^{-1}$.

Both data series of permeability and pH at the outlet were smoothed using Savitzky and Golay (1996). This method is actually performing a local polynomial regression. It is best suited to remove noise without affecting the overall signal shape.

The time-resolved permeability shows a similar behavior as the **MC10_E4** experiment. A rapid decrease in permeability at the beginning of injection was observed and then followed by a steady state behavior. After 40 hours, the injection was stopped for 12 hours, and then resumed until the end of the percolation experiment. The evolution of permeability after the break period relatively increased then it decreased again reaching a value equal to the permeability before the break period as mentioned in Figure (5.6).

The pH of the injected solution was 7.38 which is quite the same as in experiment MC10_E4. The comparison of both MC10_E4 and MC10_E5 experiments, taking into account the difference of flow rate, shows that the permeability in both experiments was sharply decreased at the beginning of injection: about 25 hours in **MC10_E5** and 5 hours in **MC10_E4**. The pH of the outlet solution showed a fluctuated trend around a value 7.5 as show in Figure (5.6). These fluctuations in pH were corresponding to the fluctuation in permeability values calculated at the time of percolation. The pressure sensor at the sample outlet was the source of these fluctuations due to migration of micro particles inside the sample that instantaneously block the sample and cause high pressure difference between the inlet and the outlet followed by pressure drop due to evasion of some of these particles.

The chemical analysis of the out let solution wasn't performed for this experiment but we can observe from the pH evolution that the dissolution is similar to the previous experiment MC10_E4. We can deduce also that the outlet solution was undersaturated with respect to Calcite.

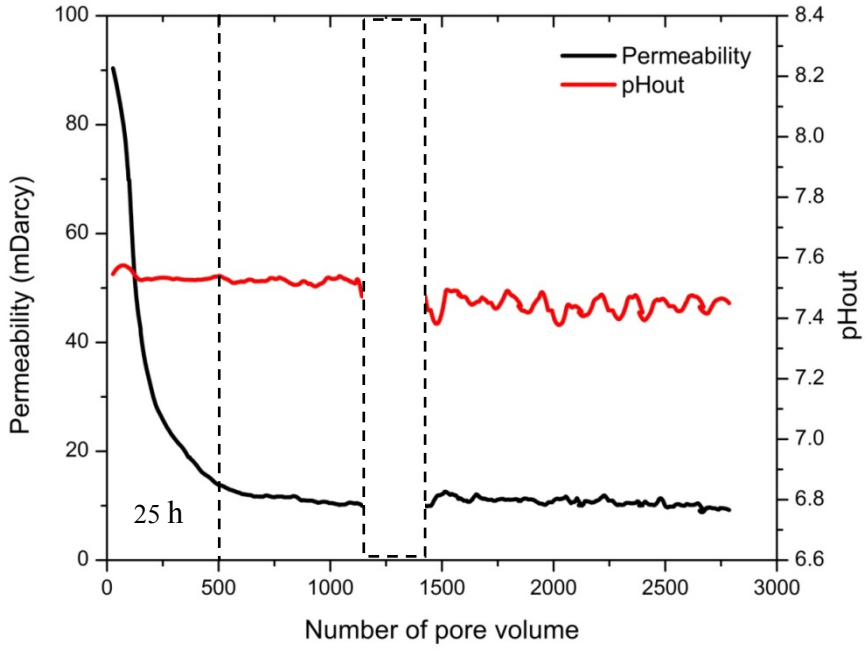

Figure 5.6: Time resolved permeability and pH at the sample outlet as a function of number of pore volume.

5.1.1.3. MC10_E7 (Mallorca)

Similarly to the **MC10_E4** experiment, the permeability was measured first with Calcite equilibrated water before starting the percolation experiment. The permeability at different flow and was calculated using Darcy law and it was found 22.65 mDarcy that was considered as an initial permeability. Then the percolation experiment was carried out by injecting a mixture of 15% salty end member solution.

The mixing was done by adding the $CaCl_2$ and $NaHCO_3$ salts inside the tank then the tank was vacuumed and was filled with 5 liters of diluted NaCl in deionized water.

An initial water sample was taken from the tank and analyzed to compare it with theoretical solution calculated using PHREEQC.

The saturation state and the partial pressure of the prepared solution at the laboratory was calculated in PHREEQC using the concentration of different species obtained from the chemical analysis of the injected solution as mentioned in Table (5.4).

Table 5.4: The chemical characteristics of injected solution from theoretical calculation (PHREEQC) and prepared solution at the laboratory.

Solution	pH	Ca tot ($mol.l^{-1}$)	Na tot ($mol.l^{-1}$)	Cl tot ($mol.l^{-1}$)	Ω ($CaCO_3$)	pCO_2
PHREEQC	7.81	1.01×10^{-3}	1.50×10^{-1}	1.50×10^{-1}	0.35	$10^{-2.86}$
Laboratory	6.79	1.0057×10^{-3}	1.320×10^{-1}	1.166×10^{-1}	0.045	$10^{-1.8}$

In general the time- resolved permeability decreased at the beginning of injection with some fluctuations then it showed a stable trend, and finished with a relative increase at the end of the experiment.

The injected solution in this experiment was more reactive (pH = 6.79) in comparison with the previous experiments (pH = 7.38). Consequently, when the solution entered to the sample with a quite acid pH of 6.85, the dissolution might have occurred at the cement layer between the Calcite grains yielding to their detachment. The detachment and the mobilization of Calcite grains will cause a rearrangement of the sample structure. A possible consequence of such rearrangement is the clogging of pores by detached Calcite grains which would cause permeability reduction (Figure 5.7).

The rapid permeability decrease is followed by a quite stable trend that might reflect an equilibrium state between two processes operating at different time scales: (i) a rapid process consisting of the detachment of Calcite grains (micro particle size) which on the short term leads to pore clogging (permeability decrease), and (ii) a slow process consisting of the chemical dissolution of Calcite which occurs on the long term leads to a higher porosity (permeability increase).

The reduction in permeability at the beginning of the percolation was not significant as it was in the previous experiments **MC10_E4** and **MC10_E5** because of the relative high reactivity of the injected solution in **MC10_E7** experiment.

Regarding to the pH at outlet, we see that it increased from 6.79 (inlet) to 7.6 (outlet). In general, the evolution of pH was in agreement with the chemical analysis of the outlet water as shown in Figure (5.7).

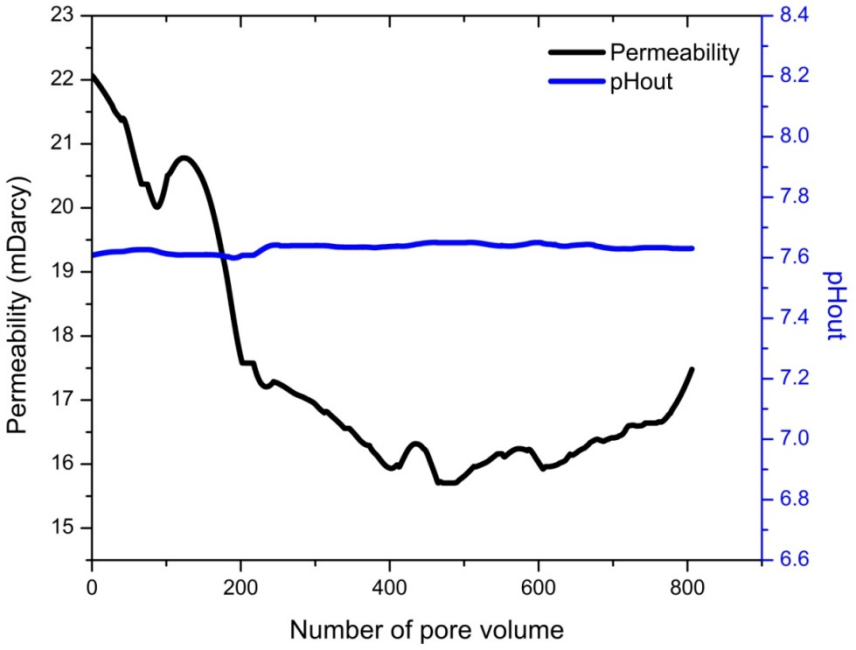

Figure 5.7: Time resolved permeability and pH at the sample outlet as a function of number of pore volume.

Concerning the chemical analyses of the injected and the outlet solution (Figure 5.8, and Figure 5.9), one can observe that the concentration difference ΔCa^{2+} between the inlet and the outlet is constant with time which indicates that the reaction rate is constant, on the other hand dissolved Mg^{2+} was observed at the first 6 hours then it seems to be precipitated in the sample matrix and the pH evolution showed a similar trend to the dissolved Ca^{2}.

PHREEQC was used to calculate ΔCa^{2+} at equilibrium (0.48 $mmol.kgw^{-1}$) which indicates that the outlet solution was always undersaturated with respect to Calcite.

The total dissolved Calcite at the end of experiment **MC10_E7** was calculated from mass balance and it was found about 12.5 mg of Calcite.

The outlet concentration of Na^{+} is higher than the inlet one. That increase in Na^{+} concentration indicates the presence of NaCl in the original sample before percolation which was leached by the injected solution as shown in figure (5.9).

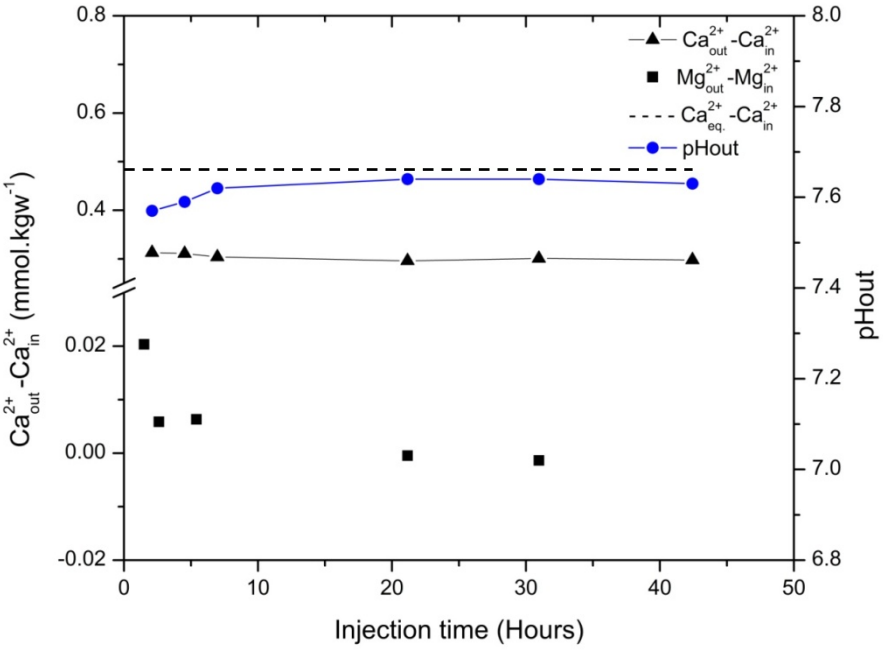

Figure 5.8: Evolution of ΔCa^{2+} and ΔMg^{2+} concentration between the outlet solution and the inlet solution, ΔCa^{2+} at equilibrium, and pH of the outlet solution.

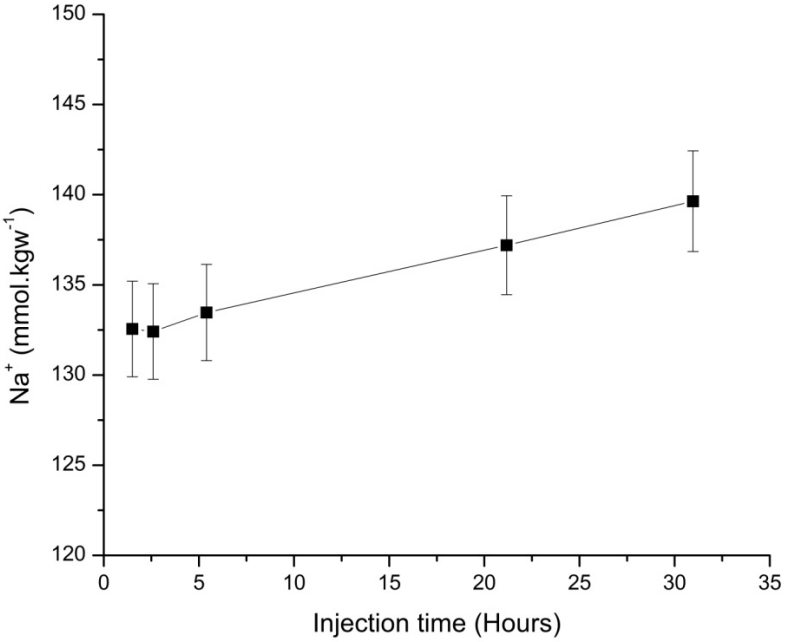

Figure 5.9: Evolution of Na^+ concentration at the outlet.

The relation between time normalized permeability and normalized porosity as a function of time shows that the porosity increased due to dissolution of Calcite where the permeability at the end of percolation showed a slight increase as shown in figure (5.10).

Dissolution of Calcite was observed at the outlet solution for all the percolation experiments which increase the porosity of the tested samples. The dissolution occurred far from equilibrium.

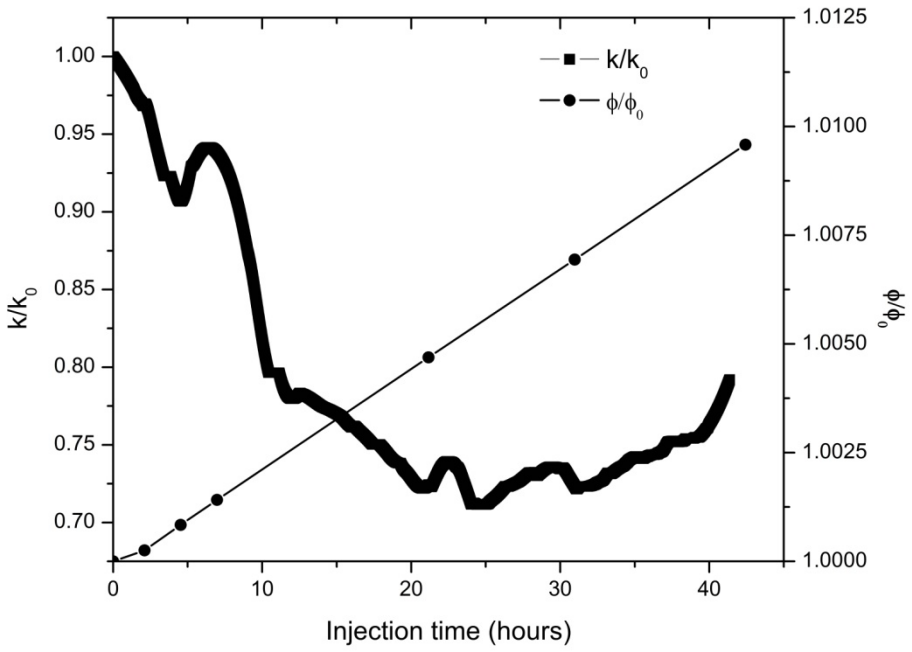

Figure 5.10: Evolution of normalized permeability and porosity corresponding to the sampling time of outlet water.

A comparison among the percolation experiments carried out at 15% of salty water in terms of normalized permeability showed a general behavior of permeability reduction especially at the beginning of injection as shown in Figure (5.11).

At a flow rate of 10 ($cm^3.hr^{-1}$), Peclet number for Mallorca samples is about 0.1 which reflects that the transport is dominated by the dispersion process. At a flow rate of 100 ($cm^3.hr^{-1}$) Peclet number for Mallorca samples is about 1 which reflects that both transport is controlled by both of advection and dispersion processes (see section 2.4.4).

On the other hand at a flow rate of 10 ($cm^3.hr^{-1}$) the permeability reductions at the beginning of injection was faster for the sample MC10_E5 than for MC10_E7 that due to the relative

high reactivity of the injected solution in MC10_E7 with a pH of 6.8 than in MC10_E5 with a pH of 7.38.

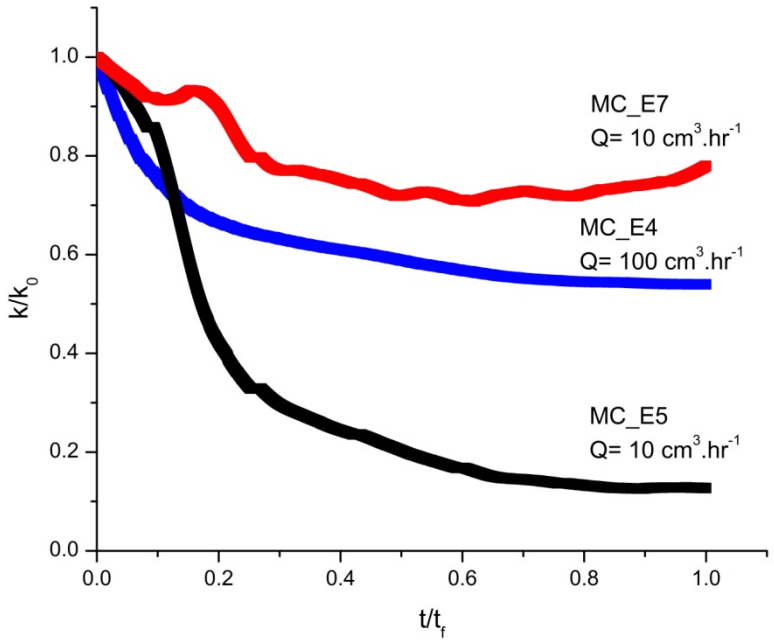

Figure 5.11: Comparison of normalized permeability among the percolation experiments at 15% mixing ratio.

In general, the permeability deduced from the percolation experiments was decreased rapidly at the beginning of injection followed by stage of slow reduction and finally it fluctuated around an average value.

Concerning the experiments with 15% salty solution, three samples from Mallorca (MC10_E4, E7 and E5) were used to carry out the percolation. Flow rate of 100 ($cm^3.hr^{-1}$) was applied for the MC10_E4 and 10 ($cm^3.hr^{-1}$) was applied for MC10_E7 and E5. Dissolution of Calcite was observed at the outlet solution for all experiments, the dissolved Calcite was more in the case of flow rate of 10 ($cm^3.hr^{-1}$), probably because the solution resides more time inside the sample which improve kinetic reactions and enhances Calcite dissolution. The pH of the injected solution was also affecting the amount of dissolved Calcite: the lower pH inlet solution caused more dissolution of Calcite. In all experiments, the outlet solution was always undersaturated with respect to Calcite.

5.1.2. Percolation experiment at 45% mixing ratio

5.1.2.1. MC10_E9 (Mallorca)

Before starting the experiment the system was cleaned using deionized water and disinfection solution (APABIO) which is peracetic-acid-based disinfectant with large spectrum: bactericide, fungicide, virucide, and sporicide.

The initial permeability was measured by injecting equilibrated water with the rock sample at different flow rates and Darcy law was applied to calculate the permeability. An average value of 45 mDarcy was considered as an initial value of the sample permeability with an initial porosity of 42%.

The mixing solution was prepared by adding the $CaCl_2$ and $NaHCO_3$ salts corresponding to the chemical speciation calculated using PHREEQC code. The mixing was done inside the tank with 5 liters of diluted NaCl in deionized water.

The pH of the injected water was in agreement with the calculated one from PHREEQC code as shown in Table (5.5).

The flow rate was fixed to 10 ($cm^3.hr^{-1}$), initially, flow was by pass the sample until both of pH at the inlet and outlet read the same value, then percolation was started and the outlet solution was sampled to follow the evolution of outlet solution chemistry.

Table 5.5: The chemical characteristics of injected solution from theoretical calculation (PHREEQC) and laboratory solution.

Solution	pH	Ca tot ($mol.l^{-1}$)	Na tot ($mol.l^{-1}$)	Cl tot ($mol.l^{-1}$)	Ω (CaCO3)	pCO_2
PHREEQC	7.56	1.99×10^{-3}	4.50×10^{-1}	4.50×10^{-1}	0.50	$10^{-2.39}$
Laboratory	7.53	2.095×10^{-3}	4.382×10^{-1}	4.50×10^{-1}	0.54	$10^{-2.33}$

As shown in Figure (5.12), the reduction of permeability was observed as in the previous experiments. The permeability decreased from 45 mDarcy to 10 mDarcy after 1250 pore volumes were injected, followed by a slow reduction until the end of percolation.

The pH of the outlet solution increased at the beginning of injection then fluctuated around a value of 7.8.

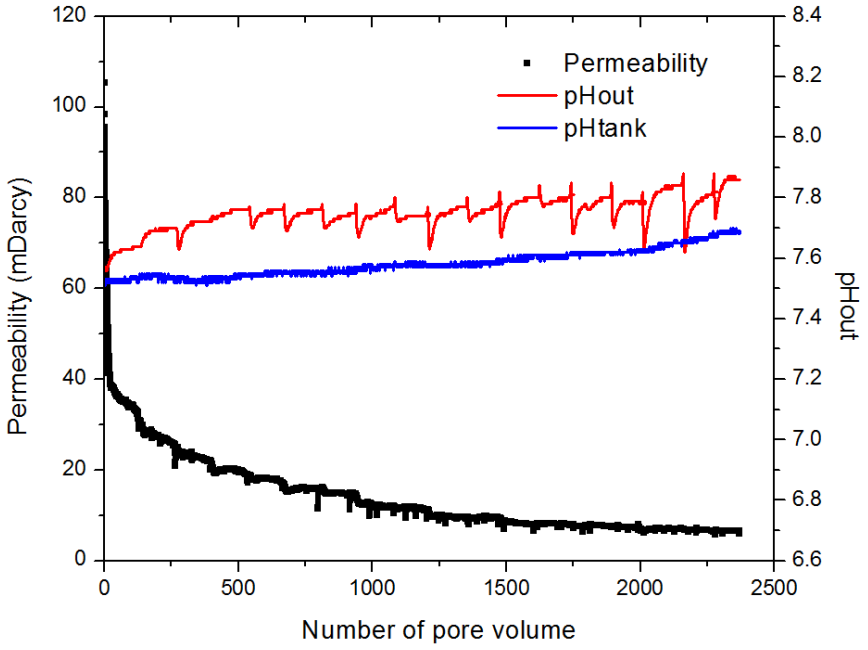

Figure 5.12: Time resolved permeability and pH at the sample outlet as a function of number of pore volume.

Concerning the chemical analysis of the outlet solution, precipitation of Calcite was observed (about 7.23 mg) according to the difference between the outlet and inlet Ca^{2+} concentration as shown in Figure (5.13), whereas dissolved Mg^{2+} was found in the outlet solution as shown in Figure (5.14). The observed precipitation of Calcite could be explained by the fact that presence of dissolved constituents such as Mg^{2+} often leads to $CaCO_3$ precipitation in the mixing zone at coastal aquifers (Wicks and Herman, 1996).

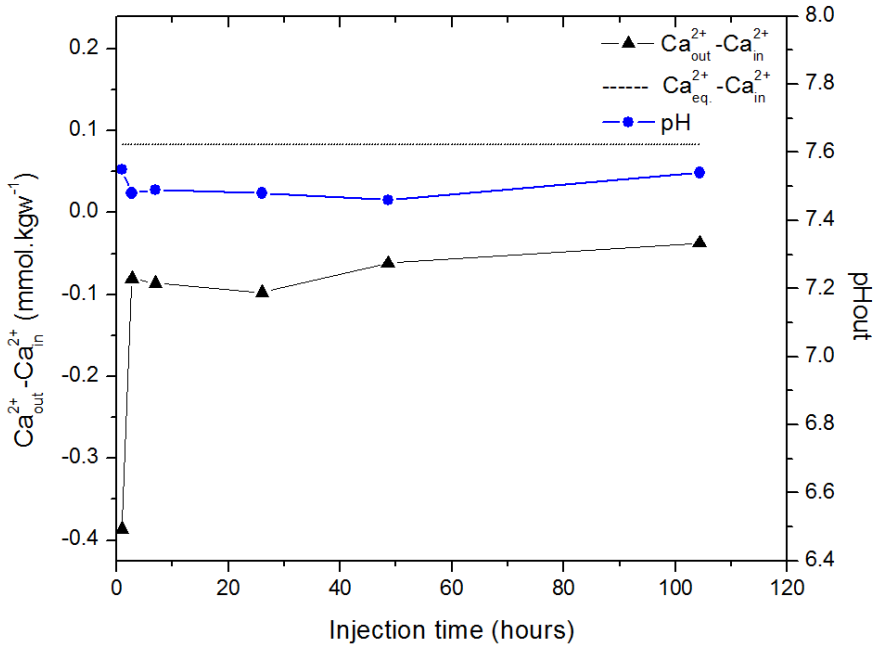

Figure 5.13: Evolution of ΔCa^{2+} concentration between the outlet solution and the input concentration, ΔCa^{2+} at equilibrium, and pH of the outlet solution.

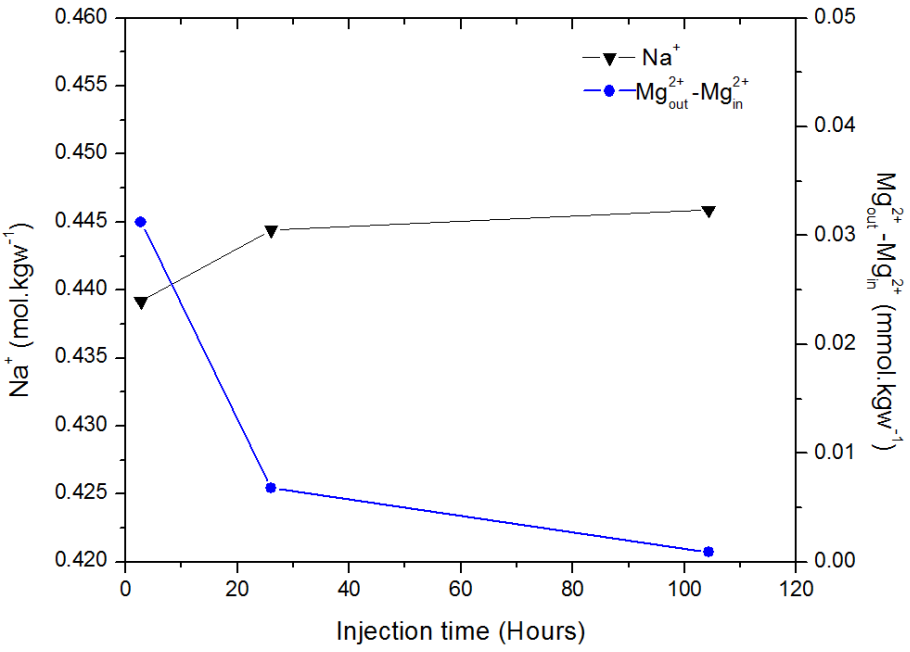

Figure 5.14: Na^+ in the outlet solution and ΔMg^{2+}concentration between the inlet and the outlet solutions.

5.1.2.2. Lav_E3 (Lavoux)

Before starting the experiment the system was cleaned using deionized water and disinfection solution (APABIO) which is peracetic-acid-based disinfectant with large spectrum: bactericide, fungicide, virucide, and sporicide.

The initial permeability was measured by injecting equilibrated water with the rock sample at different flow rates and Darcy law was applied to calculate the permeability. An average value of 4 mDarcy was considered as an initial value of the sample permeability with an initial porosity of 25%.

The mixing solution was prepared by adding the $CaCl_2$ and $NaHCO_3$ salts corresponding to the chemical speciation calculated using PHREEQC code. The mixing was done inside the tank with 5 liters of diluted NaCl in deionized water.

The chemical analysis of the injected solution calculated in PHREEQC and the laboratory solution is reported in Table (5.6).

The flow rate was fixed to 10 ($cm^3.hr^{-1}$) and the outlet solution was sampled to follow the evolution of solution chemistry.

Table 5.6: The chemical characteristics of injected solution from theoretical calculation (PHREEQC) and laboratory solution.

Solution	pH	Ca tot ($mol.l^{-1}$)	Na tot ($mol.l^{-1}$)	Cl tot ($mol.l^{-1}$)	Ω ($CaCO_3$)	pCO_2
PHREEQC	7.56	1.99×10^{-3}	4.50×10^{-1}	4.50×10^{-1}	0.50	$10^{-2.39}$
Laboratory	7.61	2.073×10^{-3}	4.541×10^{-1}	4.59×10^{-1}	0.63	$10^{-2.42}$

When the solution entered the sample, a permeability peak was observed followed by a linear reduction from 4 to 1.7 mDarcy during 40 hours of injection (equivalent to750 pore volume injection). Then a stage of stability with small fluctuations was observed (Figure 5.15).

The pH of the outlet solution increased at the beginning of injection then it became lower than the pH of the injected solution.

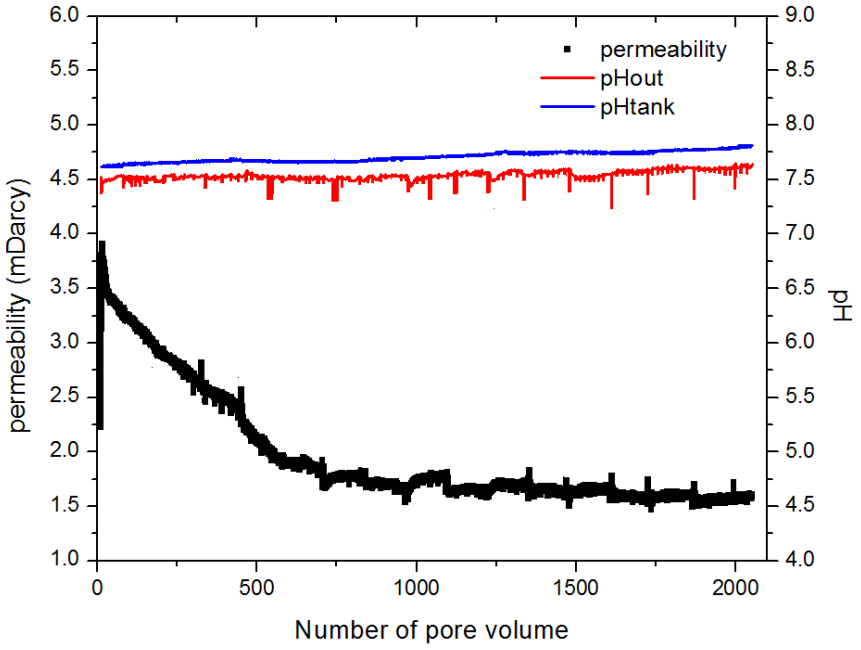

Figure 5.15: Time resolved permeability and pH at the sample outlet as a function of number of pore volume.

Concerning of the chemical analysis of the outlet solution, a high dissolution of Calcite was observed during the permeability peak at the beginning of injection. Then precipitation of Calcite was estimated according to the difference between the outlet and inlet Ca^{2+} concentration as show in Figure (5.16). The net amount of precipitated Calcite was 3.55 mg, whereas dissolved Mg^{2+} was found in the outlet solution and it was high at the first hour of injection and then it decreased until the end of injection as show in Figure (5.17).

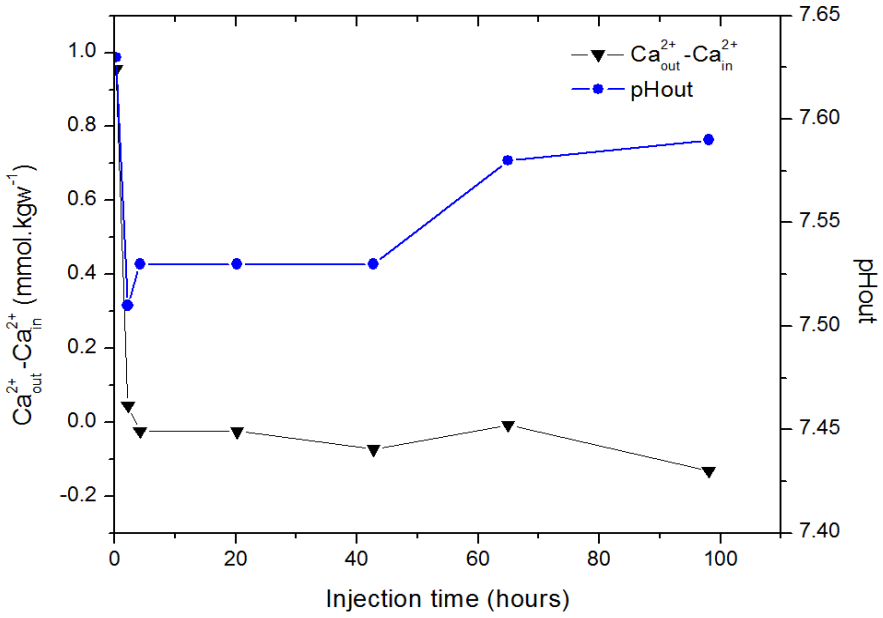

Figure 5.16: Evolution of ΔCa^{2+} concentration between the outlet solution and the input concentration; ΔCa^{2+} at equilibrium and pH of the outlet solution.

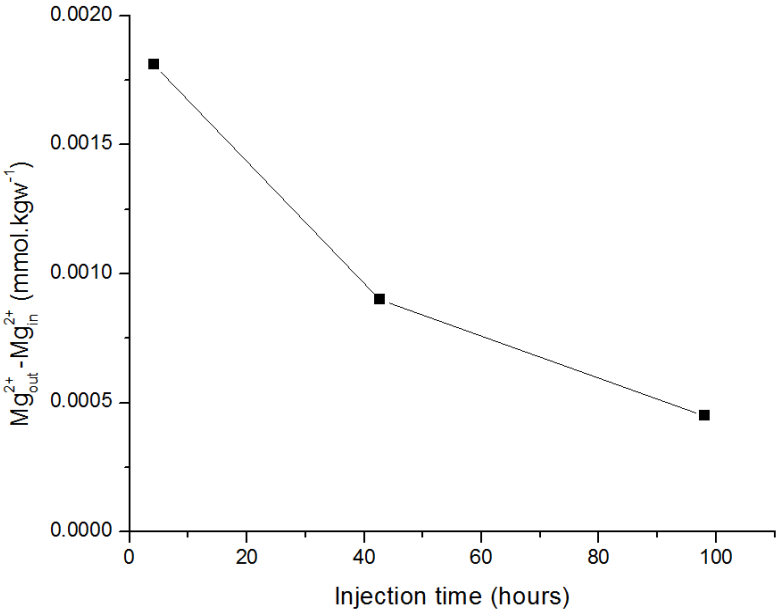

Figure 5.17: Evolution of ΔMg^{2+} concentration between the outlet and inlet solutions.

5.1.2.3. Lav_E1 (Lavoux)

Before starting the experiment the system was cleaned using deionized water and disinfection solution (APABIO) which is peracetic-acid-based disinfectant with large spectrum: bactericide, fungicide, virucide, and sporicide.

The mixing solution was prepared by adding the $CaCl_2$ and $NaHCO_3$ salts corresponding to the chemical speciation calculated using PHREEQC code. The mixing was done inside the tank with 5 liters of diluted NaCl in deionized water.

The sample was vacuumed and the injection started without measuring the initial permeability. The chemical analysis of the injected solution calculated in PHREEQC and prepared at the laboratory is reported in Table (5.7). We notice that pH, Ca^{2+} and consequently the saturation state of Calcite are lower than the theoretical calculation using PHREEQC, which reflects that laboratory solution has the potential to dissolve more Calcite than in both of previous two experiments **MC10_E9** and **Lav_E3**.

Table 5.7: The chemical characteristics of injected solution from theoretical calculation (PHREEQC) and laboratory solution.

Solution	pH	Ca tot ($mol.l^{-1}$)	Na tot ($mol.l^{-1}$)	Cl tot ($mol.l^{-1}$)	Ω (CaCO3)	pCo2
PHREEQC	7.56	1.99×10^{-3}	4.50×10^{-1}	4.50×10^{-1}	0.50	$10^{-2.39}$
Laboratory	7.48	1.672×10^{-3}	3.858×10^{-1}	3.858×10^{-1}	0.32	$10^{-2.36}$

The flow rate was fixed to 10 ($cm^3.hr^{-1}$) and the outlet solution was sampled to follow the evolution of solution chemistry.

The permeability increased for 100 hours of injection (equivalent to 2500 pore volume), then it started to decrease until the end of the percolation. The pH values of the inlet and outlet solution showed high fluctuation during the injection time, and the pH of the outlet solution was lower than the inlet one as shown in Figure (5.18). Dissolution of Calcite was observed at the outlet deduced from the difference in Ca^{2+} concentration between inlet and outlet solutions. The amount of dissolved Calcite calculated for 158 hours from the beginning of injection was about 11.54 mg.

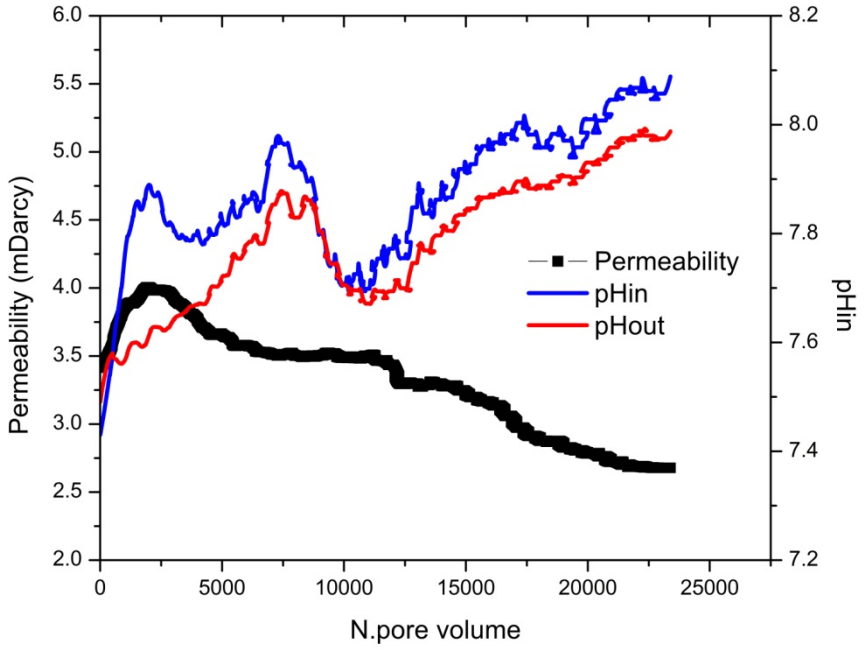

Figure 5.18: Time resolved permeability and smoothed value of pH at the sample outlet as a function of number of pore volume.

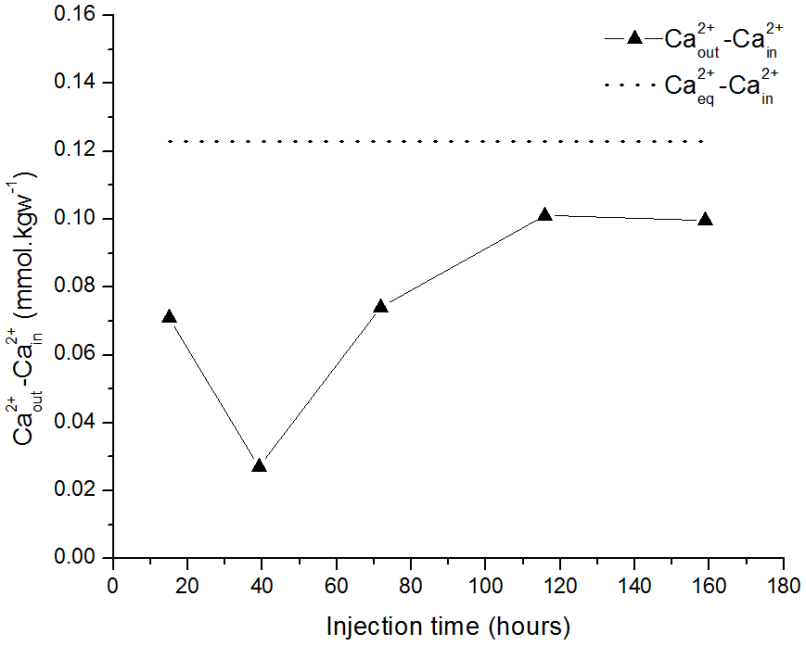

Figure 5.19: Evolution of ΔCa^{2+} concentration between the outlet solution and the input concentration; ΔCa^{2+} at equilibrium.

The outlet solution was always undersaturated with respect to Calcite as the difference between the outlet and inlet concentration was lower than the difference between Ca^{2+} at equilibrium and the inlet Ca^{2+} concentration as shown in Figure (5.19).

During **Lav_E1** experiment dissolution of Calcite we observed at the outlets solution in contrast during the other two experiments **MC10_E9** and **Lav_E3** precipitation of Calcite was observed according to the difference in Ca^{2+}concentration between the out and inlet solution. In general the amount of dissolved Calcite at **Lav_E1** was lower than in those experiments carried out at 15% which in conceptual because the saturation state of the injected solution was higher for those experiments at 45% than for those at 15%.

A comparison among the percolation experiments carried out at 45% of salty water in terms of normalized permeability showed a general behavior of permeability reduction especially at the beginning of injection as shown in Figure (5.20). The permeability reduction was faster in the case of MC_E9 (Mallorca) than in the case of Lav_E3 and Lav_E1 (Lavoux) taking into consideration that the initial permeability of Mallorca sample is higher than Lavoux samples.

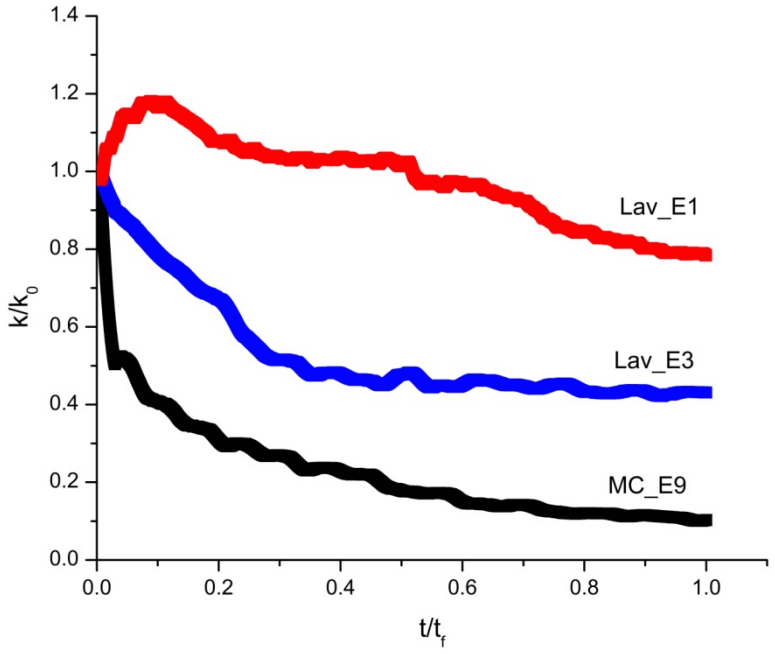

Figure 5.20: Comparison of normalized permeability among the percolation experiments at 15% mixing ratio.

It is interesting to note that the permeability reduction display some relationship with the water/rock ratio in which permeability reduction was faster for sample with high porosity (Mallorca) than for sample with low porosity (Lavoux).

By comparing Lav_E1 and Lav_E3, one can observe that dissolution observed in Lav_E1 causes permeability increase at the beginning of injection then it decreases later probably due to microparticles accumulation at the sample outlet.

So far we investigated the effect of injecting two mixed solutions that were initially in equilibrium with Calcite but at different PCO_2 using two mixing ratios of 15 and 45%. Two samples with different structure, porosity, permeability and composition were used to carry out percolation experiments. The first rock samples were cored from Mallorca site with high porosity of 45% and permeability range of 45-100 mDarcy that composed of Calcite enriched with Magnesium. The second samples were cored from Lavoux site with relatively low porosity of 25% and permeability range of 4-10 mDarcy that composed approximately of 99.7% Calcite.

Permeability reduction was observed for all the experiments and it was faster for Mallorca sample than for Lavoux samples. Calcite dissolution was observed for all experiments except for MC10_E9 and at the end of Lav_E3 low precipitation of Calcite was observed.

In the Lav_E1 experiment, permeability increased during few hours at beginning of injection then reduction in permeability was observed. Also dissolution of Calcite was measured at the outlet.

In spite of Calcite dissolution, the sample permeability decreased, which suggests once more the hypothesis of a rearrangement of sample structure: detachment and mobilization of Calcite grains, clogging of pores, and the consequent decrease of permeability.

Hereafter sorts of percolation experiments are conducted under different dissolution regimes in order to understand the evolution of permeability induced by dissolution reactions.

5.2. Permeability evolution under long term injection of deionized water

The following experiments were carried out by injection of deionized water (Table 5.8). The purpose of these experiments is to examine the hydraulic and geochemical behavior of tested sample upon injection of deionized water by following the evolution of permeability due to Calcite dissolution.

Table 5.8: Summary of experiments carried out with deionized water injection.

Experiment ID	Flow rate ($cm^3.hr^{-1}$)	k_{ini} (mDarcy)	K_{final} (mDarcy)	Duration (hours)	Dissolved Calcite (mg)
MC10_E2	10	50	23.45	302	115.7
MC10_T1	10	330	19.2	268.9	35.6

5.2.1. MC10_E2 (Mallorca)

Before starting the experiment a solution of 10% Apabio (bacterial disinfection) was used to clean the circuit from any bacterial contamination followed by de-ionized water, and then the percolation experiment was started. The system was vacuumed and the pH meters were calibrated using standard solutions, injection of deionized water started at a flow rate of 10 $cm^3.hr^{-1}$. The sample was saturated under vacuum and initial permeability was at the beginning of injection was about 45 mDarcy. The injected deionized water was analyzed to measure the concentration of Ca^{2+}, $Mg2^{+}$, Na^{+} and Cl^{-} then the outlet solution was sampled to follow the evolution of these species due to rock water interaction.

Reduction in permeability was observed during the first 25 hours then the permeability increased for 150 hours and later decreased until the end of the experiment. The pH of the inlet water was 5.84 and at the outlet it increased rapidly reaching to a maximum value of 7.9 in the first 5 hours then it decreased gradually until reaching 7.65 before fluctuating around a value of 7.6 until the end of the experiment as shown in Figure (5.21).

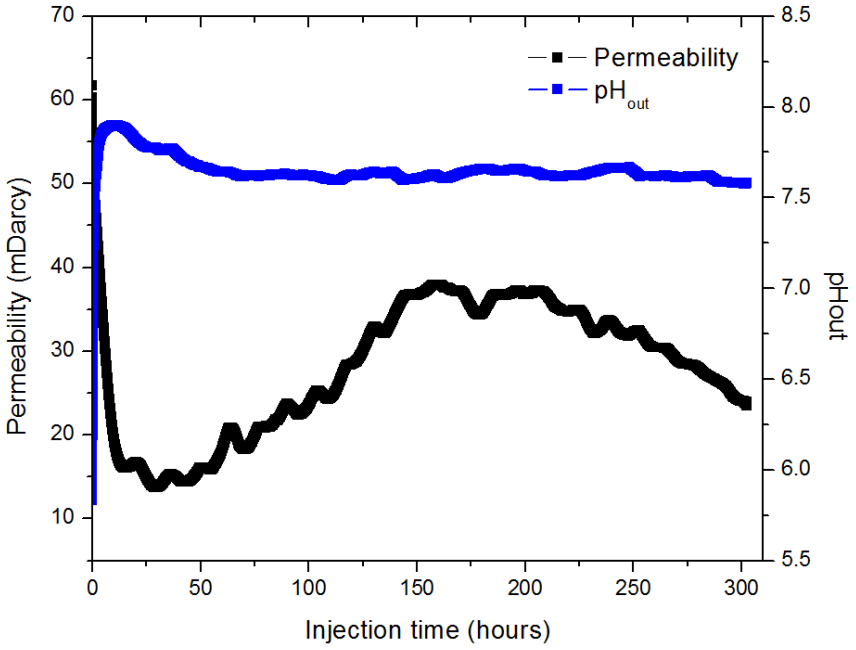

Figure 5.21: Evolution of permeability and pH at the outlet.

The permeability reduction during the first 5 hours is corresponding to the high dissolution of Ca^{2+} at the outlet that took place on the cement layer connecting Calcite grains that generates a huge number of micro particles that are detached, transported, and accumulated in micropores that become consequently clogged. At the same time, these microparticles are continually dissolved (chemical dissolution) and their resistivity to fluid flow decreases yielding a permeability increase. The later decrease of permeability is probably caused by a new pore clogging due to another process of detachment-transport-accumulation of micropoarticle. The evolution of permeability is quite similar to the evolution of Ca^{2+} (Figure 5.22), which supports the hypothesis that when the Calcite dissolution is relatively high the permeability decreases due to migration of microparticles towards the outlet causing blocking of some of connected pores.

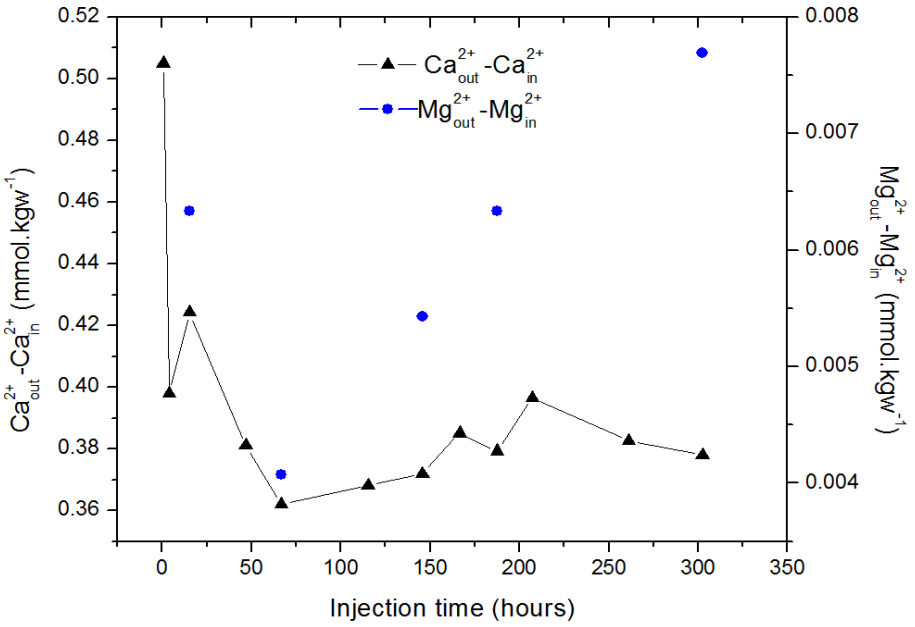

Figure 5.22: Evolution of ΔCa^{2+} and ΔMg^{2+} concentration between the outlet solution and the input concentration.

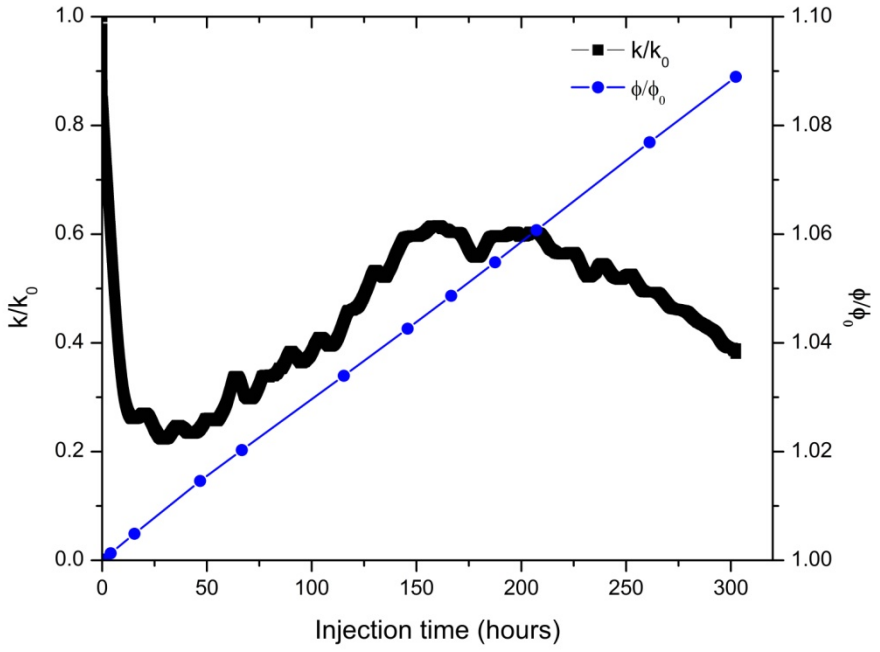

Figure 5.23: Evolution of normalized permeability and porosity corresponding to the sampling time of outlet water.

As mentioned in Figure (5.23), the permeability reduction at the beginning is linked to the sample structure variation and the clogging caused by microparticle deposition in finer pores. The porosity of the tested sample increased due to the dissolution of Calcite, this increase in porosity due to Calcite dissolution was enough high to contribute to permeability increase. The total amount of dissolved Calcite calculated at the end of experiment **(Lav_E1)** was 115.7 mg.

5.2.2. MC10_T1 (Mallorca)

The same protocol of cleaning and preparation of the experimental branch was applied as in previous experiment **MC10_E2**.

X-ray micro tomography imaging of the tested sample was performed before and after the experiment to deduce the change on local porosity and structure variations.

Deionized water (milli-Q) water was sterilized and used for injection. The initial permeability of the tested sample was about 330 mDarcy at the beginning of the percolation which is higher than the previous sample **MC10_E2**.

The evolutions of permeability as well as the evolution of chemistry of the outlet water are shown in Figures (5.24) and (5.25).

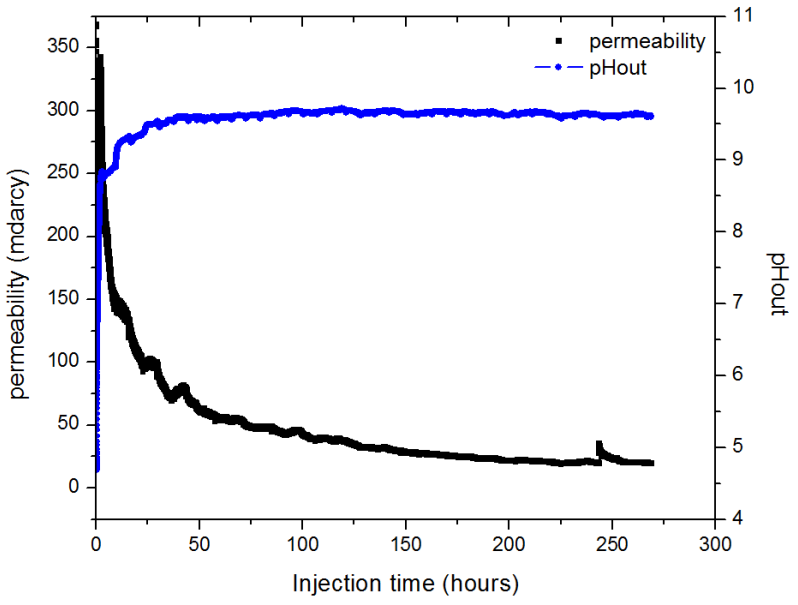

Figure 5.24: Evolution of permeability and pH at the outlet.

At the first 25 hours of injection the permeability decreased rapidly supported by high Calcite dissolution at this time and migration of microparticles towards the outlet which clog the micropores causing permeability reduction until reaching to a stage of balance (constant permeability) between the production of microparticles and their chemical dissolution.
Regarding to the chemical analysis one can observe that the dissolution was higher at the first 25 hours than at the rest of the experiment, the total amount of dissolved Calcite calculated at the end of the percolation was about 35.6 mg.

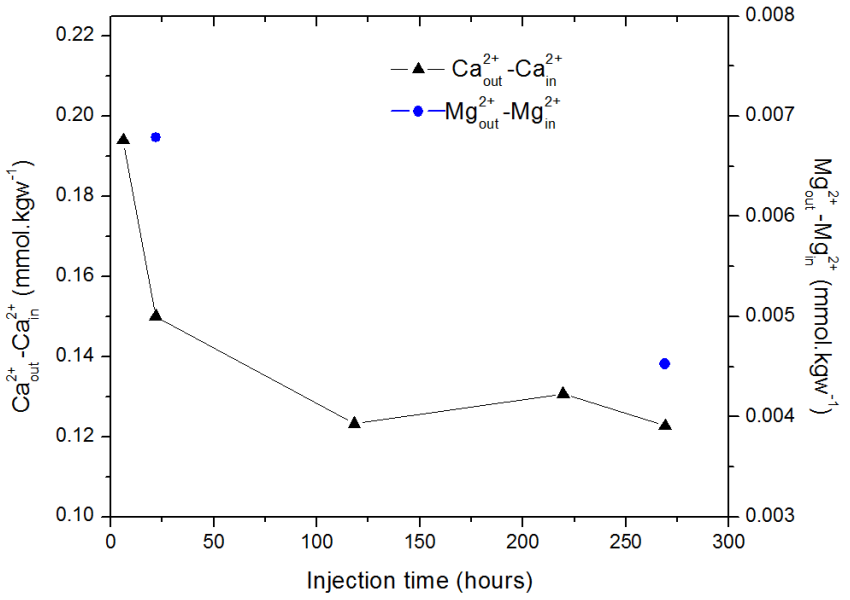

Figure 5.25: Evolution of ΔCa^{2+} and ΔMg^{2+} concentration between the outlet solution and the input concentration.

The permeability reduction at the beginning seems to be linked to the sample structure variation and the clogging caused by micro particle deposition. The porosity of the tested sample increased due to the dissolution of Calcite (Figure 5.26), but this increase in porosity due to Calcite dissolution was not high enough to contribute to permeability increase.

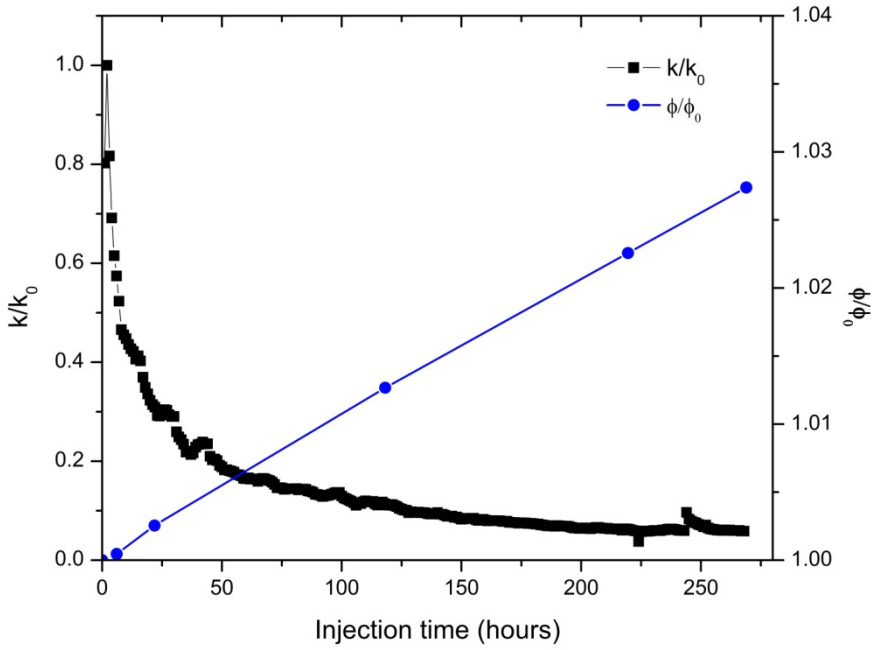

Figure 5.26: Evolution of ΔCa^{2+} and ΔMg^{2+} concentration between the outlet solution and the input concentration.

Comparing both experiments **MC10_E2** and **MC10_T1** (Figures (5.27) and (5.28)) in terms of permeability change and dissolved Calcite, we can deduce that the sharp permeability reduction occurred at the beginning of injection about 25 hours from the starting point. Permeability reduction could be explained by the redistribution of the sample structure and migration of microparticles from the inlet of the sample towards the outlet which causes clogging of pores, and consequently the permeability decreases. After this period of permeability reduction, the dissolution rate starts to affect the porosity and permeability starts to increase as in the case of **MC10_E2**. On the other hand if the dissolution rate is not high enough to affect the porosity, consequently the permeability remains decreasing until reaching a stage of equilibrium between the dissolved Calcite and the production of microparticles as in the case of **MC10_T1**. The total dissolved Calcite in **MC10_E2** and **MC10_T1** was 115.7 and 35.6 mg respectively, which reflect that when more Calcite is dissolved, the permeability starts to increase as in the case of **MC10_E2**. Conversely, the amount of dissolved Calcite in MC10_T1 was not enough to enhance the permeability increase during the percolation.

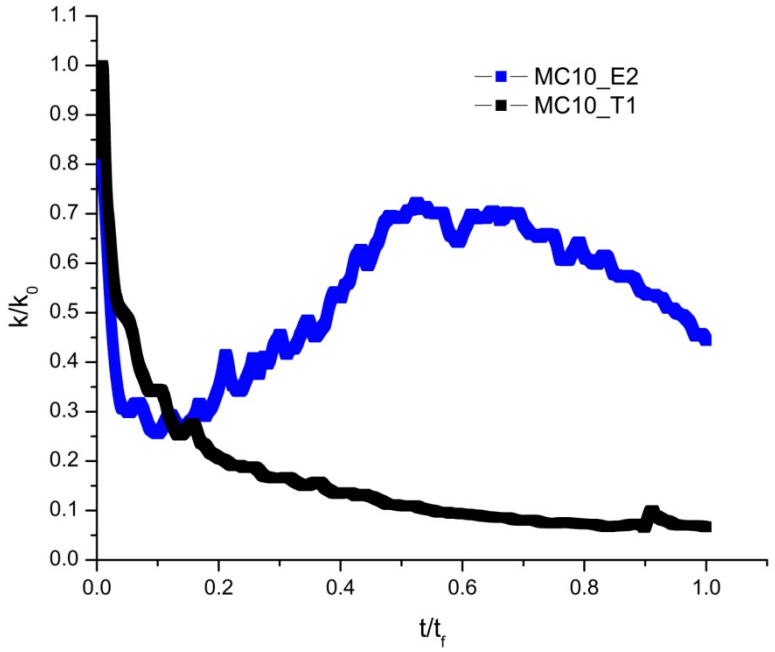

Figure 5.27: Comparison between MC10_E2 and MC10_T1 in terms of normalized permeability evolution during the injection.

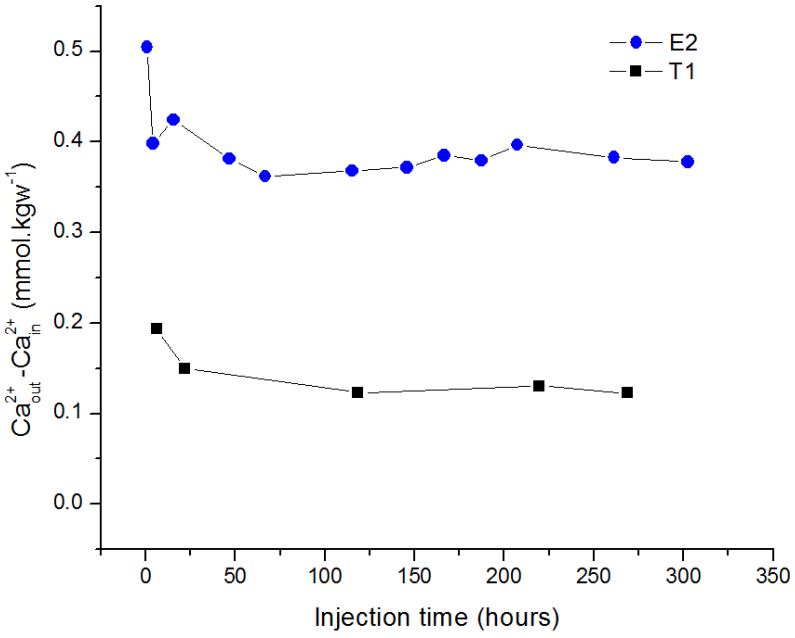

Figure 5.28: Comparison between MC10_E2 and MC10_T1 in terms of ΔCa^{2+} concentration between the outlet solution and the input concentration.

The permeability reduction in tested samples might be related the microparticles produced from the dissolution of cemented layers among the Calcite grains, which are detached, transported, and eventually accumulated in micropores leading thus to clogging and causing permeability decrease.

If we consider the competition between the process of micro particle "production" (due to detachment) and the Calcite chemical dissolution process, the permeability variation of the sample can follow different scenarios:

- When the production of Calcite micro particles is higher than the chemical dissolution, permeability decreases.
- When both processes are in equilibrium, permeability does not change.
- When the dissolution process is higher than produced micro particles, permeability increases.

In order to confirm above mentioned scenarios of the permeability variation, a series of experiments was carried out where deionized water and deionized water enriched with CO_2 were sequentially injected in the rock samples.

5.3. Permeability evolution under sequential injection of deionized water and deionized water enriched with CO_2

In the previous experiments **MC10_E2** and **MC10_T1**, permeability reduction was related to microparticles deposition in micropores at the beginning of the injection then the increase of permeability in **MC10_E2** was related to the ongoing process of dissolution. When the reaction rate was high the permeability increased. In order to verify this phenomenon, percolation experiments were carried out by sequential injection of deionized water followed by deionized water enriched with CO_2 to enhance dissolution reactions. These experiments intended thus to examine the response of permeability to the degree of chemical reactivity of the injected solution. Details of these experiments are summarized in Table (5.9).

The flow rate was fixed at 10 $cm^3.hr^{-1}$, two tanks were used to provide the injected water, one for the deionized water and the other one for the deionized water enriched with CO_2.

All the experiments were started by the injection of deionized water followed by the injection of deionized water enriched with CO_2.

CO_2 gas was added using a manual pump with a net volume of 24.8 cm^3. The pump was filled with CO_2 at 5 bars from a CO_2 bottle connected to the tank. The pH evolution was recorded until it reached a stable value. The corresponding pCO_2 was calculated using PHREEQC code and it was $10^{-1.5}$ bars. The total mass of dissolved CO_2 was 1.099×10^{-3} $mol.kg^{-1}$ of water.

Table 5.9: Summary of experiments carried out with sequential injection of deionized water and deionized water enriched with CO_2.

Experiment ID	Flow rate ($cm^3.hr^{-1}$)	K_{ini} (mDarcy)	K_{final} (mDarcy)	Duration (hours)
Lav_MK[1,2]	10	3	>20	426.5
MC10_E13[1,2,3]	10	90	>120	264

[1] Chemical analysis of outlet solution was done.
[2] Scan electron microscopy SEM was performed after percolation.
[3] XRMT analyses were performed before and after percolation.

5.1.1. Lav_MK (Lavoux)

The experimental system was cleaned and vacuumed. An initial permeability of 3 mDarcy was measured using Calcite equilibrated solution whereas the porosity of 25% was measured for a Lavoux twin sample using the triple method. The system was cleaned and vacuumed again using the same procedure as in the previous experiments. The initial and final conditions (duration, pH_{in} and $pH_{out,}$ permeability ($K_{ini.}$ and $K_{fin.}$) and mass of dissolved Calcite) at each stage of injection are reported in Table (5.10).

The evolution of both permeability and pH at the outlet was monitored using the data acquisition system. The outlet solution was sampled to follow the evolution of solution chemistry in terms of Ca^{2+}, Mg^{2+}, Na^{+} and Cl^{-} concentration. SEM analysis was performed for a thin section after the end of percolation.

Table 5.10: Summary of experimental stages carried out with sequential injection of deionized water and deionized water enriched with CO_2.

Injected water	Duration (hours)	pH_{in}	pH_{out}	K_{ini} (mDarcy)	K_{final} (mDarcy)	Dissolved Calcite (mg)
1st (H_2O)	0-20	5.7	9.7	3	1.9	0.12
2nd ($H_2O + CO_2$)	20-155	4.84	7.6	1.9	8	9.2
3rd (H_2O)	155-326	5.7	9.5	8	5.9	3.7
4th ($H_2O + CO_2$)	326-end	4.84	7.3	5.9	>20	8.2

The evolution permeability and pH at the outlet are shown in Figure (5.29). We can summarize their evolution in the following four stages:

- During the 1st stage of injection, permeability decreased from 3 to 1.9 mDarcy and the pH at the outlet increased from 5.7 at the inlet to 9.7 at the outlet, whereas the pH at equilibrium with Calcite is 9.84 (Calculated using PHREEQC).
- During the 2nd stage of injection, permeability increased from 1.9 to 8 mDarcy and the pH at the outlet increased from 4.84 at the inlet to 7.6 at the outlet whereas the pH at equilibrium with Calcite is 7.67 (Calculated using PHREEQC).

- During the 3rd stage of injection, permeability decreased from 8 to 5.9 mDarcy and the pH at the outlet increased from 5.7 at the inlet to 9.5 at the outlet, whereas the pH at equilibrium with Calcite is 9.84 (Calculated using PHREEQC).
- During the 4th stage of injection, permeability increased from 5.9 to >20 mDarcy and the pH at the outlet increased from 4.84 at the inlet to 7.3 at the outlet, whereas the pH at equilibrium with Calcite is 7.67 (Calculated using PHREEQC).

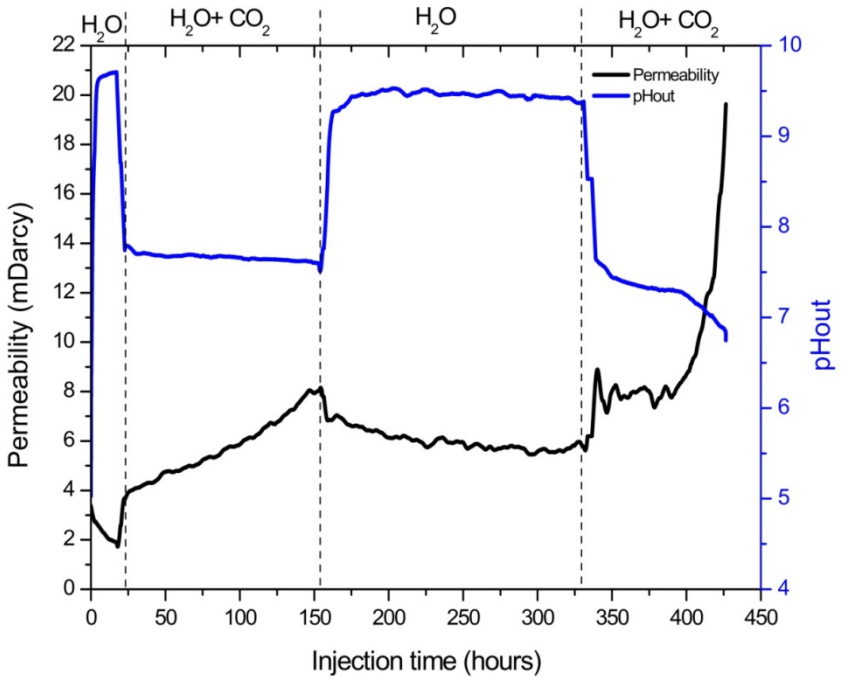

Figure 5.29: Evolution of permeability and pH at the outlet during the sequential injection.

The chemical analyses of outlet solutions in terms of ΔCa^{2+} and ΔMg^{2+} are indicated in Figure (5.30). Evolution of ΔMg^{2+} at the outlet was higher during the 2nd and 4th stages (H_2O+CO_2) than in 1st and 3rd stages (H_2O), which is relevant to the of evolution ΔCa^{2+} as follows:

- During the 1st stage of injection, ΔCa^{2+} was 0.15 (mmol.kgw^{-1}), which is very close to the calculated Ca^{2+} at equilibrium with Calcite (0.124 mmol.kgw^{-1}).
- During the 2nd stage of injection, ΔCa^{2+} was 0.95 (mmol.kgw^{-1}), which is very closed to the calculated Ca^{2+} at equilibrium with Calcite (1.02 mmol.kgw-1).

- During the 3rd stage of injection, ΔCa^{2+} was 0.124 (mmol.kgw^{-1}), which is equal to the calculated Ca^{2+} at equilibrium with Calcite (0.124 mmol.kgw^{-1}).
- During the 4th stage of injection, ΔCa^{2+} at the last sampled solution was 1.02 (mmol.kgw^{-1}), which is equal to calculated Ca^{2+} at equilibrium with Calcite (1.02 mmol.kgw^{-1}).

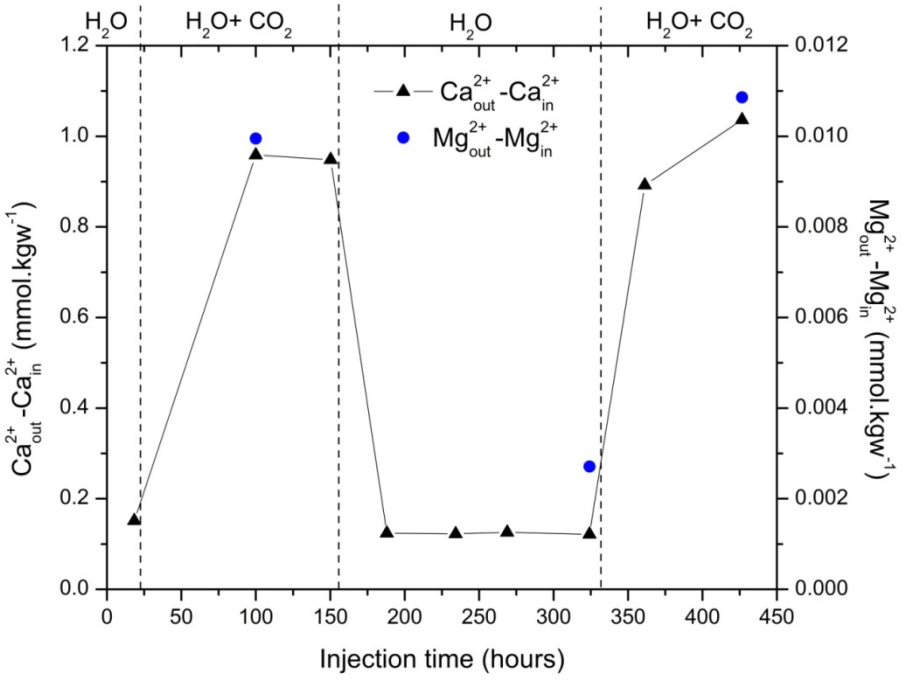

Figure 5.30: Evolution of ΔCa^{2+} and ΔMg^{2+} concentration between the outlet solution and the input concentration.

Concerning the relation between permeability and porosity deduced from chemical dissolution of Calcite (Figure 5.31) we can highlight the following:

- Permeability decrease during the 1st stage is corresponding to a constant porosity.
- Permeability increase during the 2nd stage is corresponding to porosity increase due to high dissolution rate of Calcite during this stage.
- Permeability decrease during the 3rd stage is corresponding to very little increase in porosity because the dissolved Calcite during this stage was not high enough to increase permeability.

- Finally at the 4th stage of injection, significant increase of both permeability and porosity was observed.

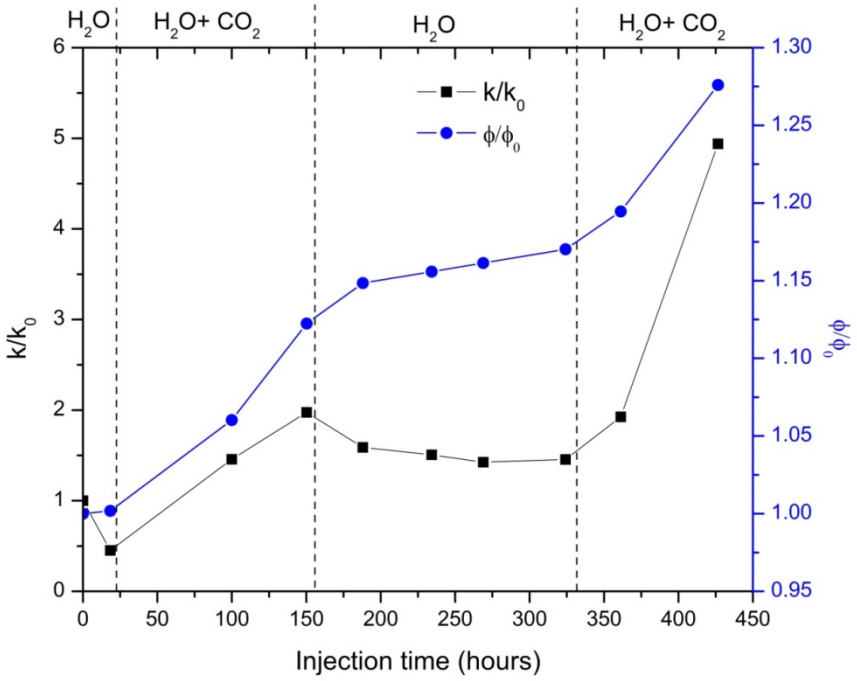

Figure 5.31: Evolution of permeability and porosity normalized to initial permeability and porosity respectively during different stages of injection.

Based on the results obtained from percolation experiment **Lav_MK**, we can conclude that the evolution of permeability is affected by two processes operating simultaneously but with different time scales depending on the injected solution reactivity, the first process consists of the detachment of Calcite microparticles and the second process is dissolution of these microparticles.

When the injected solution is moderately reactive (deionized water), a rapid detachment of micro particles occurs on short term leading to pore clogging (permeability decrease). On the other hand a slow process consisting of chemical dissolution of Calcite which occurs on a long term leads to a higher porosity (permeability increase). The combination of those two processes leads to permeability reduction in short term and permeability increase in long term.

When the injected water is high reactive (deionized water enriched with CO_2), both detachment and dissolution processes occur but the dissolution process prevails the detachment process i.e. the detached microparticles are dissolved and exit from the sample outlet which leads to increase in both permeability and porosity.

Therefore, the main driving force of permeability decrease is the detachment of microparticles, whereas the main driving force of permeability increase is the reactivity of injected solution (i.e. chemical dissolution process).

The SEM (scan electron microscopy) analysis at the end of percolation was performed where a longitudinal thin section was scanned laterally from the inlet to the outlet.

The scanned sections were collected and arranged from the top to the bottom of the sample to form the longitudinal cross section and observation was reported as shown in Figure (5.32).

One can observe particles detachment at the sample inlet (clearly close to the sample wall), these Particles were crumbled due to flow of injected solution and dissolution of cement layer among them. This crumbling process produces detached microparticles that travel along the sample depending on their size. The dissolution feature are spatially distributed, more dissolution feature are clearly occurs in the zone with finer size because of the higher reactive surface area. There are some wormholes close to the sample left hand side as indicated in site (f) in Figure (5.32)

Spectrums were taken at different sites along the sample to elucidate the chemical atomic percentage of the main elements C, O, Ca and Mg and they are illustrated in Figure (5.32) and summarized in Table (5.11). From the chemical atomic percentage we can detect that spectrums 1, 2, 3, 4 and 5 are quite identical, Calcium atomic percentage was higher for white grains than for those having a grey color, hence the dissolution occurs in the grey grains (micropore phase) more than in white grains due to the large specific surface area of grey particles. The spectrum 6 was taken for a very small particle (5microm) that contain less Calcite in comparison to the other spectrums.

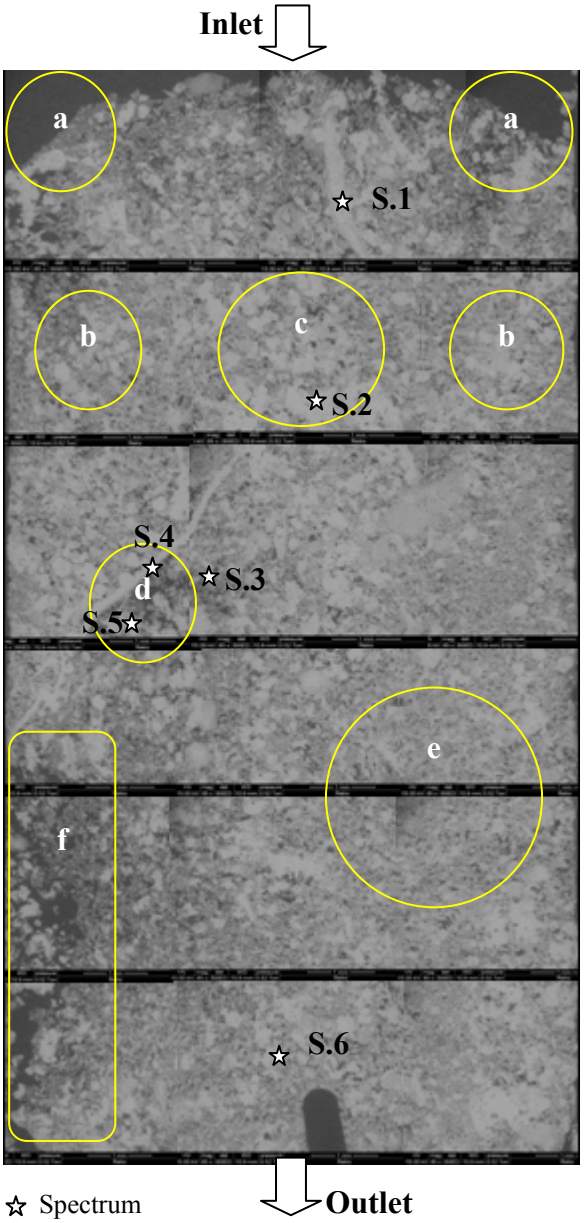

Observations

(a) Particles detached at the inlet of the sample. Dissolution features represented in the grey color (miropore phase), pure Calcite grain in white color and macropores in black.
The porosity in this zone is high because of particles migration.

(b) This zone is characterized by combination of macropores that are connected by micropore phase.

(c) The Calcite particles are smaller close to the sample wall rather than in the middle of the sample.

(d) These are some algae Dissolution features at this point looks like a wormhole because of the preferential flow through these pores.
(e) The particles in this zone are finer than the upper zones.

(f) Wormhole features are clearly represented close to the sample wall.
The dissolution features showed that the dissolution gradient is oriented from right to left towards the wormhole.

Figure 5.32: Longitudinal cross section of the Lav_MK sample used to perform SEM analysis at the end of the sequential injection.

The SEM images provided useful information in terms of structure variations of the tested sample as shown in Figures (5.32) and (5.33) the images proofed the particles detachment processes from the sample inlet, moreover the crumbling of these particles due to dissolution which lead to finer grain size towards the outlet of the sample.

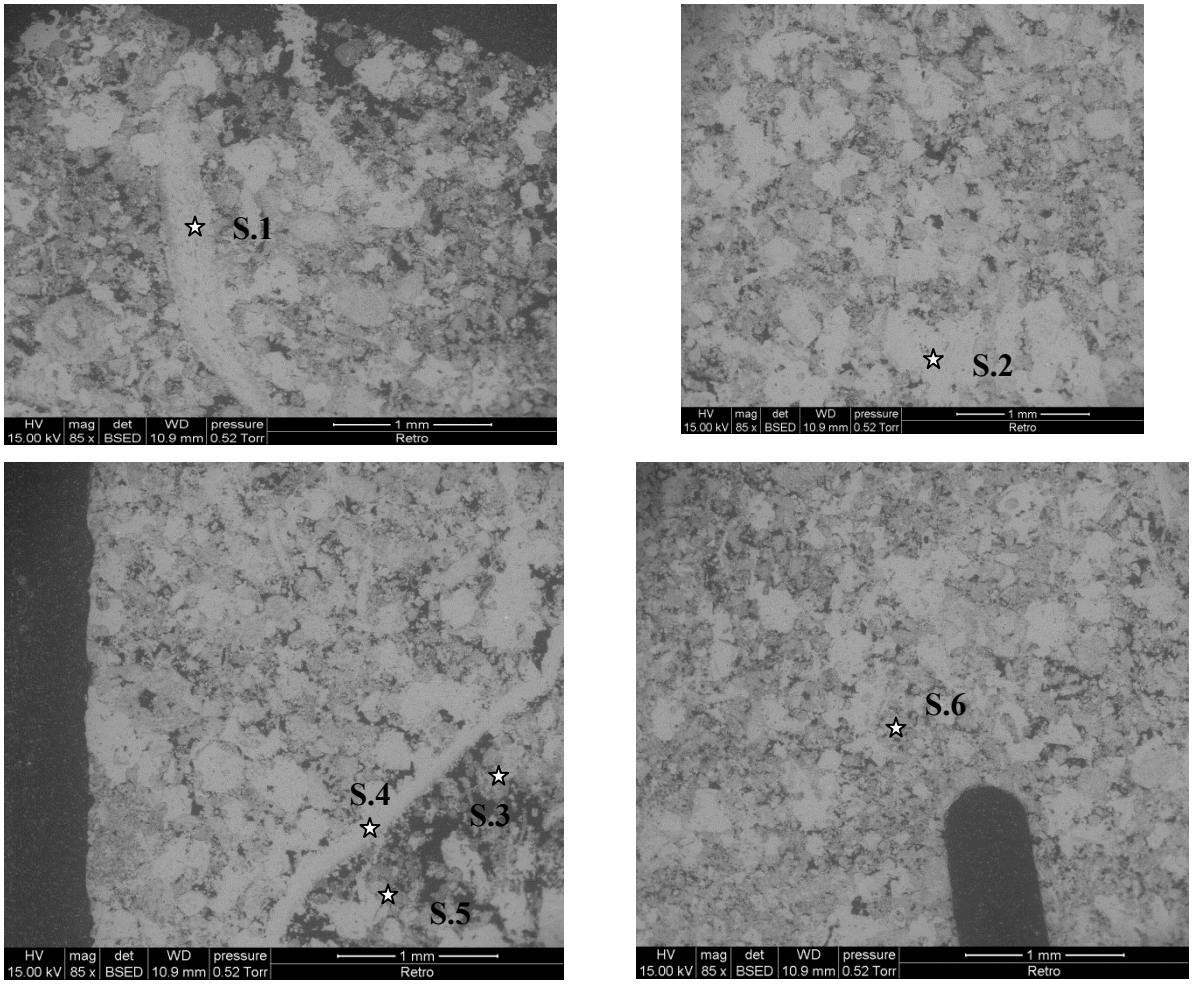

Figure 5.33: SEM images where the spectrums were taken of the Lav_MK at the end of the sequential injection.

Table 5.11: Summary of experiments carried out with sequential injection of deionized water and deionized water enriched with Calcite.

Element/Spectrum	**Ca** (Atomic %)	**Mg** (Atomic %)	**C** (Atomic %)	**O** (Atomic %)
S. 1	12.69	0.21	40.28	46.82
S. 2	13.58	0.09	35.12	51.21
S. 3	11.53	0.18	42.00	46.28
S. 4	14.51	0.17	31.06	54.26
S. 5	12.32	0.16	39.74	47.79
S. 6	6.67	0.17	22.55	70.62

5.1.2. MC10_E13 (Mallorca)

The same protocol of cleaning and vacuum was used to prepare the setup for percolation. Mallorca sample was used to perform the percolation test. XRMT analysis was performed for the tested sample before percolation and another analysis was done after the end of percolation to study the structure variations due to the sequential injection of deionized water and deionized water enriched with CO_2. The initial porosity of the sample was measured using the triple method and initial porosity of 40% was estimated. The initial and final conditions (duration, pH_{in} and $pH_{out,}$ permeability ($K_{ini.}$ and $K_{fin.}$) and mass of dissolved Calcite) at each stage of injection are reported in Table (5.12).

The evolution of both permeability and pH at the outlet was monitored using the data acquisition system. The outlet solution was sampled to follow the evolution of solution chemistry in terms of Ca^{2+}, Mg^{2+}, Na^{+} and Cl^{-} concentration.

Table 5.12: Summary of experimental stages carried out with sequential injection of deionized water and deionized water enriched with CO_2.

Injected water	Duration (hours)	pH_{in}	pH_{out}	K_{ini} (mDarcy)	K_{final} (mDarcy)	Dissolved Calcite (mg)
1st (H_2O)	0-108	5.7	7.5	90	39	35
2nd (H_2O + CO_2)	108-264	4.84	6.4	39	>120	219

The evolution permeability and pH at the outlet are shown in Figure (5.34). We can summarize their evolution in the following four stages:

- During the 1st stage of injection, permeability decreased from 90 to 40 mDarcy during 30 hours then it showed some fluctuation until the end of this stage, while the pH at the outlet increased rapidly from 5.7 at the inlet to 7.5 at the outlet, whereas the pH at equilibrium with Calcite is 9.84 (Calculated using PHREEQC). The fluctuation in permeability might be due to the migration of some microparticles, so when these particles move they could block the connected pores simultaneously they dissolve and the pore channel is partially open which causes permeability fluctuations.

- During the 2nd stage of injection, permeability increased from 39 to 50 mDarcy during 15 hours then it dropped to about 29 mDarcy then it increased gradually with some fluctuations until it reached to120 mDarcy at the end of percolation, while the pH at the outlet increased from 4.84 at the inlet to 6.7 at the outlet the it decreased gradually with some fluctuations until it reached 6.4 at the end of percolation whereas the pH at equilibrium with Calcite is 7.67 (Calculated using PHREEQC).

The permeability fluctuations are mainly due to the same mechanism of particles movement and dissolution. In this stage the injected water was more aggressive than the 1st stage, so more detached particles were produced and more fluctuations were observed, then the dissolution prevail the particle detachment and the sample became high permeable so we observed a rapid increase in permeability at the end of 2nd stage.

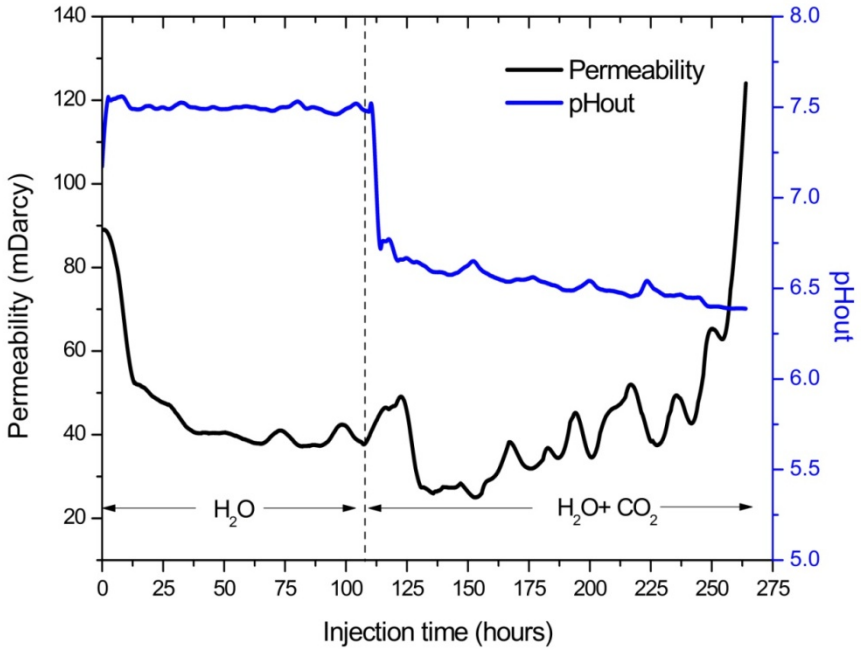

Figure 5.34: Evolution of permeability and pH at the outlet during the sequential injection.

The chemical analyses of outlet solutions in terms of ΔCa^{2+} and ΔMg^{2+} are indicated in Figure (5.35). The evolution ΔCa^{2+} was relevant to the in the pH at the outlet as follows:

- During the 1st stage of injection, ΔCa^{2+} was 0.33 (mmol.kgw^{-1}), which is higher than the calculated Ca^{2+} at equilibrium with Calcite (0.124 mmol.kgw^{-1}).
- During the 2nd stage of injection, ΔCa^{2+} was 1.8 (mmol.kgw^{-1}), which is also higher than the calculated Ca^{2+} at equilibrium with Calcite (1.02 mmol.kgw-1).

We observe that the dissolved Calcite between the inlet and the outlet is higher than the calculated one using PHREEQC this might be due to the fact that there were some detached particles from the tested sample into the outlet solution because their sizes are smaller than the minimum pore size at the outlet of the sample. When adding 200 µl of HCl at 5% to outlet solution, these particles are completely dissolved.

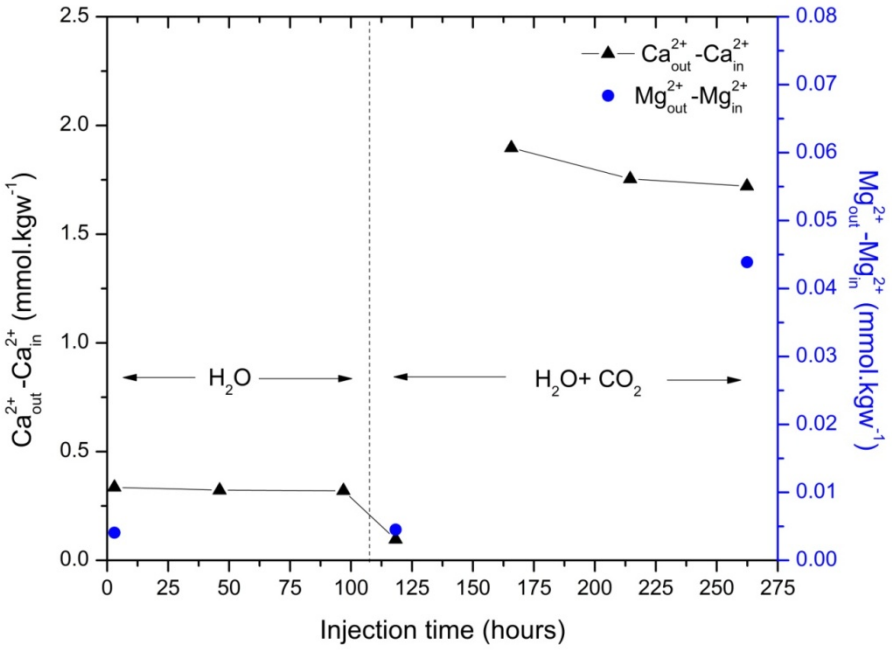

Figure 5.35: Evolution of ΔCa^{2+} and ΔMg^{2+} concentration between the outlet solution and the input concentration.

In order to have more evidences of the process of particle detachment and clogging, XRMT analysis was performed for the tested sample (**MC10_E13**) before and after percolation experiment as shown in Figure (5.36).

In Figure (5.36) we present some of XRMT images that were taken before and after the percolation at 0.6, 4.4 and 6 mm from the sample inlet. More details of XRMT analysis of Mallorca rock samples can be found in Garing (2011).
One can observe that for all the slices before the percolation the macro porous connected by microporous phase (pores < 5 microns) but after percolation we can observe the following:

- Comparing both images before and after percolation at 0.6 mm from the sample inlet we can clearly observe the process of detachment where approximately 80% of the matrix is detached and the macro porous phase became highly connected.
- Comparing both images before and after percolation at 4.4 mm from the sample inlet we can observe less detachment with respect to the previous images at 0.6 mm, but macro porous is still highly connected (see point a, b and a', b').
- Finally at 6 mm from the sample inlet we can observe the clogging process point (c) was a pore before percolation but after we can see that it is full of micro particles which proof the clogging processes at the lower half of the sample towards the outlet. From the middle of the sample to the outlet we observed that the macro porous phase is still connected by the microporous phase.

The phase ratio of macro porosity, micro porosity, matrix and indurate bioclasts were quantified before and after percolation as shown in Figure (5.37). Where the main diameter of each was found as follows:

- The main diameter of macro pores before and after percolation was found 93 and 907μm respectively.
- The main diameter of micro pores before and after percolation was found 39 and 47 μm respectively.
- The main diameter of bioclasts before and after percolation was found 88 and 98 μm respectively.

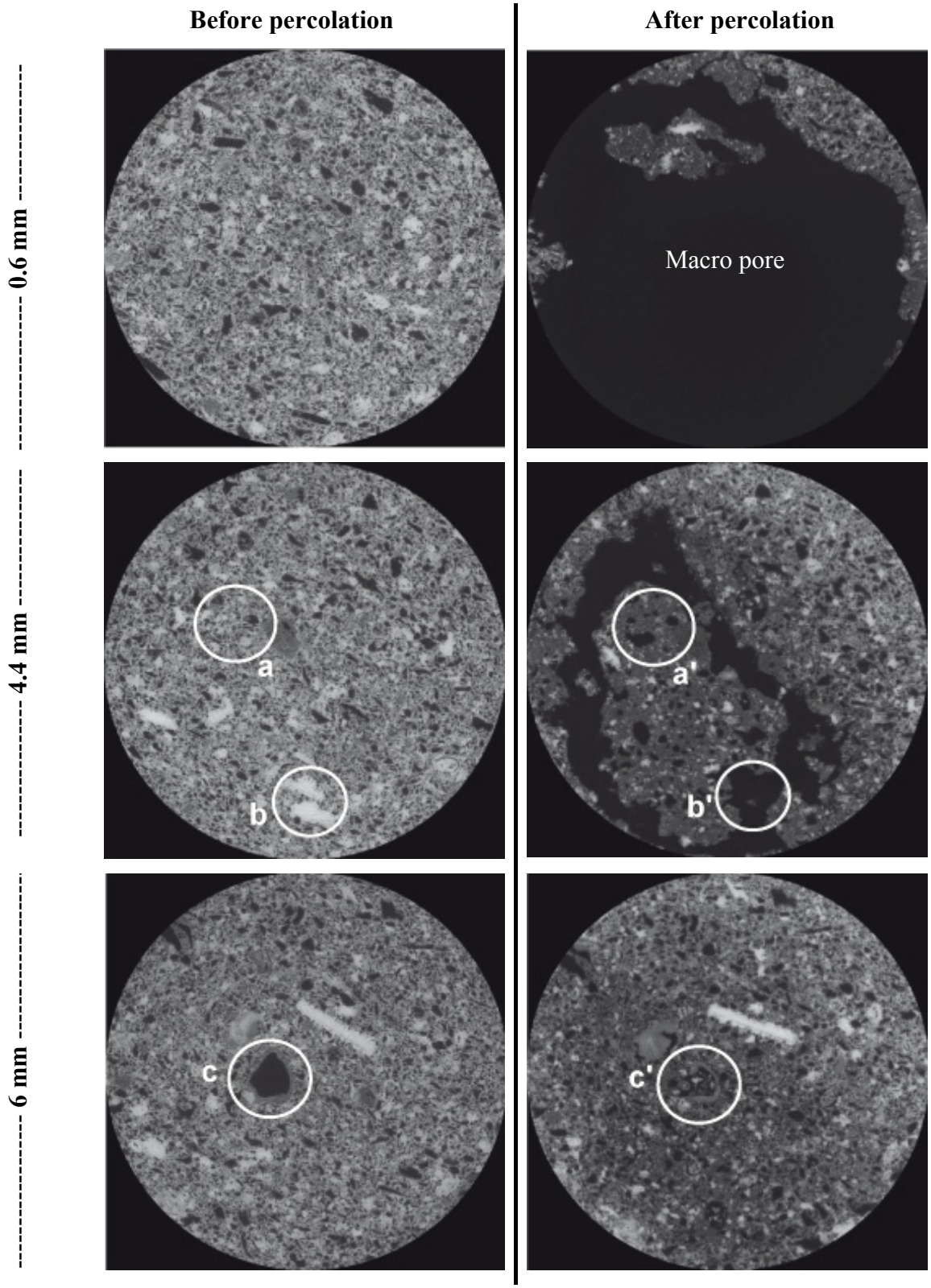

Figure 5.36: 2D XRMT images were taken before (on left) and after (on right) percolation at 0.6, 4.4 and 6 mm from the sample inlet (total sample length is 18 mm).

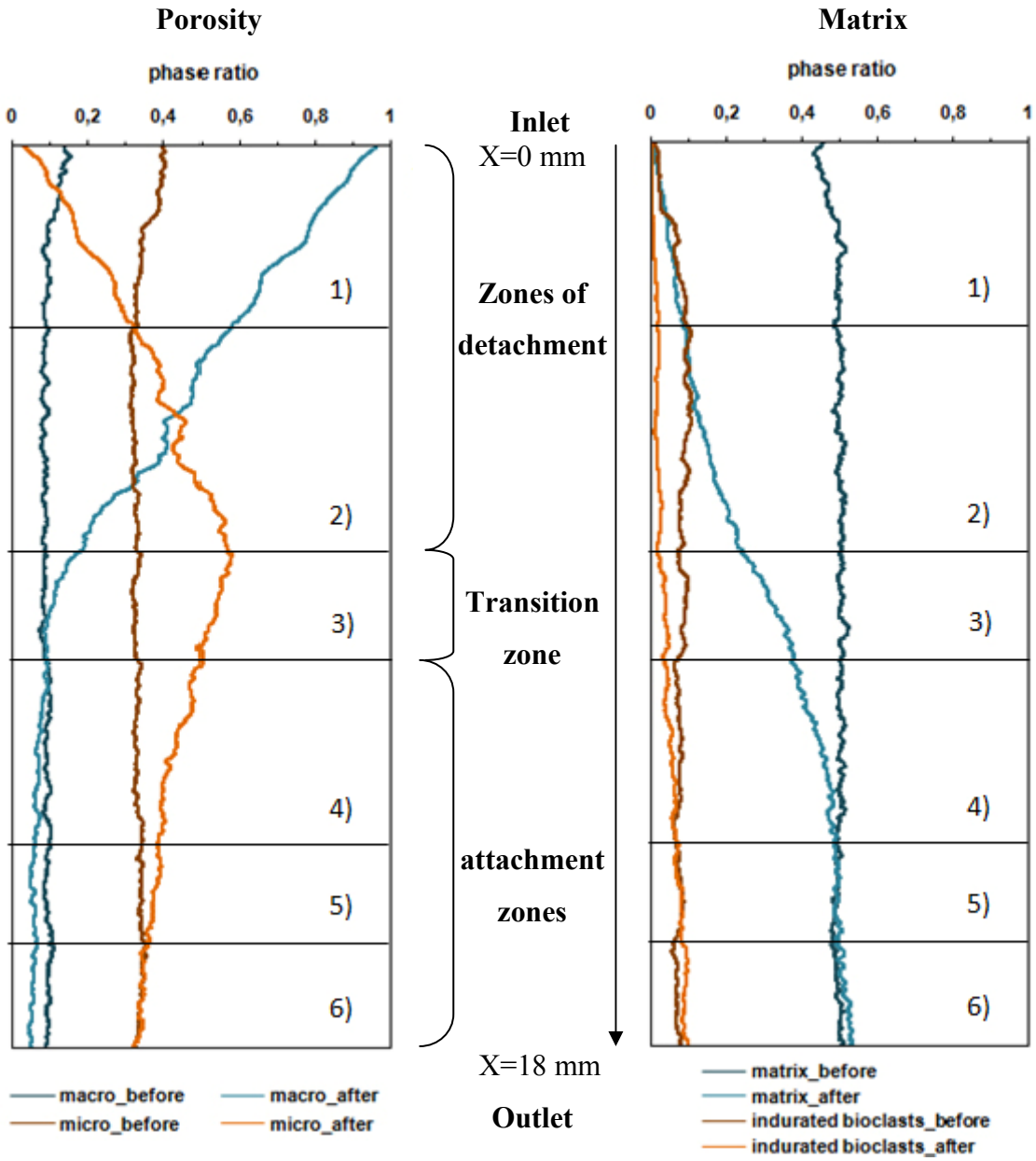

Figure 5.37: The growth in phase ratio of macro and micro porosity (on left) and the phase ratio of matrix and bioclasts (on right) along the sample calculated from XRMT images with a resolution of 5.06 micron before and after the percolation.

Combining both of figures (5.36 and 5.37) we can divide the sample into 6 zones based on the development of macro and micro porosity due to the particle detachment and clogging processes took place into the sample. One can observe that the macro and micro porosity are uniformly distributed along the sample in which macro and micro porous phases represent

about 12% and 35% respectively. In contrast the distribution after percolation is different especially in the upper part of the sample.

- The 1st zone corresponds to the sample inlet one can clearly see that the macro porous increased until 96% then it decreases gradually as we go far from the sample inlet. On the other hand the micro porous phase disappeared at the sample inlet then it start to increase far from the sample inlet until it became equal to the initial value. Also the matrix phase ratio decreased at this zone due to the detached particles and dissolution.
- At the 2nd zone one can notice that the macro porous phase continues to decrease but it is always higher than the initial value whereas the micro porous phase continues to increase and reaches a maximum value of 60 % due to particle crumbling process caused by dissolution of the matrix.
- The macro porous phase slightly increases with respect to the initial value where the micro porous phase started to decrease in comparison to the previous zone. This zone could be considered as an intermediate (transition zone) between the detachment zones (1st and 2nd) and attachment zones (4th, 5th and 6th).
- At the 5th zone one can see that the macro pours phase is less that the initial one and where the micro porous phase still higher than the initial and the matrix phase is almost constant.
- At the 6th zone one can see that macro phase is also less than the initial value where the micro porous phase is unchanged on the other hand the matrix phase ratio increased at the outlet of the sample.

The analysis of XRMT confirms our investigation of permeability variations during sequential injection of deionized water and deionized water enriched with Calcite.

Chapter 6

Modeling permeability evolution

6. Modeling permeability evolution

Based on the experimental results it is confirmed that the permeability reduction is caused by the detached micro particles transport and clogging mechanisms which are complex and can't be modeled in such heterogeneous porous media.

In this section we present a simplified approach to simulate permeability reduction induced by an equivalent processes namely particle splitting due to dissolution reactions. The percolation experiments have shown an intriguing temporal variation of sample permeability. While we expect that continuous percolation would lead to an increase of sample permeability (due to chemical dissolution of the porous media), our experimental results showed conversely that the sample permeability decreases under certain percolation conditions in the presence of dissolution. Some other experiments shows permeability increase when the injected solution is aggressive (high reactive) such as the case of DW enriched with CO_2. The main objective of elaborating a model is to understand the processes that might lead to a decrease of permeability during percolation in the presence of dissolution reaction. Hereafter, we present the model hypotheses, the approach used to solve the differential equations, the calibration of model parameters, the sensitivity analysis, and the results of model simulations.

The modeling approach presented in this section is based on the main experimental results concerning permeability evolution during percolation experiments. It was suggested that the decrease of permeability is due to the splitting of Calcite particles due to the dissolution of the cement layers among Calcite particles, consequently the sizes of these particles decrease.

We acknowledge that the spanning cluster that controls flow consists in series of macro and micro pores in which macro pores are connected by micro pores (Garing 2011). Therefore it is assumed that the permeability is controlled by such micro pores zone if harmonic mean is implemented.

The splitting process assumed in the present model is equivalent to the change in pore phase from macro to micro porous phase due to dissolution taking into consideration that the calcite particles don't move or at least don't agglomerate and create clogging zones.

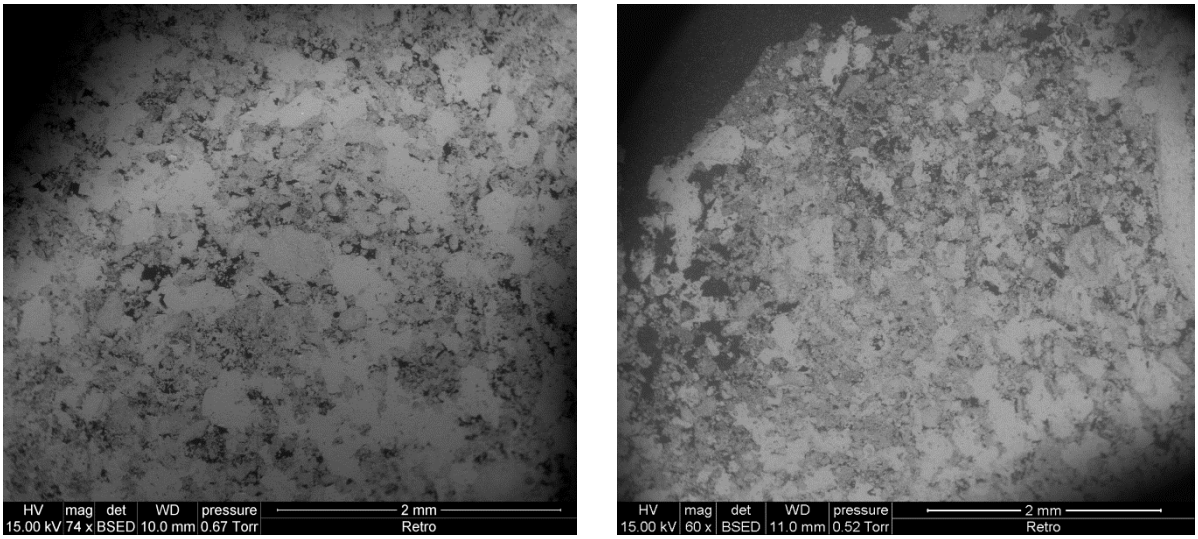

Figure 6.1: SEM images were taken before (left) and after (right) the percolation experiment show the splitting process in which the particle size decreases due to dissolution.

The scan electron microscopy analysis of the a thin section of the tested sample before and after percolation showed that the particles sizes are decreased after percolation and dissolution features are clearly found among these particles as shown in Figure (6.1).

Therefore the splitting process (crumbling) of the Calcite particles due to dissolution causes a decrease in particles sizes i.e. it became finer.

6.1. Model hypotheses

The first simplification considers that the complex original porous media is equivalent to a more homogeneous porous media consisting of spherical solid particles. Figure (6.2) illustrates the original and equivalent media have the same porosity however, the splitting process due to dissolution induce porosity increase of the equivalent media (the particles are drawn in a cubical shape to easily elucidate the splitting processes however, in the calculation the spherical shape of calcite particles is assumed).

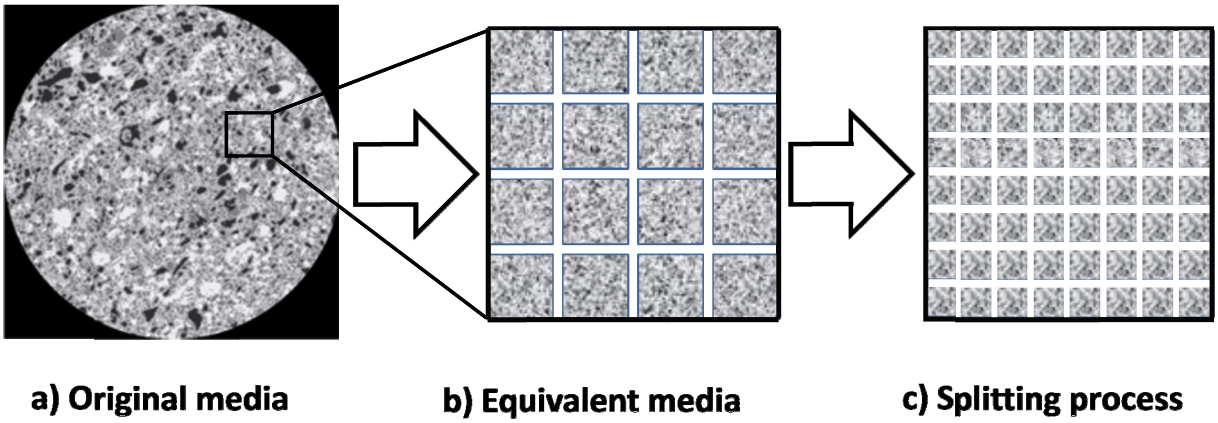

Figure 6.2: representation of the original (a), equivalent (b) porous media and resulted media from splitting process due to dissolution (c).

So it is assumed that there are two mechanisms took place simultaneously during percolation:

- Dissolution of the cement layers that connecting the Calcite particles consequently,
- These particles are crumbled into number of solid that are finer than the original one.

The idea here is to relate the evolution of permeability to the particle diameter and porosity changes due to dissolution considering the above mentioned mechanisms.

6.2. Permeability model

A number of rational and empirical equations relating permeability to porosity and grain size parameters exist. Many of these models are based on an empirical relationship developed by Kozeny, and later modified by Carmen, known as the Kozeny-Carmen equation (Bear, 1972). The two basic components of the equation are a particle-size (diameter) term and a porosity term. The diameter term is squared, derived as an expression of specific surface area with respect to a unit volume of porous medium. The porosity term (ϕ^3/ (1- ϕ)^2), where ϕ is fractional percent porosity.

The Kozeny-Carman equation (Carman, 1937) is often presented as permeability versus porosity, grain size, and tortuosity as follows:

$$k = \frac{\phi^3 \, D_p^2}{72 \, \tau \, (1-\phi)^2} \tag{6.1}$$

Where, k the absolute permeability (m^2) and ϕ is porosity (dimensionless), D_p is sphere diameter (m) and τ is tortuosity.

This form is frequently employed to mimic permeability versus porosity evolution in datasets, such as in Fontainebleau sandstone (Bourbie and Zinszner, 1985) or Finney packs (Finney, 1970). The Kozeny-Carman equation has been derived for a solid medium with pipe conduits, rather than for a granular medium and it considered that the particle diameter is constant.

Bearing this argument in mind, we explore how permeability can be predicted consistently within the Kozeny-Carman formalism, by varying the radii of particles. It requires additional assumptions, specifically, regarding tortuosity evolution during porosity increase due to dissolution and the fact that the number of particles is growing due to the splitting processes cause by dissolution.

The tortuosity is calculated using Pape et al, (1998) who theoretically derived a relation between tortuosity and porosity based on the assumption of fractal pore geometry in which:

$$\tau(\phi) \approx 0.67/\phi \tag{6.2}$$

6.3. Calculations

The calculations are based on the sample dimension (9×18 mm) used in the experimental part; it is characterized by initial porosity and permeability. The temporal evolution of permeability is related to the temporal evolution of particle diameter, porosity and tortuosity. The initial volume of Calcite solid (m^3) is calculated from the total volume of the sample and porosity as follows:

$$V_{solid_{(0)}} = \left(1 - \phi_{(0)}\right) \times V_{core} \tag{6.3}$$

Considering the reaction rate ($m^3.hr^{-1}$) obtained from the experimental data so we can calculate the temporal evolution in porosity as follows:

$$\phi_{(t)} = \phi_{(0)} + \frac{V_{diss}}{V_{core}} \tag{6.4}$$

Where: V_{diss} is equal to the dissolution rate ($m^3.hr^{-1}$) multiply by time (hr).

$$V_{solid_{(t)}} = \left(1 - \phi_{(t)}\right) \times V_{core} \tag{6.5}$$

The initial number of particle is deduced from Kozeny-Carman in which:

$$k_{(K-C)} = k_{ini} = \frac{\phi^3 \, D_p^2}{72 \, \tau \, (1-\phi)^2} \tag{6.6}$$

Knowing the initial measured permeability, initial porosity and corresponding tortuosity, so the volume of one particle V_p (m^3) is calculated from the particle diameter D_p (m) as follows:

$$V_p = {}^4/_3 \, \pi \left(\frac{D_p}{2}\right)^3 \tag{6.7}$$

$$N_{p_{(0)}} = V_{solid_{(0)}} / \, V_p \tag{6.8}$$

Now, let's assume the linear splitting processes which cause increasing of the particle number:

$$N_{p_{(t)}} = SR.t + N_{p_{(0)}} \tag{6.9}$$

Where, *SR* stands for the splitting rate (particle per unit time) and it is the only fitting parameter and it is a percentage multiplied by the initial number of particles.

At each time step the particle diameter is calculated as well as porosity and tortuosity and the corresponding permeability is deduced using equation (6.1).

Hereafter, sensitivity analyses are presented to examine the permeability variation under different levels of splitting and dissolution rates.

6.4. Sensitivity analysis of parameters

6.4.1. Splitting rate (*SR*)

Sensitivity analysis of normalized permeability as a function of splitting rate (particle.hr^{-1}) was performed by considering a porous media characterized by initial porosity (ϕ=0.4) and tortuosity of 1.675 is calculated from equation (6.2). The porosity update is only due to the dissolution reaction characterized imposed through the dissolution rate.

In general the permeability decreases rapidly at the beginning then it is evolve constantly, however the permeability decreases fast at higher splitting rate as shown in Figure (6.3).

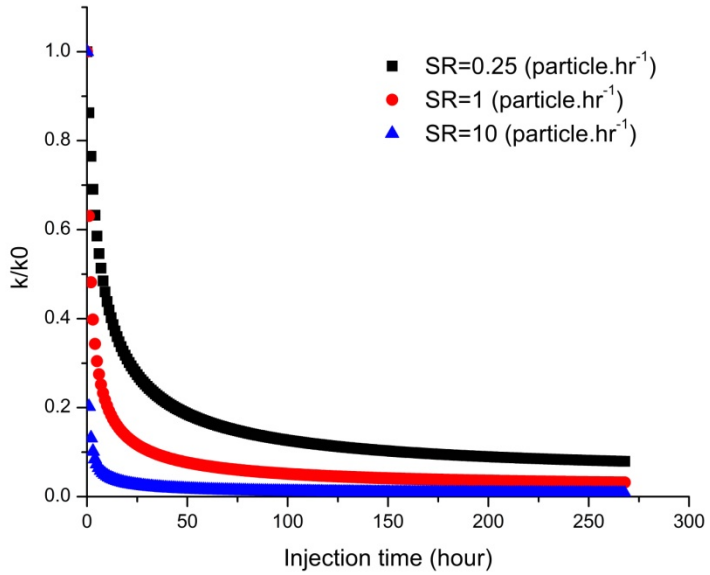

Figure 6.3: Evolution of permeability at various crumbling rates (note that porosity doesn't change with crumbling rate but it just changed as a function of dissolution rate (m^3.hr^{-1}).

6.4.2. Dissolution rate (DR)

As it was observed from the experimental part, the permeability was affected by the rate of dissolution (Dissolution rate m^3 of Calcite per hour). The sensitivity analysis showed that the permeability decrease at the beginning due to the splitting process however at higher reaction rate the permeability increase later because the dissolution reaction prevail splitting processes, meanwhile, the porosity of the sample always increase due to dissolution.

The permeability evolution as a function of dissolution rate is simulated assuming that the splitting rate is constant as shown in Figure (6.4).

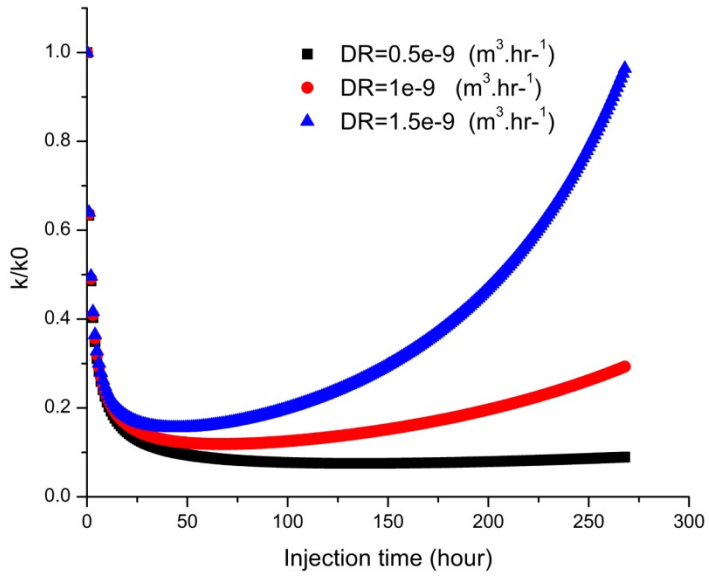

Figure 6.4: Evolution of permeability at various dissolution rates ($m^3.hr^{-1}$).

6.5. Modeling percolation experiments

The evolution of permeability obtained from percolation experiments was model using Kozeny- Carmen model taking into consideration additional assumptions, specifically, regarding to splitting processes and porosity increase due to dissolution.

The dissolution rate in m^3 of dissolved Calcite per hour was calculated from the chemical analysis of the outlet solution.

The initial permeability of the tested sample used to calculate the equivalent initial number of Calcite particles as mentioned in equations (6.6), (6.7) and (6.8).

The only fitted parameter used is the splitting rate of particles which is a percentage multiplied by the initial number of particles. Table (6.1) summarizes the experimental conditions, initial and final permeability in addition to the dissolution and the splitting rate for the modeled experiments.

Table 6.1: Summary of the modeled experiments

Exp.ID	Injected solution	Duration (hours)	K_{ini} (mDarcy)	K_{final} (mDarcy)	DR ($m^3.hr^{-1}$)	SR ($par.hr^{-1}$)
MC10_E4	15% (mixing)	40	21.3	9.92	1.8×10^{-9}	$0.16\times Np_{ini}$
MC10_T1	D.W.	268	330	19.2	4.8×10^{-11}	$0.25\times Np_{ini}$
MC10_E13	D.W	0-108	90	39	8.0×10^{-10}	$0.10\times Np_{ini}$
	D.W+CO2	108-264	39	>120	1.8×10^{-9}	$0.10\times Np_{ini}$

Hereafter, the measured and the modeled permeability for **MC10_E4**, **MC10_T1** and **MC10_E13** are plotted as a function of injection time as shown in Figures (6.5), (6.6) and (6.7) respectively.

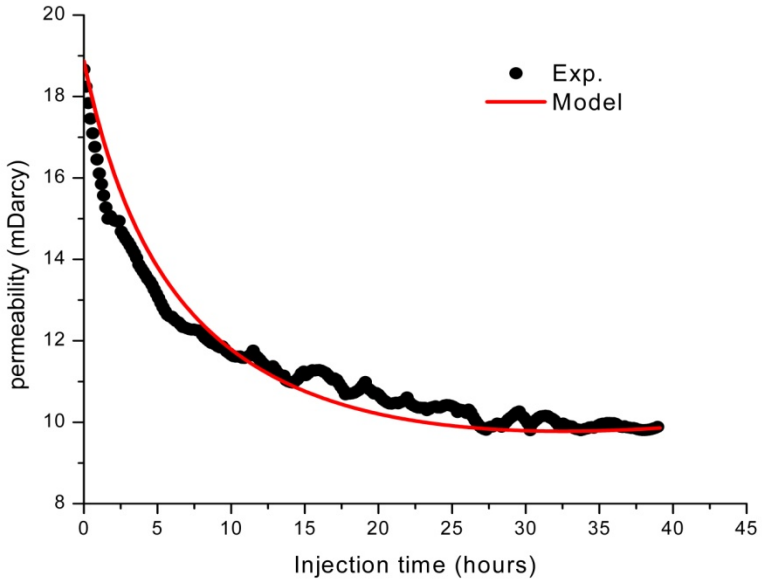

Figure 6.5: Evolution of permeability predicted by K-C model compared to experimental data of MC10_E4.

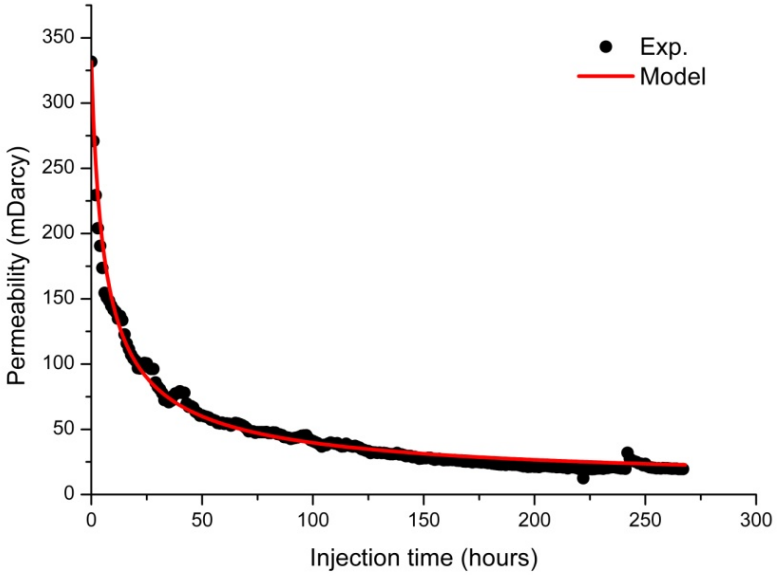

Figure 6.6: Evolution of permeability predicted by K-C model compared to experimental data of MC10_T1.

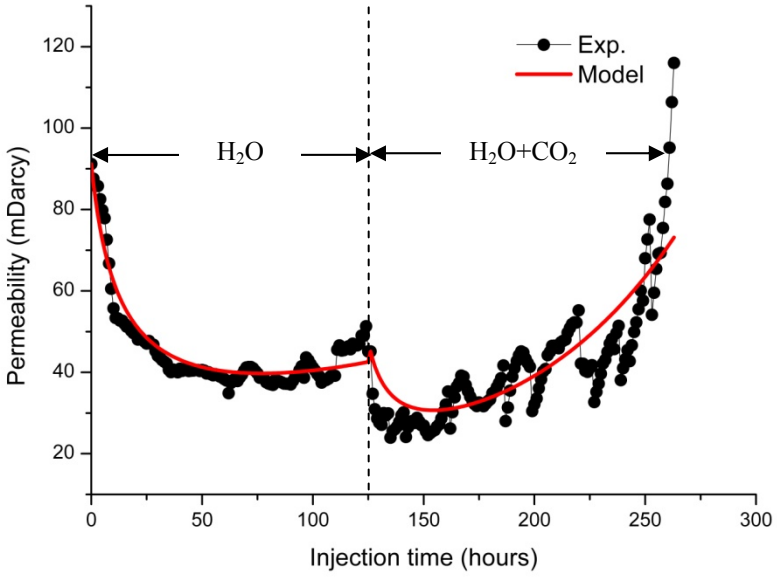

Figure 6.7: Evolution of permeability predicted by K-C model compared to experimental data of MC10_E13.

One can observe that the model shows an excellent agreement with the experimental data taking into consideration the splitting processes that occurs in the tested sample in which the Calcite grains are curmblied. This partitiing process leads permeabiliity to decrease because the resistance of pore network to the flowing fluid increases with small particle diameters.

This model considered as a first step to understand the permeability behavior under the prescriped experimental conditions. It is a simplified approach to model the permeability evolution considereing an equlivalent porous media consists of identical spherical particles. More complexation can be added to enhance the model predictivity such as the particles shape parameter, particle size distribution and the effective porosity as well as relating splitting factor to the dissolution reaction.

Chapter 7

Conclusion and perspective

7. Conclusions and perspectives

Understanding of geochemical processes that take place into coastal carbonate aquifers due to seawater intrusion is a major step towards charactering of subsequent changes in hydraulic and physical properties of these aquifers.

Results presented here provide insight on the interplay between chemistry and transport in the mixing zone of coastal carbonate aquifers.

Mixing of seawater or saline subsurface water with fresh water has been identified as the potential site of many geochemical processes. Dissolution and precipitation are two of the most important processes affecting groundwater chemistry, and they can significantly modify the physical and chemical properties of porous media.

In order to better understand and quantify mixing-driven mineral dissolution and the subsequent effects of these reactions on the physical and hydraulic properties in coastal environments, we have conducted laboratory-scale percolation experiments where hydrodynamic and geochemical reactions were combined in one setup to study evolution of permeability induced by dissolution reactions in a natural Carbonate system.

Two limestone samples were cored from a coastal zone at Mallorca in Spain and Parisian aquifer at Paris- France, respectively which represent a carbonate natural system.

The experimental setup allowed continuous measurements of permeability of the tested samples as well as the pH of the inlet and outlet solution during percolation experiments.

The first part of laboratory experiments designed to investigate dissolution of $CaCO_3$ upon mixing between carbonate-saturated fresh- and salt-water solutions under different CO_2 partial pressures. Two mixing ratios of 15 and 45% of artificial salty solution were chosen to represent the maximum subsaturation and the maximum dissolution until equilibrium obtained from PHEEQC respectively.

Experimental results indicated that dissolution rate of Calcite at 15% was higher than at 45% which is in contract with the pure geochemical modeling results mentioned in Chapter 3. The dissolution is relative to the saturation state. Low saturation state implies high dissolution rate. The dissolution is potentially occurs with low mixing ratio than for high mixing ratio under the prescribed experimental conditions. The outlet solution from the sample reactor was always undersaturated with respect to Calcite but in the model calculation the solution

was mixed then it was equilibrated with Calcite. The permeability of the tested sample showed an interesting behavior in which a rapid decrease during the beginning of injection then it showed as stable behavior until the end of percolation where the porosity of the sample was increased due to dissolution.

The interested behavior of permeability and porosity evolution obtained from the mixing experiments leaded us to study the evolution of these properties under different dissolution regimes. Injection of deionized water (DW) also causes permeability decrease in spite of dissolution reaction. At this point we suggested that relatively low dissolution rate can lead to permeability reduction because of the mechanical redistribution of the sample structure and detachment of microparticles from the inlet of the sample towards the outlet. That implies a clogging of pores, and consequently the permeability decreases.
Other experiments were done where more aggressive water was injected (DW enriched with CO_2) to increase the dissolution reactions consequently the measured Permeability of the tested sample increased.
In other words, the evolution of permeability can be considered as the result of a competition between the process of micro particle "production" (due to detachment) and the Calcite chemical dissolution process, in which the permeability variation of the tested sample can follow different scenarios:

- When the production of Calcite micro particles is higher than the chemical dissolution, permeability decreases.
- When both processes are in equilibrium, permeability does not change.
- When the dissolution process is higher than produced micro particles, permeability increases.

Evidences of particles detachment due to dissolution and pore clogging were captured from SEM and XRMT analysis also the increase of micro porous phase implies that there is a mechanical processes that took place into the tested sample causing a decrease in particle diameter due to dissolution.
This splitting processes causes permeability to decrease on the other hand permeability increases later if the dissolution reaction is enough high to dissolve the crumbled particles.

Finally, we present a simplified approach in which the permeability was modeled using Kozeny- Carman. The temporal evolution of permeability is related to the temporal evolution of particle diameter, porosity and tortuosity.

The experimental dissolution rate was used in the calculation of porosity updates and the particle diameter calculation at each time step. The only fitting parameter for better representation of the experimental data is the splitting rate. The model showed high agreement with the experimental data.

We can conclude that dissolution reactions can lead to permeability reduction if the dissolution rate is not enough high to dissolve detached microparticles and vice versa.

More complications are being done to enhance the model by incorporating different parameters that represent more closely the actual porous media, also to find a correlation between the splitting rate and the reaction rate.

Another model is under development in order to study evolution of permeability due to the micro particle deposition due detachment and attachment processes using the advective dispersion equation.

8. References

Adler P. M. (1992). Porous media: Geometry and transports: Butterworth/Heinemann, Stoneham, MA, 544 p.

Appelo C. A. J. and Postma D. (2005). Geochemistry, groundwater and pollution, 2nd Edition: A.A. Balkema Publishers, Leiden, The Netherlands, 649 p.

Auriault J. L. and Boutin C. (1992). Deformable porous media with double porosity. Quasi-statics, I: Coupling effects. *Transport Porous Media*, 7: 63-82.

Back W., Hanshaw B. B., Herman J.S., and Van Driel J. N. (1986). Differential dissolution of a Pleistocene reef in the groundwater mixing zone of coastal Yucatan, Mexico. *Geology*, 14: 137-140.

Back W., Hanshaw B. B., Pyle T. E., Plummer L.N., and Weidie A. E. (1979). Geochemical significance of groundwater discharge and carbonate solution to the formation of Caleta Xel Ha, Quintana Roo, Mexico. *Water Resources Research*, 15: 1521-1535.

Barlow P. M. (2003). Ground Water in Freshwater-Saltwater Environments of the Atlantic Coast. U.S. Geological Survey circular; 1262. http://pubs.usgs.gov/circ/2003/circ1262/

Bear J. (1972). Dynamics of Fluids in Porous Media. Elsevier.

Bear J., Cheng A. H. D., Sorek S., Ouazar D., and Herrera I. (1999). Seawater Intrusion in Coastal Aquifers: Concepts, Methods and Practices, Kluwer, Dordrecht, pp. 1-625.

Ben Clennell, M. (1997). Tortuosity: a guide through the maze. Developments in Petrophysics, Geological Society of London, Special Publication, 122:299-344.

Berryman J. G. and Wang W. F. (2000). Elastic wave propagation and attenuation in a double-porosity dual-permeability medium," International Journal of Rock Mechanics 37,63-78 .

Bourbie T. and Zinszner, B. (1985). Hydraulic end acoustic properties as a function of porosity in Fontainebleau sandstone. *Journal of Geophysical Research*, 90:11524-11532.

Carman P. C. (1937). Fluid flow through granular beds. Transactions, Institution of Chemical Engineers, London, 15: 150-166.

Cochepin B., Trotignon L., Bildstein O., Steefel C. I., Lagneau V., Van der lee J. (2008). Approaches to modelling coupled flow and reaction in a 2D cementation experiment. *Advances in Water Resources*, 31:1540-1551.

Coker D. A., Torquato S, and Dunsmuir J. H. (1996). Morphology and physical properties of Fontainebleau sandstone via a tomographic analysis, *Journal of Geophysical Research*, 101: 17497-17506.

Corbella M., Ayora C. and Cardellach E. (2003). Dissolution of deep carbonate rocks by fluid mixing: a discussion based on reactive transport modeling. *Journal of Geochemical Exploration*, 78(9): 211-214.

Corbella M., Ayora C. and Cardellach E. (2004). Hydrothermal mixing, carbonate dissolution and sulfide precipitation in Mississippi Valley-type deposits. *Mineralium Deposita*, 39(3): 344-357.

Custodio E. (2002). Coastal aquifers as important natural hydrogeological structures, in: Groundwater and Human Development, M. Bocanegra and M. Massone, eds., Barcelone, pp. 1905–1918.

Cvetkovic V. and Dagan G. (1994). Transport of kinetically sorbing solute by steady random velocity in heterogeneous porous formations. *Journal of Fluid Mechanics*, 265: 189-215.

De Marsily G. (1986). Quantitative hydrogeology. Groundwater hydrology for engineers. Academic Press, Inc., 440 p.

Delerue J. F., Perrier E., Yu Z. Y. and Velde B. (1999). New algorithms in 3D image analysis and their application to the measurement of a spatialized pore size distribution in soils. *Physics and Chemistry of the Earth,* Part A: Solid Earth and Geodesy, 24 (7): 639-644.

Dobson P. F., Kneafsey T. J., Sonnenthal E. L., Spycher N. F. and Apps J. A. (2003). Experimental and numerical simulation of dissolution and precipitation: implications for fracture sealing at Yucca Mountain. *Journal of Contaminant Hydrology* 62-63:459-476

El-Dessouky H. T. and Ettouney H. M. (2002). Fundamentals of Salt Water Desalination. Amsterdam, Elsevier Science B.V.: VII-X.

Finney J. (1970). Random packing and the structure of simple liquids (The geometry of random close packing). Proceedings of the Royal Society, November 10th, 1970, vol. 319 no. (1539):479-493

Garing C. (2011). Caractérisation géophysique et géochimique des interactions fluide-roche à l'interface eau douce-eau salée : cas des carbonates récifaux de Majorque. PhD thesis, Universite Montpellier II, France.

Gledhill D. K. and Morse J. W. (2006). Calcite dissolution kinetics in Na–Ca–Mg–Cl brines. *Geochimica et Cosmochimica Acta*, 70: 5802-5813.

Goldstein J. (2003). Scanning electron microscopy and x-ray microanalysis. Kluwer Adacemic/Plenum Pulbishers, 689 p.

González L. A. and Ruiz H. M. (1991). Diagenesis of Middle Tertiary carbonates in the Toa Baja Well, Puerto Rico. *Geophysical Research Letters*, 18(3):513-516.

Gouze P. and Luquot L. (2011). X-ray microtomography characterization of porosity, permeability and reactive surface changes during dissolution. *Journal of Contaminant Hydrology*, 120(21): 45-55.

Gouze P., C. Noiriel C. Bruderer D. Loggia and R. Leprovost (2003). X-ray tomography characterization of fracture surfaces during dissolution. *Geophysical Research Letters*, 30(5): 1267, doi:10.1029/2002GL016755.

Guadagnini A., Sanchez-Vila X., Saaltink M.W., Bussini, M. and Berkowitz B. (2009). Application of a mixing-ratios based formulation to model mixing-driven dissolution experiments. *Advances in Water Resources*, 5: 756-766

Guin J. A., Schechter, R. S. and Silberberg I. H. (1971). Chemically induced changes in porous media. *Industrial and Engineering Chemistry Fundamentals*, 10(1): 50-54.

Guyon E., Hulin J. P. and Petit L. (2001). Hydrodynamique Physique. EDP / Éditions CNRS. France, 674 p.

Hanshaw B. B. and Back W. (1979). Major geochemical processes in the evolution of carbonate aquifer systems. *Journal of Hydrology*, 43: 287-312.

Hanshaw B. B. and Back W. (1980). Chemical mass-wasting of the northern Yucatan Peninsula by groundwater dissolution. *Geology*, 8: 222-224.

Harvie C. E. and Weare J. H. (1980). The prediction of mineral solubilities in natural waters: The Na-K-Mg-Ca-Cl-SO4-H2O system from zero to high concentration at 25 °C. *Geochimica et Cosmochimica Acta*, 44: 981-997.

Harvie C. E., Moller N. and Weare J. H. (1984). The prediction of mineral solubilities in natural waters: The Na-K-Mg-Ca-H-Cl-SO4 -OH-HCO3 -CO3 -CO2 -H2O system to high ionic strengths at 25 °C. *Geochimica et Cosmochimica Acta*, 48:723-751

Heath R. C. (1984). Ground water regions of the United States. U.S. Geol. Survey Water Supply Paper 2242,

Higgins C. G. (1980). Nips, notches and the solution of coastal limestone: An overview of the problem with examples from Greece. *Estuarine and Coastal Marine Science*, 10: 15-30.

Hoefner M. L. and Fogler H. S. (1988). Pore evolution and channel forma t ion during flow and reaction in porous media. *AIChE Journal*, 34: 45-54.

Honeyborne D. B. (1982). The building limestones of France. Rapport technique, Building. Research Establishment Report, BRE, Garston, UK.

Ioannou I., Hoff W. D. and Hall C. (2004). On the role of organic adlayers in the anomalous water sorptivity of the l´epine limestone. *Journal of Colloid Interface Science*, 279: 228-234.

Katz G.E., Berkowitz B., Guadagnini A., and Saaltink M.W. (2011). Experimental and modeling investigation of multicomponent reactive transport in porous media. *Journal of Contaminant Hydrology*, 120-121: 27-44.

Kazatchenko E., Markov M. and Mousatov A. (2006). Simulation of acoustic velocities, electrical and thermal conductivities using unified pore-structure model of double-porosity carbonate rocks. *Journal of Applied Geophysics*, 59(1): 16-35.

Lasaga A.C. (1998). Kinetic Theory in the Earth Sciences. Princeton University Press, Princeton, NJ.

Lindquist W. B. and Venkatarangan A. (1999). Investigating 3D geometry of porous media from high resolution images. *Physics and Chemistry of the Earth*, Part A: Solid Earth and Geodesy. 24 (7): 593-599.

Lindquist W. B., Lee S. M., Coker D. A., Jones K. W. and Spanne P. (1996). Medial axis analysis of void structure in three-dimensional tomographic images of porous media. *Journal of Geophysical Research*, 101: 8297-8310.

Lindquist W. B., Venkatarangan A., Dunsmuir J. and Wong, T. F. (2000). Pore and throat size distributions measured from synchrotron X-ray tomographic images of Fontainebleau Sandstones. *Journal of Geophysical Research*, B: Solid Earth Planets 105 (9): 21509- 21527.

Lucia F. J. (1999). Carbonate Reservoir Characterization: An Integrated Approach, Springer.

Luquot L. and Gouze P. (2009). Experimental determination of porosity and permeability changes induced by injection of CO2 into carbonate rocks. *Chemical Geology*, 265: 148-159.

Magartiz M. and Luzier J. E. (1985). Water-rock interactions and seawater–freshwater mixing effects in the coastal dunes aquifer, Coos Bay, Oregon. *Geochimica et Cosmochimica Acta*, 49: 2515–2525.

Magnico P. (1996). Permeability evolution induced by the precipitation of an advected Solute: Effect of the Microscopic and the Macroscopic Scales Competition on the Clogging Mechanism. *Transport in Porous Media*, 24: 341-375.

Maliva R.G., Missimer T.M., Walker C.W., Owosina E.S., Dickson J.A.D., and Fallick A.E. (2001). Carbonate diagenesis in a high transmissivity coastal aquifer, Biscayne Aquifer, Southeastern Florida, USA. *Sedimentary Geology*, 143: 287-301.

Melim L.A., Westphal H., Swart P.K., Eberli G.P. and Munnecke, A. (2002). Questioning carbonate diagenetic paradigms: Evidence from the Neogene of the Bahamas. *Marine Geology*, 185: 27-53.

Morse J. W. (1983). The kinetics of calcium carbonate dissolution and precipitation .In: R.J. Reeder (Ed.), Carbonates: Mineralogy and Chemistry, Mineral Soc. Am. Rev. Mineral., II, pp. 227‑264

Morse J. W. and Arvidson R. S. (2002). The dissolution kinetics of major sedimentary carbonate minerals. *Earth-Science. Reviews*, 58: 51-84.

Morse J. W. and Berner R. C. (1979). Chemistry of calcium carbonate in the deep oceans. In Chemical Modelling- Speciation, Sorption, Solubility, and Kinetics in Aqueous Systems, vol. 93, Jenne E. (ed.), pp. 499-535. ACS Symposium Series.

Navarre-Sitchler A., Steefel C. I., Yang L., Tomutsa L. and Brantley S.A. (2009). Evolution of porosity and diffusivity associated with chemical weathering of a basalt clast. *Journal of Geophysical Research*, 114, F02016, doi: 10.1029/2008JF001060.

Ng K. C. and Jones B. (1995). Hydrogeochemistry of Grand Cayman British West Indies: implications for carbonate diagenetic studies. *Journal of Hydrology*, 164: 193-216.

Noiriel C., Bernard D., Gouze P. and Thibault X. (2005). Hydraulic properties and microgeometry evolution in the course of limestone dissolution by CO_2-enriched water. *Oil and Gas Science and Technology*, 60(1–2): 177-192.

Noiriel C., Gouze P., Bernard D. (2004). Investigation of porosity and permeability effects from microstructure changes during limestone dissolution. *Geophysical Research Letter*, 31, L24603, doi:10.1029/2004GL021572.

Noiriel C., Luquot L., Madé B., Raimbault L., Gouze P. and van der Lee J. (2009). Changes in reactive surface area during limestone dissolution: An experimental and modeling study. *Chemical Geology*, 265(1-2), 160-170.

Ortoleva E, Chadam J., Merino E. and Sen A. (1987b). Geochemical self-organization II: The reaction infiltration instability. *American Journal of science*, 287: 1008-1040.

Ortoleva E, Merino E., Moore C. and Chadam J. (1987a). Geochemical self-organization I: Reaction-transport feedbacks and modeling approach. American Journal of science, 287: 979-1007.

Pape H., Clauser C. and Iffland J. (1998). Permeability prediction for reservoir sandstones and basement rocks based on fractal pore space geometry, SEG Expanded Abstracts, SEG 1998 Meeting.

Parkhurst D. L. and Appelo C. A. J. (2006). PHREEQC, A hydrogeochemical transport model. In. http://wwwbrr.cr.usgs.gov/projects/GWCcoupled/phreeqc/

Parkhurst D. L., Thorstenson D. C. and Plummer, L. N. (1980). PHREEQE, A computer program for geochemical calculations:U.S. Geological Survey Water-Resources Investigations Report 80-96, 195 p. (Revised and reprinted August, 1990.)

Phillips O. M., (1991). Flow and reactions in Permeable Rocks, Cambridge University Press, Cambridge.

Pitzer K.S. (1979). Theory-Ion interaction approach: in R.M. Pytkowicz, ed., Activity Coefficients in Electrolyte Solutions, v. 1, CRC Press, Inc., Boca Raton, Florida, p. 157-208.

Plummer L. N. (1975). Mixing of seawater with calcium carbonate groundwater. In: E.H.T. Whitten, Editor, Quantitative Studies in the Geological Sciences, Geological Society of America Memoir 142: 219-236.

Plummer L. N., Wigley T. M. L. and Parkhurst D. L. (1978). The kinetics of calcite dissolution in CO_2-water systems at 5 to 60 °C and 0.0 to 1.0 atm CO_2. *Amirican journal of science*, 278: 179.

Plummer L.N., Parkhurst D.L., Fleming G.W., and Dunkle S.A. (1988). A computer program incorporating Pitzer's equations for calculation of geochemical reactions in brines: U.S. Geological SurveyWater-Resources Investigations Report 88-4153, 310 p.

Plummer L.N., Vacher H.L., Mackenzie F.T., Bricker O.P., and Land L.S. (1976). Hydrogeochemistry of Bermuda: A case history of ground-water diagenesis of biocalcarenites. Geological Society of America Bulletin, 87: 1301-1316.

Pokrovsky O. S. and Schott S. (2000). Forsterite surface composition in aqueous solutions: A combined potentiometric, electrokinetic, and spectroscopic approach. *Geochimica et Cosmochimica Acta*, 64: 3299-3312.

Pokrovsky O. S., Golubev S. V. and Schott J. (2005). Dissolution kinetics of calcite, dolomite and magnesite at 25 °C and 0 to 50 atm pCO_2. *Chemical Geology*, 217(3-4): 239-255.

Pokrovsky O. S., Golubev S., Schott J., Castillo A., (2009). Calcite, dolomite and magnesite dissolution kinetics in aqueous solutions at acid to circum neutral pH, 25 to 150 °C and 1 to 55 atm pCO2: new constraints on CO2 sequestration in sedimentary basins. *Chemical Geology*, 265 (1-2): 20-32

Price R. M. and Herman J. S. (1991). Geochemical investigation of salt-water intrusion into a coastal carbonate aquifer: Mallorca, Spain. *Geological Society of America Bulletin*, 103: 1270-1279.

Rard J. A. and Wijesinghe A. M. (2003). Conversion of parameters between different variants of Pitzers ion-interaction model, both with and without ionic strength dependent higher-order terms. *Journal of Chemical Thermodynamics*, 35(3):439-473.

Reilly T. E. and Goodman A. S. (1985). Quantitative Analysis of Saltwater-Freshwater Relationships in Groundwater Systems - A Historical Perspective. *Journal of Hydrology*, 80: 125-160.

Rezaei M., Sanz E., Raeisi E., Ayora C., Vázquez-Suñe E., and Carrera J. (2005). Reactive transport modeling of calcite dissolution in the fresh-salt water mixing zone. *Journal of Hydrology*, 311: 282-298.

Romanov D. and Dreybrodt W. (2006). Evolution of porosity in the saltwater-freshwater mixing zone of coastal carbonate aquifers: An alternative modeling approach *Journal of Hydrology*, 329: 661-673

Rosso J. J. and Rimstidt J. D. (2000). A high resolution study of fosterite dissolution rates. *Geochimica et Cosmochimica Acta*, 64: 797-812.

Sanford W. E. and Konikow L. F. (1989a). Simulation of calcite dissolution and porosity changes in saltwater mixing zones in coastal aquifers. *Water Resources Research*, 25: 655-667.

Sanford W. E. and Konikow L. F. (1989b). Porosity development in coastal carbonate aquifers. *Geology*, 17: 249-252.

Sanz E., Ayora C. and Carrera J. (2011). Calcite dissolution by mixing waters: geochemical modeling and flow-through experiments. *Geologica Acta*, 9: 67-77.

Savitzky A. and Golay M. J. E. (1964). Smoothing and Differentiation of Data by Simplified Least Squares Procedures. *Analytical Chemistry*, 36(8):1627-1639.

Schechter R. S. and Gidley J. L. (1969). The change in pore size distribution from surface reactions in porous media. *AIChE Journal*, 15: 339-350.

Schott J., Pokrovsky O. S. and Oelkers E. H. (2009). The Link between mineral dissolution/precipitation kinetics and Solution chemistry. *Reviews in Mineralogy and Geochemistry*, 70(1): 207-258.

Singurindy O. and Berkowitz B. (2003). Evolution of hydraulic conductivity by precipitation and dissolution in carbonate rock. *Water Resources Research*, 39(1): 14.

Singurindy O., Berkowitz B., and Lowell R. P. (2004). Carbonate dissolution and precipitation in coastal environments: Laboratory analysis and theoretical consideration. *Water Resources Research*, 40: 1-12.

Smart P. L., Dawans J. M. and Whitaker F. (1988). Carbonate dissolution in a modern mixing zone. *Nature*, 335: 811-813.

Steefel C. I. and Lasaga A. C. (1994). A coupled model for transport of multiple chemical species and kinetic precipitation/dissolution reactions with application to the reactive flow in single phase hydrothermal systems. *American Journal of science*, 294: 529-592.

Steefel C. I. and Lasaga A. C. (1990). The evolution of dissolution patterns: Permeability change due to coupled flow and reaction. In Chemical Modeling of Aqueous Systems II. Vol. 416. Melchior D. and Bassett R. L. (ed) American Chemical Society, Washington, p 212-225.

Steefel C. I. and Lichtner P. C. (1994). Diffusion and reaction in rock matrix bordering a hyperalkaline fluid-filled fracture. *Geochim Cosmochim Acta*, 58: 3595-3612.

Steefel C. I. and Lichtner P. C. (1998a). Multicomponent reactive transport in discrete fractures: II. Infiltration of hyperalkaline groundwater at Maqarin, Jordan, a natural analogue site. *Journal of Hydrology*, 209: 200-224

Steefel C. I. and Lichtner P. C. (1998b). Multicomponent reactive transport in discrete fractures: I. Controls on reaction front geometry. *Journal of Hydrology*, 209:186-199.

Steefel C. I. Maher K. (2009). Fluid-rock interaction: A reactive transport approach. *Reviews in Mineralogy and Geochemistry*, 70: 485-532.

Stossell R. K., Ward W. C., Ford B. H. and Schuffert J. D. (1989). Water chemistry and CaCO3 dissolution in the saline part of an open flow mixing zone, coastal Yucatan Peninsula, Mexico. *Geological Society of America Bulletin*, 101: 159-169.

Sun R. J., and Johnston R. H. (1994). Regional Aquifer-Systems Analysis Program of the U.S. Geological Survey, 1978-92: U.S. Geological Survey Circular 1099, 126 p.

Taud H., Martinez-Angeles R., Parrot J. F. and Hernandez-Escobedo L. (2005). Porosity estimation method by X-ray computed tomography. *Journal of Petroleum Science and Engineering*, 47: 209-217

Todd D. K. and Mays L. W. (2005). Groundwater Hydrology. 3rd Edition (pp. 589-606). USA: John Wiley and Sons, Inc

Walsh M. E., Bryant S. L., Schechter R. S. and Lake L. W. (1984). Precipitation and dissolution of solids attending flow through porous media. *AIChE Journal*, 30: 317-328.

Whitaker F. F. and Smart P. L. (1997). Groundwater circulation and geochemistry of a karstified bankmarginal fracture system, South Andros Island, Bahamas. *Journal of Hydrology*, 197: 293-315.

Wicks C. M. and Herman J. S. (1996). Regional Hydrogeochemistry of a Modern Coastal Mixing Zone. *Water Resources Research*, 32(2): 401-407.

Wicks C. M., Herman J. S., Randazzo A. F., and Jee J. L. (1995). Water-rock interactions in a modern coastal mixing zone. *Geological Society of America Bulletin*, 107: 1023-1032.

Wigley T. M. L. and Plummer L. N. (1976). Mixing of carbonate waters. *Geochimica et Cosmochimica Acta*, 40 (9): 989–995.

Annexes

A. Input file for PHREEQC for both 15% and 45% mixing ratios of salty end member solution.

```
SOLUTION 1 # Fresh end member solution
    temp      25
    pH        7
    pe        4
    redox     pe
    units     mol/kgw
    density   1
    -water    1 # kg

EQUILIBRIUM_PHASES 1
    CO2(g)    -3.5 10
    Calcite   0 10
SAVE SOLUTION 1
End
------------------------------------------------------------------------
SOLUTION 2 # salty end member solution
    temp      25
    pH        7
    pe        4
    redox     pe
    units     mol/kgw
    density   1
    Na        1
    Cl        1
    -water    1 # kg
EQUILIBRIUM_PHASES 2
    CO2(g)    -2 10
    Calcite   0 10
SAVE SOLUTION 2
End
------------------------------------------------------------------------
#Mixing

Mix 1 #Mixing ratio of 15%
1 0.85
2 0.15
END
------------------------------------------------------------------------
Mix 2 #Mixing  ratio of 45%
1 0.55
2 0.45
END
```

B. Output file form PHREEQC

```
Input file: C:\Phreeqc\Diapor.pqi
Output file:C:\Phreeqc\Diapor.pqo
Database file: C:\Phreeqc Interactive 2.17.4799\database\pitzer.dat

------------------
Reading data base.
------------------

      SOLUTION_MASTER_SPECIES
      SOLUTION_SPECIES
      PHASES
      PITZER
      EXCHANGE_MASTER_SPECIES
      EXCHANGE_SPECIES
      SURFACE_MASTER_SPECIES
      SURFACE_SPECIES
      END
-----------------------------------
Reading input data for simulation 1.
-----------------------------------

DATABASE C:\Program Files\USGS\Phreeqc Interactive
2.17.4799\database\pitzer.dat

SOLUTION 1 # Fresh water
          temp      25
          pH        7
          pe        4
          redox     pe
          units     mol/kgw
          density   1
          water    1 # kg
      EQUILIBRIUM_PHASES 1
          CO2(g)    -3.5 10
          Calcite      0 10
      SAVE SOLUTION 1
      end
-------------------------------------------
Beginning of initial solution calculations.
-------------------------------------------

Initial solution 1.
-----------------------------Solution composition------------------------------

      Elements           Molality       Moles

      Pure water
----------------------------Description of solution----------------------------

                                     pH  =   7.000
                                     pe  =   4.000
       Specific Conductance (uS/cm, 25 oC) = 0
                           Density (g/cm3)  =   0.99705
                       Activity of water  =   1.000
```

Fresh water

```
                          Ionic strength  =  1.003e-007
                       Mass of water (kg)  =  1.000e+000
                 Total alkalinity (eq/kg)  =  4.618e-010
                    Total carbon (mol/kg)  =  0.000e+000
                       Total CO2 (mol/kg)  =  0.000e+000
                     Temperature (deg C)  =  25.000
                  Electrical balance (eq)  = -4.618e-010
 Percent error, 100*(Cat-|An|)/(Cat+|An|)  =  -0.23
                              Iterations  =   2
                         Gamma iterations  =   2
                      Osmotic coefficient  =   0.99988
                         Density of water  =   0.99706
                                  Total H  = 1.110124e+002
                                  Total O  = 5.550622e+001

----------------------------Distribution of species----------------------------
                                                                  MacInnes   MacInnes
                                       MacInnes    Log           Log          Log
   Species                Molality     Activity  Molality     Activity       Gamma

   OH-                  1.005e-007  1.005e-007    -6.998      -6.998      -0.000
   H+                   1.000e-007  1.000e-007    -7.000      -7.000      -0.000
   H2O                  5.551e+001  1.000e+000     1.744      -0.000       0.000

------------------------------Saturation indices-------------------------------
      Phase               SI log IAP  log KT

      H2O(g)           -1.51   -0.00    1.51  H2O

-----------------------------------------
Beginning of batch-reaction calculations.
-----------------------------------------

Reaction step 1.

Using solution 1.
Using pure phase assemblage 1.

--------------------------------Phase assemblage--------------------------------

                                                        Moles in assemblage
Phase                  SI log IAP  log KT      Initial       Final       Delta

Calcite              0.00   -8.41   -8.41   1.000e+001  9.999e+000 -5.295e-004
CO2(g)              -3.50   -4.97   -1.47   1.000e+001  9.999e+000 -5.218e-004

-----------------------------Solution composition-----------------------------

      Elements           Molality       Moles
      C                1.051e-003  1.051e-003
      Ca               5.295e-004  5.295e-004
```

----------Description of solution----------

```
                            pH  =   8.297      Charge balance
                            pe  =   4.000      Adjusted to redox equilibrium

       Specific Conductance (uS/cm, 25 oC) = 104
                           Density (g/cm3)  =   0.99712
                        Activity of water   =   1.000
                           Ionic strength   =  1.582e-003
                        Mass of water (kg)  =  1.000e+000
                 Total alkalinity (eq/kg)   =  1.059e-003
                        Total CO2 (mol/kg)  =  1.051e-003
                      Temperature (deg C)   =  25.000
                    Electrical balance (eq) = -4.618e-010
 Percent error, 100*(Cat-|An|)/(Cat+|An|)   =  -0.00
                                Iterations  =  16
                           Gamma iterations =   4
                        Osmotic coefficient =   0.97226
                           Density of water =   0.99706
                                    Total H = 1.110124e+002
                                    Total O = 5.550885e+001
```

----------Distribution of species----------

Species	Molality	MacInnes Activity	Log Molality	MacInnes Log Activity	MacInnes Log Gamma
OH-	2.096e-006	1.991e-006	-5.679	-5.701	-0.022
H+	5.284e-009	5.046e-009	-8.277	-8.297	-0.020
H2O	5.551e+001	1.000e+000	1.744	-0.000	0.000
C(4)	1.051e-003				
HCO3-	1.024e-003	9.810e-004	-2.990	-3.008	-0.019
CO2	1.076e-005	1.077e-005	-4.968	-4.968	0.000
CO3-2	1.074e-005	8.902e-006	-4.969	-5.051	-0.082
CaCO3	5.560e-006	5.560e-006	-5.255	-5.255	0.000
Ca	5.295e-004				
Ca+2	5.239e-004	4.409e-004	-3.281	-3.356	-0.075
CaCO3	5.560e-006	5.560e-006	-5.255	-5.255	0.000

----------Saturation indices----------

Phase	SI	log IAP	log KT	
Aragonite	-0.19	-8.41	-8.22	CaCO3
Calcite	0.00	-8.41	-8.41	CaCO3
CO2(g)	-3.50	-4.97	-1.47	CO2
H2O(g)	-1.51	-0.00	1.51	H2O
Portlandite	-9.57	-14.76	-5.19	Ca(OH)2

```
------------------
End of simulation.
------------------
```

```
------------------------------------
Reading input data for simulation 2.
------------------------------------

      SOLUTION 2 # saltwater
          temp      25
          pH        7
          pe        4
          redox     pe
          units     mol/kgw
          density   1
          Na        1
          Cl        1
          water    1 # kg
      EQUILIBRIUM_PHASES 2
          CO2(g)    -2 10
          Calcite   0 10
      SAVE SOLUTION 2
      end
----------------------------------------
Beginning of initial solution calculations.
----------------------------------------

Initial solution 2.

-----------------------------Solution composition------------------------------

      Elements           Molality       Moles

      Cl                1.000e+000  1.000e+000
      Na                1.000e+000  1.000e+000

----------------------------Description of solution----------------------------

                                       pH  =   7.000
                                       pe  =   4.000
       Specific Conductance (uS/cm, 25 oC) = 81503
                           Density (g/cm3)  =   1.03620
                        Activity of water   =   0.967
                           Ionic strength   =  1.000e+000
                        Mass of water (kg)  =  1.000e+000
                 Total alkalinity (eq/kg)   =  7.092e-008
                    Total carbon (mol/kg)   =  0.000e+000
                       Total CO2 (mol/kg)   =  0.000e+000
                     Temperature (deg C)    =  25.000
                   Electrical balance (eq)  = -7.092e-008
 Percent error, 100*(Cat-|An|)/(Cat+|An|)   =  -0.00
                                Iterations  =   6
                           Gamma iterations =   4
                        Osmotic coefficient =   0.93564
                           Density of water =   0.99706
                                    Total H = 1.110124e+002
                                    Total O = 5.550622e+001
```

Salty solution

```
----------------------------Distribution of species--------------------------

                                                                  MacInnes   MacInnes
                                        MacInnes    Log           Log        Log
   Species                 Molality      Activity  Molality      Activity     Gamma

   OH-                  1.765e-007  9.713e-008    -6.753    -7.013    -0.259
   H+                   1.056e-007  1.000e-007    -6.977    -7.000    -0.023
   H2O                  5.551e+001  9.669e-001     1.744    -0.015     0.000
Cl              1.000e+000
   Cl-                  1.000e+000  6.028e-001    -0.000    -0.220    -0.220
Na              1.000e+000
   Na+                  1.000e+000  7.115e-001    -0.000    -0.148    -0.148

------------------------------Saturation indices-----------------------------

      Phase               SI log IAP  log KT

      H2O(g)           -1.52   -0.01    1.51  H2O
      Halite           -1.94   -0.37    1.57  NaCl

----------------------------------------
Beginning of batch-reaction calculations.
----------------------------------------

Reaction step 1.

Using solution 2.
Using pure phase assemblage 2.

------------------------------Phase assemblage-------------------------------

                                                        Moles in assemblage
Phase                   SI log IAP  log KT      Initial       Final       Delta

Calcite              0.00   -8.41   -8.41   1.000e+001  9.996e+000 -3.697e-003
CO2(g)              -2.00   -3.47   -1.47   1.000e+001  9.996e+000 -3.921e-003

-----------------------------Solution composition----------------------------

      Elements           Molality       Moles

      C                7.618e-003  7.618e-003
      Ca               3.697e-003  3.697e-003
      Cl               1.000e+000  1.000e+000
      Na               1.000e+000  1.000e+000

----------------------------Description of solution---------------------------

                                     pH  =   7.382      Charge balance
                                     pe  =   4.000      Adjusted to redox
equilibrium
       Specific Conductance (uS/cm, 25 oC) = 81652
                           Density (g/cm3)  =   1.03663
                        Activity of water   =   0.967
                           Ionic strength   =  1.011e+000
                       Mass of water (kg)   =  9.999e-001
```

```
                 Total alkalinity (eq/kg)  =  7.395e-003
                       Total CO2 (mol/kg)  =  7.618e-003
                     Temperature (deg C)   =  25.000
                  Electrical balance (eq)  = -7.092e-008
 Percent error, 100*(Cat-|An|)/(Cat+|An|)  =  -0.00
                              Iterations   =  20
                         Gamma iterations  =   5
                     Osmotic coefficient   =   0.93551
                        Density of water   =   0.99706
                                 Total H   = 1.110124e+002
                                 Total O   = 5.552515e+001

----------------------------Distribution of species----------------------------

                                                                  MacInnes    MacInnes
                                          MacInnes     Log         Log          Log
   Species                  Molality      Activity   Molality    Activity      Gamma

   OH-                   4.296e-007   2.342e-007     -6.367      -6.630     -0.264
   H+                    4.380e-008   4.147e-008     -7.359      -7.382     -0.024
   H2O                   5.551e+001   9.667e-001      1.744      -0.015      0.000
C(4)            7.618e-003
   HCO3-                 7.280e-003   3.649e-003     -2.138      -2.438     -0.300
   CO2                   2.812e-004   3.405e-004     -3.551      -3.468      0.083
   CO3-2                 5.137e-005   4.029e-006     -4.289      -5.395     -1.106
   CaCO3                 5.560e-006   5.560e-006     -5.255      -5.255      0.000
Ca              3.697e-003
   Ca+2                  3.692e-003   9.741e-004     -2.433      -3.011     -0.579
   CaCO3                 5.560e-006   5.560e-006     -5.255      -5.255      0.000
Cl              1.000e+000
   Cl-                   1.000e+000   6.022e-001      0.000      -0.220     -0.220
Na              1.000e+000
   Na+                   1.000e+000   7.116e-001      0.000      -0.148     -0.148

------------------------------Saturation indices-------------------------------

      Phase               SI log IAP  log KT

      Aragonite        -0.19   -8.41   -8.22  CaCO3
      Calcite           0.00   -8.41   -8.41  CaCO3
      CO2(g)           -2.00   -3.47   -1.47  CO2
      Gaylussite       -4.75  -14.17   -9.42  CaNa2(CO3)2:5H2O
      H2O(g)           -1.52   -0.01    1.51  H2O
      Halite           -1.94   -0.37    1.57  NaCl
      Nahcolite        -2.18  -12.92  -10.74  NaHCO3
      Natron           -5.01   -5.84   -0.82  Na2CO3:10H2O
      Pirssonite       -4.89  -14.13   -9.23  Na2Ca(CO3)2:2H2O
      Portlandite     -11.08  -16.27   -5.19  Ca(OH)2
      Trona            -7.26  -18.64  -11.38  Na3H(CO3)2:2H2O

------------------
End of simulation.
------------------
```

```
------------------------------------
Reading input data for simulation 3.
------------------------------------

      SELECTED_OUTPUT
          file                 diapor.txt
          selected_out         true
          reset                false
          ph                   true
          alkalinity           true
          ionic_strength       true
          totals               C  Ca  Cl  Na
          saturation_indices   Calcite  CO2(g)
      Mix 1 #Mixing ratio of 15%
      1 0.85
      2 0.15
      END
----------------------------------------
Beginning of batch-reaction calculations.
----------------------------------------

Reaction step 1.

Using mix 1.


Mixture 1.

8.500e-001 Solution 1   Solution after simulation 1.
1.500e-001 Solution 2   Solution after simulation 2.

-----------------------------Solution composition------------------------------

      Elements           Molality       Moles

      C                2.036e-003  2.036e-003
      Ca               1.005e-003  1.005e-003
      Cl               1.500e-001  1.500e-001
      Na               1.500e-001  1.500e-001

----------------------------Description of solution----------------------------

                                       pH  =   7.811      Charge balance
                                       pe  =   4.000      Adjusted to redox
equilibrium
       Specific Conductance (uS/cm, 25 oC) = 16027
                           Density (g/cm3)  =   1.00331
                        Activity of water   =   0.995
                           Ionic strength   =  1.530e-001
                        Mass of water (kg)  =  1.000e+000
                 Total alkalinity (eq/kg)   =  2.009e-003
                        Total CO2 (mol/kg)  =  2.036e-003
                     Temperature (deg C)    =  25.000
                   Electrical balance (eq)  = -1.101e-008
 Percent error, 100*(Cat-|An|)/(Cat+|An|)   =  -0.00
                                Iterations  =  10
                           Gamma iterations =   3
```

Mixing ratio 15%

```
                    Osmotic coefficient  =   0.92519
                       Density of water  =   0.99706
                                Total H  = 1.110124e+002
                                Total O  = 5.551129e+001
```

----------Distribution of species----------

Species	Molality	MacInnes Activity	Log Molality	MacInnes Log Activity	MacInnes Log Gamma
OH-	8.965e-007	6.475e-007	-6.047	-6.189	-0.141
H+	1.935e-008	1.544e-008	-7.713	-7.811	-0.098
H2O	5.551e+001	9.950e-001	1.744	-0.002	0.000
C(4)	2.036e-003				
HCO3-	1.973e-003	1.388e-003	-2.705	-2.858	-0.153
CO2	4.551e-005	4.684e-005	-4.342	-4.329	0.013
CO3-2	1.559e-005	4.118e-006	-4.807	-5.385	-0.578
CaCO3	1.956e-006	1.956e-006	-5.709	-5.709	0.000
Ca	1.005e-003				
Ca+2	1.003e-003	3.353e-004	-2.999	-3.475	-0.476
CaCO3	1.956e-006	1.956e-006	-5.709	-5.709	0.000
Cl	1.500e-001				
Cl-	1.500e-001	1.104e-001	-0.824	-0.957	-0.133
Na	1.500e-001				
Na+	1.500e-001	1.143e-001	-0.824	-0.942	-0.118

----------Saturation indices----------

Phase	SI	log IAP	log KT	
Aragonite	-0.64	-8.86	-8.22	CaCO3
Calcite	-0.45	-8.86	-8.41	CaCO3
CO2(g)	-2.86	-4.33	-1.47	CO2
Gaylussite	-6.72	-16.14	-9.42	CaNa2(CO3)2:5H2O
H2O(g)	-1.51	-0.00	1.51	H2O
Halite	-3.47	-1.90	1.57	NaCl
Nahcolite	-3.40	-14.14	-10.74	NaHCO3
Natron	-6.47	-7.29	-0.82	Na2CO3:10H2O
Pirssonite	-6.90	-16.13	-9.23	Na2Ca(CO3)2:2H2O
Portlandite	-10.66	-15.85	-5.19	Ca(OH)2
Trona	-10.03	-21.41	-11.38	Na3H(CO3)2:2H2O

```
------------------
End of simulation.
------------------------------------
```

```
Reading input data for simulation 4.
-----------------------------------

      Mix 2 #Mixing ratio of 45%
      1 0.55
      2 0.45
      END
----------------------------------------
Beginning of batch-reaction calculations.
----------------------------------------

Reaction step 1.

Using mix 2.


Mixture 2.

5.500e-001 Solution 1   Solution after simulation 1.
4.500e-001 Solution 2   Solution after simulation 2.

------------------------------Solution composition------------------------------
      Elements           Molality       Moles

      C                4.006e-003  4.006e-003
      Ca               1.955e-003  1.955e-003
      Cl               4.500e-001  4.500e-001
      Na               4.500e-001  4.500e-001

----------------------------Description of solution----------------------------

                                    pH  =   7.561      Charge balance
                                    pe  =   4.000      Adjusted to redox
equilibrium
       Specific Conductance (uS/cm, 25 oC) = 43931
                           Density (g/cm3)  =   1.01537
                        Activity of water   =   0.985
                           Ionic strength   =  4.559e-001
                        Mass of water (kg)  =  1.000e+000
                 Total alkalinity (eq/kg)   =  3.910e-003
                        Total CO2 (mol/kg)  =  4.006e-003
                     Temperature (deg C)    =  25.000
                  Electrical balance (eq)   = -3.217e-008
 Percent error, 100*(Cat-|An|)/(Cat+|An|)   =  -0.00
                                Iterations  =  12
                           Gamma iterations =   3
                       Osmotic coefficient  =   0.91978
                          Density of water  =   0.99706
                                   Total H  = 1.110124e+002
                                   Total O  = 5.551618e+001
```

Mixing ratio 45%

----------Distribution of species----------

Species	Molality	MacInnes Activity	Log Molality	MacInnes Log Activity	MacInnes Log Gamma
OH-	5.776e-007	3.605e-007	-6.238	-6.443	-0.205
H+	3.367e-008	2.745e-008	-7.473	-7.561	-0.089
H2O	5.551e+001	9.851e-001	1.744	-0.007	0.000
C(4)	4.006e-003				
HCO3-	3.851e-003	2.271e-003	-2.414	-2.644	-0.229
CO2	1.262e-004	1.376e-004	-3.899	-3.861	0.037
CO3-2	2.641e-005	3.787e-006	-4.578	-5.422	-0.843
CaCO3	2.761e-006	2.761e-006	-5.559	-5.559	0.000
Ca	1.955e-003				
Ca+2	1.952e-003	5.146e-004	-2.709	-3.288	-0.579
CaCO3	2.761e-006	2.761e-006	-5.559	-5.559	0.000
Cl	4.500e-001				
Cl-	4.500e-001	2.946e-001	-0.347	-0.531	-0.184
Na	4.500e-001				
Na+	4.500e-001	3.212e-001	-0.347	-0.493	-0.146

----------Saturation indices----------

Phase	SI	log IAP	log KT	
Aragonite	-0.49	-8.71	-8.22	CaCO3
Calcite	-0.30	-8.71	-8.41	CaCO3
CO2(g)	-2.39	-3.86	-1.47	CO2
Gaylussite	-5.73	-15.15	-9.42	CaNa2(CO3)2:5H2O
H2O(g)	-1.52	-0.01	1.51	H2O
Halite	-2.59	-1.02	1.57	NaCl
Nahcolite	-2.73	-13.48	-10.74	NaHCO3
Natron	-5.65	-6.47	-0.82	Na2CO3:10H2O
Pirssonite	-5.90	-15.13	-9.23	Na2Ca(CO3)2:2H2O
Portlandite	-10.98	-16.17	-5.19	Ca(OH)2
Trona	-8.51	-19.90	-11.38	Na3H(CO3)2:2H2O

End of simulation.

Reading input data for simulation 5.

End of run.
